Spring 1992

Ring Dynamics in the Western Gulf of Mexico

Adolphe W. Indest
Old Dominion University

Ring Dynamics
in
the Western Gulf of Mexico

by

A. W. Indest January 13, 1992
B. S. December 1979, Louisiana State University
M. S. August 1982, University of New Orleans

A Dissertation submitted to the Faculty of
Old Dominion University in Partial Fulfillment of the
Requirement for the Degree of

Doctor of Philosophy

Oceanography
Old Dominion University
May, 1992

Approved by:

A. D. Kirwan, Jr. (Director)

Acknowledgments

I would like to thank several people who have contributed in some way or another to my graduate career. First, I would like to extend my sincerest gratitude to Dr. Geiseler Gust for giving me the opportunity to change careers and study physical oceanography. Thanks to Dr. Gabe Csanady for expanding my world-view and to realize that I should always ask "What are the physics?". A tip of the jar to Dr. Chet Grosch for his insightful and illuminating methods of incorporating teaching with story-telling. My kind thanks to Dr. Dana Thompson for his generous support and help in making his numerical model codes available.

In the past several years there have been many people who have helped me through some bad times as well as good. Watson and Margarita Gregg, Wade Jeffery, Dave and Suzannah Costello, Jeff and Louise Hanson and all the folks in St. Petersburg who supported me during a low point in my life. Thanks go to Alan Wallcraft who put up with an incessant barrage of mail messages containing questions about the numerical model and his NCAR graphics plotting routines.

Thanks to the Department of Oceanography at Old Dominion University for their generosity and to the kind folks responsible for the Slover Fund . I am pleased to acknowledge the Office of Naval Research as the source of funding for my research.

A special thanks goes to my major professor, Dr. Denny Kirwan, who, besides introducing me to a cornucopia of magic bullets, has put up with me all these years.

Finally, my kind and heartfelt thanks to my wife who was supportive throughout my graduate tenure.

Table of Contents

List of Figures

List of Figures (continued)

List of Figures (continued)

List of Figures (continued)

Abstract

Ring Dynamics
in
the Western Gulf of Mexico

A. W. Indest
Old Dominion University
Director: A. D. Kirwan, Jr.

The interaction of a recently-formed Loop Current ring and a fossil ring is studied using observations and a two-layered eddy-resolving general circulation model of the Gulf of Mexico. This interaction is investigated by following the evolution of volume, energy, potential vorticity, angular momentum and enstrophy within a model ring as it moves westward and encounters a fossil ring along the continental slope of the Gulf of Mexico. By comparing the model results with drifter and hydrographic data several new insights into ring/ring and ring/slope interactions are seen. A Loop Current ring may merge with a fossil ring along the slope. The signature of this merger is evident in many drifter tracks suggesting that this occurs in the Gulf quite frequently. This merger explains several observations. There is an offshore transport induced by the merging of the rings that is comparable to the transport out of the Florida Straits. The volume of the Loop Current ring decreases sharply during the merger indicating an exchange of mass is occurring. A cyclone is generated when the ring interacts with a fossil ring and there is a transfer of energy from the surface layer to the lower layer.

Analysis also shows that during the merger, as expected, a decrease in energy, potential vorticity and angular momentum and an increase in enstrophy occur. Other cyclones are seen first in the lower layer, prior to the ring's arrival in the slope area, and then appear in the upper layer as the ring interacts with another ring and/or the slope.

1. Introduction

This paper focuses on the interaction of Loop Current rings with other rings along the western continental slope of the Gulf of Mexico using both observations and a two-layered eddy-resolving general circulation model. The underlying dynamics of these interactions are investigated by following the evolution of several integral quantities—volume (mass), energy, angular momentum, potential vorticity and enstrophy—within a model ring as it moves westward and encounters another anticyclonic ring along the continental slope of the Gulf of Mexico. In following these dynamical balances in two rings and by comparing the model results with drifter and hydrographic data several new insights into the dynamics of ring/ring and ring/slope interactions are seen.

In the mid-seventies, it was thought that a semi-permanent anticyclonic circulation existed in the Gulf. Later, as more data was collected, the understanding was that an anticyclone was spawned from the Loop Current, moved westward through the deeper part of the Gulf until it impinged upon the western slope where it then headed north. From the results presented here a new picture emerges. When a ring impinges upon the slope, it readjusts and may merge with a fossil ring. The signature of this merger is seen both in the observed drifter tracks and

the model results. During the merger, an exchange of mass may occur and there is evidence of a considerable transport offshore. In addition, the model results suggest a transfer of energy from the surface layer to the lower layer and a re-energizing of the fossil ring. Concomitantly, there is a cyclonic flow in the lower layer which intensifies and becomes expressed in the upper layer. After detaching from the fossil ring, a ring, paired with a cyclone, may move to the north.

This paper is organized in the following manner. A literature review is presented in the next section which is followed by a discussion of the analysis of the drifter data. A description of the integral quantities and how they are calculated is presented in the fourth section and a description of the numerical model and results from a ninety day simulation are presented in section 5. Comparisons between observations and model results are made in section 6. Finally, the conclusions are presented in section 7.

2. Literature Survey

The circulation of the Gulf of Mexico has been the subject of many studies. In a 1775 chart of the Gulf of Mexico, Debrahm depicted an anticyclonic circulation in the Gulf (DeVorsey, 1980). Prior to 1973, it was thought that there was a poorly-defined semi-permanent anticyclonic signature in the central Gulf (Sweitzer, 1898; Austin, 1955; Nowlin and McClellan, 1967; Nowlin *et al.*, 1968; Nowlin, 1972; Nowlin and Hubertz, 1972; Wert and Reid, 1972). Sturges and Blaha (1976) and Blaha and Sturges (1978) proposed the anticyclonic circulation was the result of the wind stress curl and planetary vorticity or a small-scale western boundary current. This was disputed by Elliot (1979, 1982) who used hydrographic and geomagnetic electro-kinetograph (GEK) data along with surface winds to show that these anticyclones were quite energetic and that they were probably spawned from the Loop Current, as originally proposed by Ichiye (1962). Kirwan *et al.*, (1984b) settled the matter by tracking a ring shed by the Loop Current across the Gulf to the continental shelf of Mexico.

It is now known that these rings are generated from an unstable meander of the Loop Current (Hurlburt and Thompson 1980, 1982; Lewis *et. al*, 1989). Once a ring pinched off from the Loop Current, it usually migrated west-southwest and

impinged upon the continental slope in the western Gulf of Mexico (Kirwan *et al.*, 1984a, 1984b, 1988; and Vukovich and Crissman, 1986). As shown by Kirwan, *et al.* (1984b) and Vukovich and Crissman (1986), these anticyclones remained stable as they moved across the Gulf following a path determined by topographic steering and interactions with other rings (Lewis *et al.*, 1989).

After encountering the slope, rings slowly migrated towards the north (Indest *et. al*, 1989) persisting for 3–5 months along the western boundary (Lewis and Kirwan, 1985). Nakamoto (1986, 1989) applied solitary wave theory to these rings to explain this northward migration along the slope and found that rings interacting with a slope behave as form-preserving flow structures. However not all rings migrated to the north. In part of a five year physical oceanographic field study of the Gulf of Mexico, SAIC (1988) showed a Loop Current ring remained stationary over the western slope before it migrated to the south.

Vukovich and Waddell (1991) described a Loop Current ring encountering the western slope in the Gulf of Mexico and found no indication of a large-scale exchange of water between the ring and the slope. From temperature measurements they showed an increase in area of the anticyclonic circulation was followed by a decrease in ring size. The decrease in size was a factor of three to five times that of the ring prior to moving onto the slope region. They speculate that the cause for the increase and subsequent decrease in size was due to an interaction with another anticyclone to the south.

Several studies showed that cyclonic flow structures are associated with Loop Current rings. Austin (1955) and Nowlin and McLellan (1967) found high dynamic topography coupled with a slight low to the north in the western Gulf of Mexico. Merrell and Morrison (1981) reported an anticyclone paired with a cyclone in the western Gulf of Mexico. Brooks (1984) found an anticyclonic high centered around 24.5°N 95°W and a cyclonic low centered around 26.5°N 95°W in the western Gulf. The cyclonic circulation was 50 km in diameter and extended below 700 m. A current of 10 cm/sec was observed at this depth. Brooks and Legeckis (1982) found an anticyclonic-cyclonic pair centered at 23°N 95.5°W–26°N 95°W. Elliot (1982) and Vukovich and Waddell (1991) also reported an anticyclonic-cyclonic pair in the same general area of the western Gulf of Mexico. The results obtained by Cochrane and Kelly (1986) and Dinnel and Wiseman (1986) in the northwestern Gulf of Mexico can be explained by the presence of a cyclonic flow pattern. Vukovich and Maul (1985) described several cyclones in the eastern Gulf of Mexico. Müller-Karger *et al.* (1991) indicated several cyclonic flow structures in both the advanced very high resolution radar (AVHRR) data and the coastal zone color scanner (CZCS) data.

Hofmann and Worley (1986) inferred the deep circulation of the Gulf using inverse methods from a hydrographic survey of the entire Gulf. They showed a large cyclonic gyre in the western Gulf opposing the anticyclonic surface cir-

culation; however, they cautioned that there were no observations available for verification.

There have been a number of studies devoted to the analysis of drifters in the Gulf of Mexico. Lewis and Kirwan (1985) studied Loop Current ring topography and noted the vorticity changes of a ring as it made its westward transit across the Gulf. They also indicated that these rings interact with the northwestern Gulf of Mexico shelf region to form cyclones, which may be a mechanism for the negative vorticity from the rings to be assimilated in the Gulf. Lewis and Kirwan (1985) also suggested that the occurrence of a "peanut-shaped" orbit in the drifter tracks may be indicative of the merging of two rings. Kirwan *et al.* (1988) concluded that the distortion seen in the drifter paths around 94°W can be attributed to the interaction of rings with the continental slope topography and/or slope circulation.

Loop Current rings are immense in size. In panel *a* of Figure 1, the cruise tracks for expendable bathythermograph (XBT) transects through a ring are shown. In panel *b* of Figure 1, the span of a ring between the maximum thermal gradients is about 300 km. Thus Loop Current rings have a diameter three times that of Gulf Stream rings which are about 100 km (Lai and Richardson, 1977 and Doblar and Cheney, 1977). The depth of the 10° isotherm is about 650 meters. The 5° isotherm is usually depressed to 1200 meters (Elliot, 1982). If the mean radius is assumed to be 150 km and the depth of a ring is 1.2 km, then the volume of a ring is about 8.4 x $10^5 km^3$. As the total volume of the Gulf of Mexico

is 2.3 x $10^6 km^3$ (Wilson, 1967) then a typical ring corresponds to approximately 4% of the total volume of the Gulf of Mexico water mass. Given a ring generation of three rings per year (Indest *et. al*, 1989) and each with a ring lifespan of one year then the Gulf receives one eighth of its total water mass yearly from the rings.

As 4% of the Gulf's volume regularly impinges upon the western slope, then what is the fate of these large water masses in the western Gulf or restated, how does 12% of the Gulf's volume leave the western boundary each year? Merrell and Morrison (1981) and Merrell and Vasquez (1983) showed that along the western slope the rings were paired with cyclones and an eastward offshore transport of 30 Sv was found between a cyclone-anticyclone pairing. Thirty Sverdrups is comparable to the transport of the Yucatan Current into the Gulf through the Yucatan Straits, as well as of the Florida Current flowing out of the Gulf. Müller-Karger *et al.* (1991) showed several indications of offshore transports along the Texas and Louisiana slopes. They speculated that a cyclonic flow was generated when an anticyclonic ring moves into shallower water

As one of the dominant features of the Gulf's circulation, Loop Current rings have spawned much modeling work. Much of the dynamics of eddy shedding by the Loop Current and the general circulation of the Gulf of Mexico was elucidated by Hurlburt and Thompson (1980, 1982) with a two-layer nonlinear primitive equation model. Walsh *et al.* (1989) modelled the entire Gulf of Mexico to study what effect rings had upon the biological and chemical distributions.

Smith and O'Brien (1983) examined the interaction of a ring with the western slope of the Gulf of Mexico. As the ring moved into shallower water the flow accelerated. This caused an asymmetric distribution in the flow field. As the northward flow of the western half of the ring was greater than the southward flow of the eastern portion of the ring, the ring moved toward the north. They also found that the asymmetric flow produced offshore movement for anticyclones or onshore propagation for cyclones. Other effects such as large scale shear flow may also induce asymmetries in the rings which may move the ring in other directions.

Using a two-layer nonlinear primitive equation model similar to that of Hurlburt and Thompson (1980), Smith (1986) showed for an anticyclone migrating onto the western slope of the Gulf of Mexico that in the lower layer there was a strong offshore cross-isobath flow on the northern edge of the anticyclone which acquired cyclonic relative vorticity as it flowed into deeper water. This cyclonic flow excited comparable motion in the layer above it through vortex stretching at the interface. After these simulated anticyclones encountered topography, two things happened dependent upon the lower layer flow — 1) if the lower layer flow was strong, the anticyclone moved eastward; 2) if the flow in the lower layer was weak, the anticyclone moved towards the north.

In his analysis of a Somali Current model, Cox (1979) showed that when a ring approached the coast, a band of vorticity developed between the boundary and the ring. This band of vorticity was advected north, along the boundary,

and then to the east along the northern edge of the anticyclone. As this band of vorticity was advected offshore a cyclonic flow developed on the northern edge of the anticyclone. Cox (1979), Smith and O'Brien (1983) and Smith (1986) showed that this readjustment of vorticity may cause an anticyclonic eddy to move to the east or offshore. Cox (1976 and 1979) also showed that the nonlinear terms are responsible for energy transfer into the eddy during this period and a significant portion of this energy was lost later via vertical mixing.

With questions of the interaction of a ring with a sloping bottom effectively addressed in earlier studies, the next step is to focus on the interaction of a ring with another anticyclonic ring in the western slope region of the Gulf of Mexico. There are several questions to be addressed. What happens to a ring when it interacts with a fossil ring? What causes the offshore transport and what process is responsible for the occurrence of cyclones? We examine these questions with observations from several rings along with simulations from a numerical model. Specifically, we estimate several integral quantities from the model data and apply the results to explain the observations in a consistent dynamical framework.

3. Drifter Observations of Loop Current Rings

This section first describes an analysis which estimates several kinematic properties of drifter data from a number of eddies in the western Gulf of Mexico. Then a description of the drifter tracks and the estimates from the analysis is given. The kinematic properties estimated here are normal deformation, shear deformation, vorticity and the position of the ring center. The results presented in this section demonstrate a marked change in the dynamics of the rings as they near the western slope.

3.1 Kinematic Analysis

The analysis routine used to determine the kinematic properties was first proposed by Kirwan (1984) and extended by Kirwan *et al.* (1988). The routine inverts Lagrangian path data to obtain the desired kinematic properties, namely the shear and normal deformations, the local vorticity and the positions of the ring center.

The observed drifter velocity $(u,\ v)$ is decomposed into a ring translation $(U_T,\ V_T)$ and a swirl $(u_s,\ v_s)$,

$$u = U_T + u_s$$

$$v = V_T + v_s.$$

Following Okubo (1970) and Kirwan, *et al.* (1984a), a model for the swirl velocities is:

$$u_s = \tfrac{1}{2}[(d + a)x] + \tfrac{1}{2}[(b - c)y] \tag{3.1}$$

$$v_s = \tfrac{1}{2}[(b + c)x] + \tfrac{1}{2}[(d - a)y]. \tag{3.2}$$

Here (x, y) are the components of the present drifter position relative to the center of the ring, i.e., a local flow center. The other parameters, a, b, c, and d, have various interpretations (Okubo, 1970 and Kirwan, *et al.*, 1984a). If these parameters are constant or slowly varying over the time interval of interest, they approximate the normal deformation, shear deformation, local vorticity and horizontal divergence, respectively. In Kirwan *et al.* (1988), they are used to define the elliptical structure of particular drifter orbits.

Okubo (1970) presents a general solution to equations (3.1) and (3.2). The procedure is to apply this solution for equations (3.1) and (3.2) to every time interval between drifter positions. Thus for the interval $t_k \leq t \leq t_{k+1}$, one obtains

$$u_k = U_{Tk} + \tfrac{1}{2}[(d_k + a_k)x_k] + \tfrac{1}{2}[(b_k - c_k)y_k] \tag{3.3}$$

$$v_k = V_{Tk} + \tfrac{1}{2}[(b_k + c_k)x_k] + \tfrac{1}{2}(d_k - a_k)y_k], \tag{3.4}$$

where

$$\begin{aligned} x_k = \{&exp\{[r_{1k}(t - t_k)][X_k(\sqrt{a_k^2 + b_k^2 - c_k^2} + a_k) + Y_k(b_k - c_k)]\} \\ &- exp\{[r_{2k}(t - t_k)][X_k(a_k - \sqrt{a_k^2 + b_k^2 - c_k^2}) + Y_k(b_k - c_k)]\}\} \\ &\div 2\sqrt{a_k^2 + b_k^2 - c_k^2} \end{aligned} \tag{3.5}$$

$$y_k = \{exp\{[r_{1k}(t-t_k)][X_k(b_k+c_k)+Y_k(\sqrt{a_k^2+b_k^2-c_k^2}-a_k)]\}$$
$$+exp\{[r_{2k}(t-t_k)][-X_k(b_k+c_k)+Y_k(\sqrt{a_k^2+b_k^2-c_k^2}+a_k)]\}\}$$
$$\div 2\sqrt{a_k^2+b_k^2-c_k^2} \qquad (3.6)$$

In equations (3.5) and (3.6), (X_k, Y_k) are the coordinates of the drifter in question at time $t = t_k$ relative to the ring center and,

$$r_{1k} = \tfrac{1}{2}(d_k+\sqrt{a_k^2+b_k^2-c_k^2}) \qquad (3.7)$$

$$r_{2k} = \tfrac{1}{2}(d_k-\sqrt{a_k^2+b_k^2-c_k^2}) \qquad (3.8)$$

are the eigenvalues of the matrix

$$M = \tfrac{1}{2}\begin{pmatrix}(d_k+a_k) & (b_k-c_k)\\ (b_k+c_k) & (d_k-a_k)\end{pmatrix}.$$

From (3.7) and (3.8), it is seen that if the eigenvector, r_{ik}, is complex then the components are complex conjugates which produce real periodic solutions characteristic of swirl velocities of drifters trapped in a ring.

The procedure used by Kirwan *et al.* (1988) is to invert the path data, (3.3) and (3.4), for a, b, c, d, (x, y), and (U_T, V_T). The basis for this inversion is a Taylor expansion in time about the instant t_k of the velocity vector. From the left-hand side of (3.3) and (3.4) one obtains

$$u(t) = u(t_k)+u'(t_k)(t-t_k)+u''(t_k)(t-t_k)^2/2+u'''(t_k)(t-t_k)^3/6 \qquad (3.9)$$

$$v(t) = v(t_k) + v'(t_k)(t - t_k) + v''(t_k)(t - t_k)^2/2 + v'''(t_k)(t - t_k)^3/6 \quad (3.10)$$

for the interval $t_k \leq t \leq t_{k+1}$. The primes denote differentiation with respect to time. Each of the terms on the right-hand side of (3.9) and (3.10) may be calculated from the velocity record using centered finite differences.

The analytical solutions, equations (3.5) and (3.6), are expanded in a Taylor series, as well. After expanding and equating the coefficients of the appropriate powers with equations (3.9) and (3.10), a system of simultaneous nonlinear equations is obtained for each time interval. With the subscript, k, suppressed, these are:

$$u = \tfrac{1}{2}[X(a + d) + Y(b - c)] + U_T \quad (3.11)$$

$$v = \tfrac{1}{2}[X(b + c) + Y(d - a)] + V_T \quad (3.12)$$

$$4u' = X[(d + a)^2 + b^2 - c^2] + 2Yd(b - c) \quad (3.13)$$

$$4v' = 2Xd(b + c) + Y[(d - a)^2 + b^2 - c^2] \quad (3.14)$$

$$8u'' = X[(d + a)^3 + (b^2 - c^2)(3d + a)] + Y(b - c)(3d^2 + a^2 + b^2 - c^2) \quad (3.15)$$

$$8v'' = X[(b + c)(3d^2 + a^2 + b^2 - c^2) + Y[(d - a)^3 + (b^2 - c^2)(3d - a)] \quad (3.16)$$

$$16u''' = 4X[(a^2 + b^2 - c^2 + d^2)^2 + 4d^2(a^2 + b^2 - c^2) + 4ad(a^2 + b^2 - c^2 + d^2)] + 4Yd(b - c)(a^2 + b^2 - c^2 + d^2) \quad (3.17)$$

$$16v''' = Xd(b + c)(a^2 + b^2 - c^2 + d^2) + Y[(a^2 + b^2 - c^2 + d^2)^2 + 4d^2(a^2 + b^2 - c^2) - 4ad(a^2 + b^2 - c^2 + d^2)]. \quad (3.18)$$

These eight equations are inverted at each time step for X, Y, U_T, V_T, a, b, c and d. This may be done from the observations without knowing a, b or c, *a priori* for

$$det(M) = -4(u''v''' - u'''v'')/(u'v'' - v'u'') = M^2$$

$$Tr(M) = (u'v''' - v'u''')/(u'v'' - v'u'') = d.$$

Insertion of M^2 and d, calculated from the above into equations (3.11) – (3.18) yields,

$$X = 8(u'M^2 - 2u''')/M^4 \quad (3.19)$$

$$Y = 8(v'M^2 - 2v''')/M^4 \quad (3.20)$$

$$a = -(u'v''' + u'''v' - 2u''v'') \div (u'v'' - u''v') \quad (3.21)$$

$$b = -[-(u'u''' - v'v''') + (u''^2 - v''^2)]$$

$$\div (u'v'' - u''v') \tag{3.22}$$

$$c = -[(u'u''' + v'v''') - (u''^2 + v''^2)]$$

$$\div (u'v'' - u''v') \tag{3.23}$$

As all the other terms are known, the final step, calculating U_T and V_T, is straightforward. The kinematic parameters are then estimated for the next time step.

3.2 Drifter Analysis

Drifters 1598, 1599 and 1600 represent parcel flow paths of the 1981–1982 ring which impinged upon the western Gulf of Mexico in late 1981. The path of drifter 1599 is shown in Figure 2a. Note the "peanut-shaped" track of drifter 1599 outlined in Figure 2a. Within the outline, the center path (the dashed lines) suggests a readjustment of the flow field as the ring nears the slope region. Around 23.5°N 94.5°W, the center tracks shows the tendency for the ring to move offshore. The ring then moves northward.

In Figure 2b, the normal and shear deformations and vorticity are shown in panels *a*, *b*, and *c*, respectively. Note the signal for each time series shows a rapid transition between positive and negative values. This type of signal pattern may be indicative of a ring interacting with either a fossil ring or topography.

This correlates with the center track shown in Figure 2a. For drifter 1599, the interaction with topography occurs around day 410.

Drifter 3374 is entrained in the 1983–1984 anticyclone shown in Figure 3a. There is a gap in the trajectory due to a loss of transmissions from the drifter. The path in the mid-gulf shows evidence of a "peanut-shaped" track with a northwest to southeast orientation centered around 24°N 94.25°W. The trajectory along the slope region shows the northwest movement of the 1982–1983 ring. Note the smaller curved tracks in the center of the ring.

In Figure 3b, the three kinematic properties of normal and shear deformations and vorticity are presented in panels *a*, *b*, and *c*, respectively. From this set of time series, the interaction is occurring around day 360. Although the shear deformation does not depict this interaction, the normal deformation is increasing and the vorticity is decreasing on day 360. Note in Figure 3 that this is the time period when a "peanut-shaped" orbit is seen.

The path of drifter 3375 shown in Figure 4 is a good example of a "peanut-shaped" trajectory. Note the drifter takes a southerly route at 24.5°N to about 22.5°N in ten days. This corresponds to a flow speed in excess of 1.5 m/sec to the south.

Drifter 5495 is initially seeded in an old Loop Current ring but leaves it and becomes entrained in another Loop Current eddy which follows the south-southwest migration route as depicted in Figure 5. As the ring approaches the

slope region, the rotational period of the drifter increases. The center track shows a slight southerly readjustment around 23°N 94°W.

As is evident from the path of drifter 3378 shown in Figure 6a not all of the rings follow a southerly route. The drifter suggests that the ring interacts strongly with the western topography. Note the "peanut-shaped" orbit oriented northwest to southeast is outlined in red. This drifter shows the eddy moving towards the south after interacting with the western slope. Note the displacement to the south from 24.5°N 94.25°W to 22.75°N 93.75°W encompasses 200 *km* in 10 days. The large excursion from the southernmost track below 22°N to 25°N takes 20 days and is over 170 *km*.

In Figure 6b, the normal and shear deformations and vorticity are shown in panels *a* through *c*, respectively. In all three panels, there is a rather dramatic series of spikes around day 6180 which indicates the ring is adjusting to a different flow regime. Note the fluctuations in the vorticity signal, starting around day 6375. This is when the drifter was in a "peanut-shaped" orbit.

Drifter 3353, shown in Figure 7a, leaves a ring called Ghost Eddy and became entrained in what is called Eddy E or Fast Eddy. There is a divergence and convergence as the ring nears topography. The center track shows a readjustment occurring around 24.75°N 94.75°W. This drifter track is interesting in that as the ring moves northeast, the drifter becomes briefly involved in a cyclonic flow field

(26.75°N 93.5°W, 25°N 92°W) and then becomes entrained in an anticyclonic circulation around 25°N 91°W.

The three time series of normal deformation, shear deformation and vorticity for drifter 3353 are shown in Figure 7b, panels *a*, *b*, and *c*, respectively. Although there are small spikes around day 140 in the normal and shear deformation signals, the interaction of the ring with topography is clearly evident in the vorticity time series. The latter part of the signal is erratic due to the drifter experiencing various anticyclonic and cyclonic flow regimes.

The trajectory of drifter 3379 is depicted in Figure 8a. It is entrained in an anticyclone and later shows evidence of entrainment by the Bay of Campeche cyclone, a cyclonic feature that persists in the southwestern Gulf of Mexico. Note the large "peanut-shaped" drifter track and the concomitant readjustment to the south displayed by the center track within the red box. After interacting with the slope, the drifter track displays a large anticyclonic circular path. At 25.5°N 95.5°W, the drifter suddenly heads southward and traverses a little less than 700 *km* in 100 days. The drifter then follows a cyclonic path and returns to the anticyclone to the north, follows another "peanut-shaped" orbit, heads south again and is again entrained in the Bay of Campeche cyclone.

As can be seen in panels *a*–*c* of Figure 8b, the time series of the kinematic parameters of drifter 3379 fluctuate wildly. However, the interaction of the ring

with the slope is evident in all signals around day 130. Once again, the drifter is experiencing different flow regimes and as a result the signals are quite noisy.

Drifter 3345 is shown in Figure 9. It is placed in an anticyclone and follows it as it moves westward towards the south-southwest. Note the half-peanut shape in the latter part of the trajectory. The center paths shows the ring rebounds offshore at 23.5°N 94.0 °W.

Drifter 3347, shown in Figure 10, seems to be near the center of the anticyclone drifter 3345 is in as the path orbits traverse less distance than those of drifter 3345. The center track shows the south-southwest movement of the ring. When the edge of the ring enters shallower waters there is a slight divergence of the trajectory at 23.5°N 95°W. Also, there is an abrupt change from the north to the south in the center track at this location.

Any study which uses drifter trajectories is subject to potential problems. One of these problems is the drifter may experience extraneous drag. Another problem is that they may not follow the same parcel of water throughout their lifetimes. In this paper it is assumed that the drifters do follow the same water parcels.

From these data, a tenative scenario emerges. A Loop Current ring migrates westward until its outermost fringes interact with the topography or with another older ring. An abrupt change in the kinematics of the ring occurs, the ring reacts to its new environment and moves toward the north. This scenario suggests that there

is some sort of readjustment of the dynamics when the ring nears the topography or another ring. This readjustment is depicted in the model results. The evolution of several processes as this particular event occurs and during this readjustment is the subject of this dissertation.

In this section, the observations and kinematic analysis show that Loop Current rings undergo a rather dramatic shift or rearrangement of the forces operating upon them. This is evident not only in the "peanut-shaped" orbit but also from the abrupt changes in the time series of the kinematic properties. This raises the question, "What process or processes are responsible for the "peanut-shaped" orbits?"

4. Integral Quantities

In order to examine the interaction of rings with topography and other flow structures the approach taken in this section is to follow the evolution of integral balances of volume, energy, angular momentum, potential vorticity and enstrophy in several rings. This is accomplished by calculating at each time step, the appropriate quantity in either a Loop Current ring or cyclonic ring from the model results. These quantities may then be compared with hydrographic data, drifter data and moored current meter data.

The integral properties for the upper layer are calculated from the following formulae:

$$\begin{aligned} volume &= \int\int h\,dx\,dy \\ &\cong \sum_{i=y_0}^{y_1}\sum_{j=x_0}^{x_1} h_{ij}\triangle x\triangle y \end{aligned} \tag{4.1}$$

$$\begin{aligned} kinetic\ energy &= \int\int [\tfrac{1}{2}(u^2 + v^2)]\, h\,dx\,dy \\ &\cong \sum_{i=y_0}^{y_1}\sum_{j=x_0}^{x_1} (\tfrac{1}{2}(u_{ij}^2 + v_{ij}^2)h_{ij}\triangle x\triangle y \end{aligned} \tag{4.2}$$

$$\begin{aligned} potential\ vorticity &= \int\int \left(\frac{\zeta + f}{h}\right) h\,dx\,dy \\ &\cong \sum_{i=y_0}^{y_1}\sum_{j=x_0}^{x_1} \left(\frac{\zeta_{ij} + f}{h_{ij}}\right) h_{ij}\triangle x\triangle y \end{aligned} \tag{4.3}$$

$$\begin{aligned} \textit{angular momentum} &= \int\int [(xv - yu) + \tfrac{f}{2}(x^2 + y^2)]\, h\, dx\, dy \\ &\cong \sum_{i=y_0}^{y_1} \sum_{j=x_0}^{x_1} [(x_{ij}v_{ij} - y_{ij}u_{ij}) \\ &\quad + \tfrac{f}{2}(x_{ij}^2 + y_{ij}^2)]\, h_{ij}\Delta x \Delta y \end{aligned} \tag{4.4}$$

$$\begin{aligned} \textit{enstrophy} &= \int\int \zeta^2\, h\, dx\, dy \\ &\cong \sum_{i=y_0}^{y_1} \sum_{j=x_0}^{x_1} \zeta_{ij}^2 h_{ij} \Delta x \Delta y, \end{aligned} \tag{4.5}$$

where h, u, v are the layer thickness, east-west velocities, north-south velocities, respectively and f is the Coriolis parameter. The grid spacing in the east-west and north-south directions are Δx and Δy, respectively and the local vorticity, $\zeta = \frac{\partial v}{\partial x} - \frac{\partial u}{\partial y}$. The estimates are subscripted with i, j, so the estimate of vorticity is $\zeta_{ij} = \frac{v_{ij}}{\Delta x} - \frac{u_{ij}}{\Delta y}$ where i and j are the indices defining the model ring in the x and y directions, starting with x_0, y_0 and ending with x_1, y_1. For the estimate of the angular momentum, x_{ij} and y_{ij} are the distances from the center of the eddy which is defined at the point the layer thickness, h_{ij}, is a maximum/minimum for anticyclonic/cyclonic rings.

Every two model days, the integral dynamical parameters for each ring are calculated from the velocity vector plots by selecting a rectangular region that encloses the ring and the appropriate coordinates are recorded. The ring periphery is defined at the point when the height field differences from the mean are zero. At each time step, the velocities and layer thicknesses are extracted from the model

data. The estimates of the integral properties are then calculated using equations 4.1 – 4.5.

One source of error in these estimates is due to the 10 km model grid spacing. The error estimate for the area calculations is approximately 20% for a ring with a 100 km radius. Thus, the volume of a ring with a depth of 300 m is approximately $9.4x10^{12}m^3$. The 300 m depth was chosen for comparison with the upper layer model results and corresponds to the 20°isotherm shown in Figure 1. A conservative error estimate for the kinetic energy, potential vorticity, angular momentum and enstrophy is 30%. There is another source of error in these estimates. During the time the rings are merging (model days 1830–1840), the exact boundary of the ring is not apparent and a subjective estimate is made. The estimates during this period fluctuate and are not reliable.

The approach taken here is to use the model as a source of data. In this way, the evolution of specific mesoscale processes, namely, the interaction of two anticyclones, may be studied by estimating these integral quantities. The intent is to compare model data with observations. As the model data is an "experimental" ocean, treating it as equivalent data will assist in answering several questions regarding these interactions.

5. The Numerical Model and Results

This section describes the numerical model and the results obtained from a 90 day simulation. The first subsection describes the model, its suitability for this analysis and an error analysis. The next subsection describes the results from the model—layer thicknesses, velocities and integral quantities—for several anticyclones and cyclonic flow structures.

5.1 Model Description

The model used in this study is an improved version of the two-layer primitive equation model of Hurlburt and Thompson (1980, 1982). It is a hydrodynamic primitive equation ocean model employing a semi-implicit time scheme on a β-plane with a free surface and is formulated on the Arakawa C grid (Wallcraft 1985, 1986). The Helmholtz equations derived from the semi-implicit scheme are solved with a variation of the method described by Hockney (1965). For the rectangular regions, this method is a FACR(l) fast direct solver (Press *et al.*, 1988, p. 672). The open outflow boundary conditions follow a variant of Orlanski's (1976) radiation condition. Some of the improvements include the incorporation of full-scale topography and solving for the non-rectangular regions using the capacitance matrix technique of Buzbee *et al.*, (1971).

The question arises as to the suitability of the model for this analysis. As established by Kirwan *et al.* (1988, 1990) and Indest *et al.* (1989), this eddy-resolving general circulation model adequately portrays many of the observed features in the Gulf. Vorticial structures appear in the numerical model which are similar to those observed. Loop Current eddy shedding, westward migration through the abyssal Gulf and a northern migration parallel to the western slope in the Gulf of Mexico have all been observed. These similarities indicate that the vorticity balances found in the model may be similar to those responsible for ring behaviour in the Gulf.

As shown in Figures 11 and 12, the path of a simulated ring is quite similar to that of the actual path. The cyclonic-anticyclonic pair found along the western boundary by Merrell and Morrison (1981) and Merrell and Vasquez (1983) also occurs in the model simulations. The fusion of two rings described by Lewis *et al.* (1989) is also seen in the model data.

There are some limitations in using this model. The numerical model is a two-layer model and may not adequately portray all of the physics of the system. The results shown here do not include wind forcing. The inflow through the Yucatan Straits in the model may not adequately represent what is happening in the Straits because the vertical distribution of the flow through the Yucatan Straits is not known. Leben *et al.* (1990) find a 25% difference between GEOSAT height data and the model variability. They suggest that this is due to the model

not including a variable transport through the Yucatan Straits which is known to vary by almost 10 Sverdrups about a mean of 30 Sverdrups in the Florida Current (Schott *et al.*, 1988). Kirwan *et al.* (1988, 1990) suggest that in the abyssal Gulf, the model underestimates swirl velocities and overestimates ring period, however, better agreement is found for rings moving along the slope. Furthermore, the model does not perform well in areas where the depth is less than 500 m; but, as can be seen in Figures 11 and 12, the model captures the event of the ring impinging upon the slope.

5.2 Model Results

The results of this section are from the numerical model. This model, initially at rest, reaches a steady state of eddy shedding by a continuous inflow through the Yucatan Straits which is matched by outflow through the Florida Straits. The results presented in this section are from the sixth model year, beginning with model day 1800. At this time, the model is in statistical equilibrium and possesses a nearly exactly repeating nature of shedding Loop Current rings. These results, specifically, the upper layer thicknesses, current velocities and integral quantities, span three model months, days 1800–1890. The results focus on three anticyclones (M1, M2, and M3) and four cyclones (MC1, MC2, MC3, MC4) in the upper layer and the lower layer cyclone, MC5.

During the three model months, an anticyclonic model ring migrates across the abyssal Gulf and interacts with a fossil anticyclone and the slope of the western

Gulf of Mexico. During these interactions there is an indication of a loss of mass and an offshore cross-isobath transport is generated on the northern edge of the interaction. The anticyclone moves towards the north with a pair of cyclones revolving anticyclonically around it. During the interaction of the anticyclone with the fossil ring, flow along the Yucatan isobaths intensifies in the lower layer and the main cyclonic flow pattern of the Campeche Basin of the lower layer is disrupted.

5.2.1 Layer Thickness and Velocities

This section focuses on the layer thicknesses and velocities of anticyclonic and cyclonic model vortices in the western Gulf of Mexico. These structures appear as closed contours in the upper layer thickness plots, Figures 13a–22a, and as coherent axi-symmetric velocity fields of the upper layer shown in Figures 13b–22b. The current vectors for the lower layer flow are shown in Figures 13c–22c. The upper layer heights are contoured at 10 m intervals. For all velocity figures those current vectors less than 5 cm/sec are not shown. The lower layer velocities are scaled a factor of three greater than the upper layer velocities.

The eddies, M1, M2 and M3, and the cyclones, MC1 and MC2, are shown in Figures 13a–c for model day 1800. In Figure 13a, the anticyclone, M1, is approaching the western Gulf. The maximum diameter of M1 is about 330 km. The elliptical orientation of the major axis is approximately northwest to southeast. The maximum thickness of M1 is approximately 340 m at the center, whereas

along the fringes the thickness diminishes to 190 m. The rest thickness in the model is 200 m. Figure 1a shows a typical ring thickness to be about 100 m at its fringe.

Eddy M2 has a diameter of about 550 km. It has a trailing wake which is curling around the cyclonic structure, MC2. The elliptical orientation of M2 is almost due north. Note the cyclonic structures, MC1 and MC2. The thickness of MC1 is about 140 m.

In Figure 13b, the upper layer flow field shows the circulation pattern of three well-defined anticyclones and two lesser-defined cyclonic structures. The M1 ring's flow is between the northern and southern 2000 m isobaths. The flow of M2 is extensive — from 20°to 26°N, a range greater than 600 km. As in the layer contours of Figure 13a, there are two cyclonic structures associated with M2—MC1, at the northeastern edge and MC2, another more intense flow on the eastern side of M2.

MC2 may be a surface manifestation of the lower layer cyclonic circulation of Figure 13c as they are both centered around 23°N 94°W. The large cyclone, MC5, is within the 2000 m lower isobath. Also seen in Figure 13c is the lower layer signature of M1, the anticyclonic circulation centered at 25.25°N 91.75°W. Other upper layer structures may not be seen because of the contour interval.

The results from model day 1810 are shown in Figure 14. Eddy M1 is somewhat more circular than in the previous figure and is moving closer to the western

coast. Note the small wake-like structure on its trailing southeastern portion and the cyclone, MC3, to the east. Eddy M2 is moving closer to the coast. MC1 and MC2 appear to be merging which seems to be squeezing M2 towards the north.

In Figure 14b, the flow in MC2 is intensifying and is shifting farther south possibly due to advection by M2's southerly flow. MC2 is now centered at 22.5°N 94°W. MC1 is not apparent in the top layer flow but another cyclonic structure, MC3, has developed to the east of M1 at 25.5°N 89.5°W. In Figure 14c, the cyclonic structure remains stationary and directly below MC2 but the southward flow is intensifying along the western 3000 m isobath. This suggests the lower layer flow may be an important dynamical process as it may be responsible for the southward migration of the cyclonic wall of Figure 14a. The lower layer signature of the M1 anticyclone remains but is not as defined as it was in Figure 13c.

On day 1820, in Figure 15a, M1 is beginning to merge with M2, separating the cyclonic flows. The anticyclone, M1, is becoming somewhat elliptical with the major axis oriented meridionally. There is a steep gradient just north of M2 with the appearance of a cyclonic flow, MC4, centered at 25.5°N 96.5°W.

In Figure 15b, the surface flow in the area of this gradient is intense. Velocity vectors exceeding the 1 m/sec cutoff are shown as dots. There are cyclonic structures north (MC1) and south (MC2) of the merger. The surface flow of MC2 or the Campeche cyclone is clearly evident in Figure 15b. It is expansive and seems

to be deforming M2. MC1 is intensifying as M1 maintains its westward course, causing a shear effect with M2 upon MC1.

As Figure 15c depicts, the lower layer flow is now dipolar. There is a weak cyclonic flow centered approximately at 25.5°N 94°W, directly below MC1, with MC5, the large cyclonic flow, to the south. MC5 remains within the 2000 m isobath, centered around 22.25°N 94°W. The flow to the northeast along the southern topography where the 1000, 2000 and 3000 m isobaths are relatively close together is intensifying. There is also evidence in the lower layer of the upper layer cyclonic flow generated by the intense transport along the 25°N parallel centered at 25.5°N 96.5°W.

In Figure 16a, MC1 and MC4, merged to form the cyclone, MC4. MC4 is moving toward the northeast while MC2 has shifted towards the northwest and is more expansive. The two anticyclones continue to merge. There is a steep gradient at the northern juncture of the merger from 25.0°N 95.0°W to 25.0°N 93.0°W. In this area the layer thickness increases from 160 m to 280 m in 25 km. The maximum thickness of M1 and M2 is about 330 m. This coalescence may be the reason drifters follow a "peanut-shaped" orbit in this area. Drifter 3375 is shown atop Figure 16a for comparison. The model layer thickness is quite similar to the drifter path. Although a displacement of 100 km would produce a better fit, this overlay shows a remarkable similarity despite the variability of the rings evident

in the section describing the drifters. Other reasons for this displacement may be that the model is only two-layered and there is no wind forcing present.

Depicted in Figure 16b is the intensification of the transport event along the 25°N. The transport extends from 25.5°N 96.5°W to 25.5°N 93°W. In fact, comparing Figure 15b with this one shows the band of intense flow moves anticyclonically to the north of M2. MC1 is seen quite clearly in the upper layer currents. The cyclonic circulatory pattern of MC3 continues to develop east of the merging rings, centered at 24.5°N 90.75°W, and MC2, the Campeche cyclone, is clearly evident in the upper layer currents.

In Figure 16c, there is an anticyclonic flow in the northern abyss and a "peanut-shaped" cyclonic flow pattern with lobes centered at 22.5°N 94°W and 24°N 92°W which feeds the northeastern isobath flow. The isobath flow persists and is part of the third flow structure, the anticyclone.

Figure 17a shows the old eddy M1 is more elongate in the north-south direction as the anticyclones, M1 and M2, begin to separate. MC1 is intensifying and is moving towards the northeast. Note that M1's volume is less than that of the previous model day — its maximum thickness is now about 280 m as opposed to 330 m in Figure 15a. This is indicative of an ejection of mass probably due to the interaction of M1 and M2.

Figure 17b shows the upper layer flow field of M1 and M2 separating. Note the intense flow at the northern edge of M2 along the 25°N and then north along

the western edge of M1, creating another cyclonic structure which is not labeled. The Campeche cyclone, MC2, has a well-defined southerly flow on its western edge; but the flow is less intense on its eastern side.

In Figure 17c, the flow in the lower layer, centered at 24°N 92°W is intensifying and is centered southeast of the separation of M1 and M2 in the upper layer. The anticyclonic flow of the lower layer in Figure 17c seems to have a small cyclone to the west of it around 23.75°N 95.5°W. The northeast isobath flow is intensifying, perhaps contributing to the generation of the cyclonic flow to the north.

Model day 1850, shown in Figure 18a, depicts eddy M1 attaining a more elliptical shape with the major axis oriented northeast to southwest. M1 is completely separated from M2. M1 now has two associated cyclonic structures, one to the northwest (MC4) and one to the southeast (MC3). Note that the cyclone, MC3, that was originally east of eddy M1 is now to the southeast. A comparison of the layer thickness plots from model days 1850—1880 shows the paired cyclones, to the northwest (MC4) and southeast (MC3), appear to be revolving around eddy M1.

In Figure 18b, the flow over topography of eddy M1's northwestern quadrant is intensifying. The cyclone, MC3, to the northwest of M1 is more coherent than MC4, the cyclone on the southern edge of M1. The Campeche cyclone, MC2,

maintains a coherent cyclonic flow structure. M2 is now merging with M3 and their flows are interacting.

The lower layer flow in Figure 18c shows MC5, a coherent cyclone centered at 24°N 93°W, spanning the entire abyss. The cyclone is almost directly below the point of separation in the upper layer. The lower layer flow along the 3000 m isobath of the western slope persists but the anticyclonic flow of Figure 17c is no longer evident.

Model day 1860 shows the cyclones, MC4 and MC3, are now directly north and south of eddy M1 and the major axis of eddy M1 is due east and west. The southern cyclone, MC3, is enlarging. In Figure 19a, the wave-like pattern again appears to be trailing M2. M2 continues to merge with M3.

As in Figure 19a, the cyclones MC4 and MC3 are now due north and south of M1 in Figure 19b. M1 is diminishing in size and is moving towards the north. Note the southerly flow from M3. In Figure 19b, M3 is diminishing in intensity and there is a southerly flow continuing south along the eastern side of M2. The cyclone MC3 is moving towards the west and now spans 23.5°N and 25.25°N. MC3 may be the upper layer response to the lower layer cyclone, MC5, shown in Figure 19c. The lower layer flow diagram, Figure 19c, shows an intensification centered around 24°N 93.5°W. The northeast isobath flow is gone. The MC5 cyclonic flow in Figure 18c spans the entire abyss and extends into the slope region of the southwestern Gulf of Mexico.

Model day 1870 is shown in Figure 20. As seen in Figure 20a, MC3 is expanding and is beginning to extend towards the south, pushing the trailing wake of M2. M2 is fissioning and generating a new anticyclone, labeled M2′ in Figure 20a. The cyclones, MC4 and MC3, continue to revolve anticyclonically around eddy M1. MC2 is diminishing in size. M2 and M3 continue to interact.

In Figure 20b, the flow of M1 is fairly intense, with the northernmost cyclone, MC4, intensifying. The flow of M3 is diminishing while the southern and eastern flows of M2 in conjunction with MC3 are intensifying. The Campeche cyclone, MC2, remains a coherent cyclonic flow.

The most intense flow in the lower layer occurred on day 1870 where a flow of 34 cm/sec was found. Figure 20c shows that most of this flow is southward along the 3000 m isobath on the western side of MC5, the lower layer cyclone which is centered at 23.25°N 94.25°W. MC3, the cyclone in the upper layer above MC5, is centered a little to the north, at 24°N 94.25°W. Note the northeast flow in the lower layer along the Yucatan 1000–3000 m isobaths is returning.

Eddy spawning may be due to the cyclonic structure of the lower layer (MC5) coupled with the upper layer (MC3) as seen in Figures 20b and 20c. The strong southerly isobath flow may have cleaved M2 into two eddies. The upper layer cyclonic expression, MC3, between the two anticyclones shown in Figure 20b may be the surface manifestation of the lower layer cyclone, MC5.

During model day 1880, shown in Figure 21a, M2 and M2′ have completely separated. Once again there is a cyclonic wall continuing southward seeming to cleave M2′ from M3. The cyclonic wall is extending to the south from 27°N to 22°N. The cyclones, MC4 and MC3, paired with M1 continue to revolve around it. In Figure 21b, there is a surface signature of the cyclonic flow between M2 and M2′. The easternmost cyclone, MC4, of M1 is the stronger of the two. M3 has decreased in intensity. In Figure 21c, the flow of MC5, the lower layer cyclone, centered at 22°N 94.25°W, is still intense. The strong southerly flow to the west of this cyclone persists and the northeast flow has reappeared.

Model day 1890 shows the cyclonic wall is divided into northern and southern cyclones, the southern one extending into the Bay of Campeche. In Figure 22, there are four anticyclonic structures and three cyclonic structures. The Campeche cyclone seems to squeeze M2 against the coastline. The cyclones, MC4 and MC3, are now due east and west of M1; MC4 is more defined than MC3.

Figure 22b delineates the areas of cyclonic and anticyclonic flows with the cyclonic structures due east of M1 being the most energetic but the Campeche cyclone, centered at 21.5°N 94.75°W, remains the largest in diameter. M3 and MC3 are beginning to dissipate.

Figure 22c shows the lower layer cyclone is within the 2000 m isobath and the northeastern flow parallel to the isobaths has intensified to 30 cm/sec. The

lower layer cyclonic flow of Figure 22c is offset from the upper Campeche cyclone; it is centered at 22.5°N 93.75°W.

To summarize, during the ninety model days, M1 migrated across the abyssal Gulf onto the slope and interacted with M2 on days 1820–1850. During this time the upper layer thickness of M1 decreased from 350 m to 280 m and the radius decreased from 200 km to 110 km, an indication of a loss of mass. An offshore cross-isobath transport was generated on the northern edge of the M1/M2 interaction. M1 then moved towards the north with a pair of cyclones revolving anticyclonically around it. During the interaction of M1 and M2, flow along the Yucatan isobaths increased as the main cyclonic flow pattern of the Campeche Basin was disrupted in the lower layer. The cyclone, MC1, dissipated but after a few model days, another cyclone, MC4, appeared. The anticyclones persisted throughout the model run and on day 1880, M2 fissioned into two anticyclones.

5.2.2 Integral Quantities

In panel *a* of Figure 23, the volume of eddies M1, M2 and M3 are shown for the period 1800–1890. Initially M1 is approximately $7x10^{12}m^3$ but decreases to a level of $2x10^{12}m^3$ around day 1850. Thus M1 lost 70% of its mass after interacting with M2 in this ninety day simulation. Initially the volume of M2 is about $7x10^{12}m^3$, from days 1800–1840, reaches its maximum level during the merging event and then decreases to about $7x10^{12}m^3$. The smallest anticyclone

examined is M3; it maintains a volume of approximately $1.5x10^{12}m^3$ throughout the simulation.

The kinetic energy balances are shown in panel *b* of Figure 23. Initially, M1 has a value of about $6x10^{11}joules$ between days 1800–1830 which falls subsequently to $2x10^{11}joules$. M2 initially has an average value of $9x10^{11}joules$ which subsequently drops to an average of $7x10^{11}joules$. M3 remains constant at $1x10^{11}joules$. M1 loses energy as it moves into the slope region and interacts with M2. M2 also loses some energy after it interacts with M1.

In panel *c* of Figure 23, the angular momenta for the three anticyclonic model rings are shown. The angular momentum for M1 is initially $1x10^{19}m^2/sec$, and drops to a value of $6x10^{18}m^2/sec$ after M1 and M2 interact. The angular momentum of M2 starts off with an average value of $9x10^{19}m^2/sec$ then decreases to an average of $2.5x10^{19}m^2/sec$ during days 1820–1860. The angular momentum then increases to $6x10^{19}m^2/sec$ by day 1865 and on day 1890 after fissioning has a final value of $7x10^{19}m^2/sec$.

The angular momentum for M3 is $6x10^{18}m^2/sec$ for the first 60 days then climbs to a value higher than that of M1, $1x10^{19}m^2/sec$. M1 loses angular momentum as does M2. However, M2 gains some after the interaction with M1 and M3. M3 initially has an order of magnitude less angular momentum, yet gains an amount comparable to the value at which the time series for M1 ends.

The time series for potential vorticity is shown in panel *d* of Figure 23. The potential vorticity for M1 is around $7x10^{-3}sec^{-1}$ initially but falls to $2x10^{-3}sec^{-1}$ on day 1860 and remains fairly constant for the final 30 days. The initial potential vorticity value for M2 is about $6x10^{-3}sec^{-1}$ which drops to $5x10^{-3}sec^{-1}$ as M1 interacts with M2. After the interaction with M1, the potential vorticity increases to about $6.5x10^{-3}sec^{-1}$ on day 1860. The potential vorticity of M2 gradually tapers off to a little less than $6x10^{-3}sec^{-1}$ by day 1890. The potential vorticity for M3 remains fairly constant at $1.75x10^{-3}sec^{-1}$ during days 1800–1860, but increases to value greater than that of M1, $2.5x10^{-3}sec^{-1}$.

In panel *e* of Figure 23, the enstrophy time series for each anticyclone is shown. The enstrophy of M1 is fairly constant for the first 30 days at about $2.5x10^4m^2/sec$. After the interaction with M2, it almost reaches a value of $6x10^4m^2/sec$ during day 1860 and then falls to $2x10^4m^2/sec$ for the last 20 days. The enstrophy time series for M2 is roughly an average of $8x10^4m^2/sec$ for the first 30 days and then decreased to around $4x10^4m^2/sec$ on day 1850. It stays constant up to day 1880 where it again increases to a value in excess of $6x10^4m^2/sec$. The enstrophy for M3 remains constant at $6x10^4m^2/sec$. Both M1 and M2 lose enstrophy while M3 gains enstrophy to an extent that is greater than M1's. Note that enstrophy is not conserved.

The time series of kinetic energy for M1 and MC5, the cyclone in the lower layer, are shown in panel *f* of Figure 23. The kinetic energy of the lower layer

cyclone decreases from $8x10^{11} joules$ to $3x10^{11} joules$ as M1 passes over it. There is an increase in MC5's kinetic energy to $1x10^{11} joules$ after the interaction of M1 and M2 while there is a concomitant decrease in M1's kinetic energy from $7x10^{11} joules$ to about $3x10^{11} joules$. This suggests that there may be a transfer of energy from M1 to the lower layer, a transfer that is also shown to occur by Hurlburt and Thompson (1982).

Panel *a* of Figure 24 depicts the volume time series for the cyclones, MC1, MC2, MC3 and MC4. Initially, MC1 has a volume of about $9x10^{11} m^3$, increases to a maximum of $2x10^{12} m^3$ around day 1836 and then decreases to its original value and is no longer a coherent cyclone by day 1850. MC2 begins with a volume of $3x10^{12} m^3$ and rapidly increases to $6x10^{12} m^3$ during days 1818–1824. The volume of cyclone MC2 decreases to about $3.5x10^{12} m^3$ after the interaction of M1 and M2. On day 1806, MC3 has a volume of $2.4x10^{12} m^3$. The volume increases gradually to an average of $6x10^{12} m^3$ after the interaction of M1 and M2 and falls to about $3x10^{12} m^3$. MC4 appeared on day 1838 with a volume of $1x10^{12} m^3$ which rises only slightly and maintains a relatively constant value of $2x10^{12} m^3$ for the remainder of the model run. MC4 is actually the result of a merging of MC1 with a small cyclonic structure that is not depicted in these results.

The energy time series for cyclones MC1, MC2, MC3 and MC4 are given in panel *b* of Figure 24. The energy of MC1 is initially about $1x10^{10} joules$, rises to an average of about $4x10^{10} joules$ during day 1820–1840 and falls to

$3x10^{10} joules$. The energy of MC2 is initially $3.5x10^{10} joules$ and rapidly increases to $1x10^{11} joules$ during days 1818–1824. The energy level drops to an average of approximately $2.5x10^{10} joules$ for the remainder of the simulation.

The energy for MC3 is about $1x10^{10} joules$ initially and gradually increases to $4x10^{10} joules$ by day 1850. It then goes up to about $6x10^{10} joules$ and falls abruptly by day 1880. MC4's kinetic energy fluctuates around $4.5x10^{10} joules$ between days 1840–1890.

The angular momenta for MC1, MC2, MC3 and MC4 are shown in panel *c* of Figure 24. The angular momentum for MC1 is initially $1.5x10^{17} m^2/sec$, increases to a maximum of $1x10^{18} m^2/sec$ on day 1838 and then decreases to a final value of $1.5x10^{17} m^2/sec$ by day 1848. Initially MC2's angular momentum is about $1x10^{18} m^2/sec$ and rapidly increases to the maximum of $1x10^{19} m^2/sec$ on day 1836 and then drops to $1x10^{18} m^2/sec$ by day 1860. Its final value is $3x10^{18} m^2/sec$.

MC3's angular momentum is initially similar to MC2's. MC3 does not increase as rapidly as MC2's but attains its maximum value of $8x10^{18} m^2/sec$ on day 1840; then drops to $4x10^{18} m^2/sec$ in ten days. From day 1860 the value for the momentum fluctuates around $4x10^{18} m^2/sec$. The angular momentum for MC4 is initially $2.75x10^{17} m^2/sec$ on day 1838 and gradually rises to $1.5x10^{18} m^2/sec$ by day 1862. It subsequently falls to an average of $1x10^{18} m^2/sec$ for the remainder of the record.

The time series for potential vorticity is shown in panel *d* of Figure 24. Initially MC1 has a potential vorticity of $1x10^{-3}sec^{-1}$ which increases to a maximum of $3x10^{-3}sec^{-1}$ by day 1836. The potential vorticity then decreases to $2x10^{-3}sec^{-1}$ by day 1846. The potential vorticity for MC2 begins with a value of $3x10^{-3}sec^{-1}$ and increases to $6.5x10^{-3}sec^{-1}$ during day 1816–1824. On day 1836 the maximum value, $1x10^{-3}sec^{-1}$, is attained. The potential vorticity gradually decreases to about $4x10^{-3}sec^{-1}$ but by day 1880 falls to a final value of $3x10^{-3}sec^{-1}$.

MC3 gradually gains potential vorticity—from $3x10^{-3}sec^{-1}$ on day 1806 to about $8x10^{-3}sec^{-1}$ on day 1840. After day 1864, the potential vorticity falls to about $3x10^{-3}sec^{-1}$. MC4 also gradually gains potential vorticity, from an initial value of $2x10^{-3}sec^{-1}$ to a maximum of $4.25x10^{-3}sec^{-1}$ on day 1862 but levels out thereafter to $3.75x10^{-3}sec^{-1}$.

The enstrophy time series for MC1, MC2, MC3, and MC4 are shown in panel *e* of Figure 24. MC1's enstrophy rises from an initial value of $1x10^2m^2/sec$ to $9x10^2m^2/sec$ during the merging of M1 and M2 and falls to $1x10^2m^2/sec$ by day 1846. The enstrophy time series for MC2 starts at a value of $1x10^2m^2/sec$ and increases to about $4x10^2m^2/sec$ from days 1818–1835. The enstrophy falls to $1x10^2m^2/sec$ on day 1850 then increases to about $2x10^2m^2/sec$.

The enstrophy for MC3 remains low for the first half of the record, then on day 1840 increases to $4x10^2m^2/sec$ by day 1862 and subsequently falls by day 1878 to

a final value of $1x10^2 m^2/sec$. The enstrophy for MC4 increases from $5x10^1 m^2/sec$ to $4x10^2 m^2/sec$ by day 1860 and gradually tapers off to $5x10^1 m^2/sec$ by day 1890.

The integral balances of M1 and M2 are not reliable during model days 1825–1840 because the identification of their respective boundaries is not possible while they are interacting. However there are correlations between the balances for M1, M2, MC1 and MC2 before and after the interaction. The volume and energy balances increase for MC1 and MC2 as M2's decrease. As M1 and M2 interact, the volume and energy of the cyclones increase. As M1 moved northward, MC1 dissipates but MC4 appears and its volume and energy increase slightly while M1's decrease.

After interacting with each other M1 loses volume while M2 and MC3, the cyclone east of M1, gains volume. Similar results are obtained for the energy time series. After day 1850, as M2 loses volume, M3 increases in volume as did MC3 and MC4 but not enough to account for M2's loss.

The angular momentum of M2 decreases fairly rapidly after M1 and M2 interact, while that of MC2 increases and subsequently drops. M1 gains a small amount but the value drops after day 1840. M3's angular momentum remains fairly constant; it increases somewhat after M3 interacts with M2.

After M1 interacts with M2, M1's potential vorticity decreases to a level comparable to M3, an older ring, possibly. M2's potential vorticity is fairly constant

for the entire record whereas M3's potential vorticity increases after M3 interacts with M2.

The enstrophy time series show M2 loses enstrophy while M1 gains enstrophy. MC3 and MC4, the cyclones revolving around M1, also gain enstrophy during the time M1 moves above the topography of the northern Gulf of Mexico. When M1 and M2 merge, the enstrophy of MC1, the cyclone between them, increases dramatically. MC2 also gains enstrophy during this time. The enstrophy time series between M2 and MC2 are similar, they only differ in that M2 has a larger variation in amplitude than MC2.

The model results presented in the three previous sections show that when a ring approaches the western Gulf of Mexico it interacts with not only the topography but quite possibly a fossil ring. The interaction results in a loss of volume, a transfer of energy and an intensification of flow on the northern edge of the interacting rings and the appearance of a cyclone in the upper layer. This cyclone persists and revolves anticyclonically around the northward moving anticyclone. In the lower layer, there is a large cyclonic flow pattern, MC5, which is disrupted temporarily by the passage of a Loop Current ring in the upper layer.

6. Comparison of Model Results with Observations

In this section, the model results presented previously are compared with observations—hydrographic data from the western Gulf of Mexico and satellite-tracked drifter data. The comparisons are organized by dynamical event. The migration of the anticyclone and subsequent offshore or eastward movement after impinging upon the slope is presented in the next subsection. A discussion of the merging with a fossil ring and consequent mass loss follows. The cyclones observed both in the model results and in the western Gulf of Mexico are discussed followed by a subsection on the contribution of the lower layer to the dynamics of the system. A discussion of anticyclonic fission is presented in the final subsection.

6.1 Migration and Rebound

In Figures 11 and 12, the center path results from a kinematic analysis of observed and simulated drifters are compared. Two of the center paths are calculated from the numerical model simulated paths (drifters 1 and 2). The other nine center paths are calculated from the observed drifters with buoy identification numbers—1599, 3374, 3375, 5495, 3378, 3353, 3379, 3345 and 3347. Each drifter is seeded in a separate ring generated by the Loop Current between 1981–1989.

Figures 11 and 12 not only demonstrate that at different times six mesoscale eddies followed a similar path in the Gulf of Mexico but the numerical model does an excellent job of simulating the ring dynamics in this area as is reported by Kirwan *et al.* (1988, 1990). Note Figures 11 and 12 support the view of Vukovich and Crissman (1986) that the west southwest path seems to be the preferred way for the Loop Current eddies to migrate across the Gulf of Mexico. The center paths shown in Figures 11 and 12 suggest that when the rings are influenced by the slope or another ring they readjust toward the east then back to the west and then usually migrate to the north. An exception is drifter 3378 for it follows the more northerly path and moves to the south after interacting with the slope; nevertheless, drifter 3378 exhibits the characteristic readjustment. These rebounds usually occur between 95°–94°W.

A scenario similar to that reported by Cox (1979) is seen in Figures 15 – 17 which show M2 along the Mexican coast and a cyclone, MC1, to the north. The interpretation is that the redistribution of vorticity causes movement of the eddy offshore. Thus, when a new ring interacts with another ring along the slope, there is a redistribution of vorticity which is verified by panel *c* of Figure 23. Cox (1979) determined that the nonlinear terms are responsible for energy transfer during the period the vorticity is redistributed. This would imply that the interaction of M2 and MC1 is nonlinear.

6.2 Merger and Mass Loss

There are several accounts of merging of anticyclones in the literature. Observations of the merging of anticyclones are presented by Cresswell (1982) and Cresswell and Legeckis (1987). McCreary and Kundu (1987) establish numerically that merging of anticyclones may take place and according to Nof (1988) merging of anticyclones is inevitable. Cooper *et al.* presented results from a survey of two Gulf of Mexico warm core rings. They found two rings, an older one in the western Gulf adjacent to the west Texas shelf and a second ring recently shed from the Loop Current. The presence of two rings suggests that a merging event is likely.

Cushman-Roisin's (1989) analysis of merging anticyclonic lenses demonstrate that when anticyclones of comparable size are allowed to interact a loss of mass equivalent to 20% of the initial volume may occur. However, the analysis is based on the assumptions of energy, mass and momentum conservation. In Figure 23a, M1 loses 65% of its volume when it impinges upon the slope. However this is for the upper layer only. The volume calculations from Figure 1b correspond quite well to the model volume of Figure 23a. For the 15° isotherm at a depth of 400 m (radius = 200 km), the volume is $5x10^{13}$ m^3. This value is a little less than the average ring volume for M1 in Figure 23a during the days 1800–1830.

Mied and Lindemann (1984) numerically examine the interaction of two anticyclonic Gulf Stream rings and find that, depending upon the values of the viscosity and tracer diffusivity, a mass transfer between model rings of up to 35%

is possible. Here, assuming all of the increase in volume of M2 is from M1, a transfer of 33% of the volume is observed in the model.

Merrell and Morrison (1981) report a transport of 27.5 Sv along the 24.5°N parallel (95°–94°W) in the same general area as the transport occurring during model day 1830 shown in Figure 16. Since a merging event is occurring simultaneously with this transport event in the model, Merrell and Morrison (1981) may have captured part of a merging event in 1980 but due to a lack of resolution and hydrographic coverage, a second anticyclone is not seen in their data. Figure 25 depicts the 15°C isothermal contours from two periods, April 1–12, 1978, shown in panel *a*, and April 12–26, 1978, shown in panel *b*. Panel *a* is quite similar to the model Figure 16. The depth of the cyclonic low is around 150 m and the model layer thickness in the same area is 140 m. The high in Figure 25a is 300 m and for the model layer it is 340 m thick. These comparisons, although between temperature contours and layer thicknesses, imply that the merging of two anticyclones occurs in the Gulf and is directly related to the observed transport of 30 Sverdrups.

A comparison between Figure 25b and model day 1840, shown in Figure 17, indicates a separation of the anticyclones for the temperature contours are closed. This comparison demonstrates that the anticyclones merge partially and then separate as seen in the model results.

The merger of M1 with M2 or the spawning of an additional anticyclone may be the mechanism behind the "peanut-shaped" drifter trajectory as seen in drifters 1599, 3378, 3379 and 3347 shown in Figures 2, 6, 8 and 10, respectively. A portion of the drifter track from 3375 is shown in Figure 16 with the upper layer thickness contours. These "peanut-shaped" orbits are similar to the padlock flow patterns of Nof (1988) according to whom, as long as mass is conserved, merging of anticyclonic flow structures is inevitable and potential vorticity is not conserved. The potential vorticity results in panel *d* of Figure 23 show that this is indeed the case.

The question of what is the fate of a portion of these large water masses is answered in part by the track of drifter 3378 shown in Figure 26. The initial portion of the trajectory shows the "peanut-shaped" orbit which is outlined in Figure 6. Thereafter the drifter makes a large anticyclonic orbit but at the northernmost point the drifter heads due east. At 25°N 88.5°W, drifter 3378 encounters the fringe of the Loop Current and follows it to the north and then south. Finally, the drifter is entrained in the Florida current and comes ashore on one of the Florida Keys.

This drifter track demonstrates that a water parcel may leave the western Gulf of Mexico and traverse the entire Gulf of Mexico after a merging event. A likely mechanism for this is the transport event that is shown to occur concomitantly

with the "peanut-shaped" orbit of the drifter. Note that the drifter began its eastward migration around 25°N, the latitude where the offshore transport occurs.

6.3 Cyclones

Several cyclones are seen in the model results, but is the occurrence of so many cyclonic flow structures in the western Gulf of Mexico likely? This section attempts to reinforce the model results by examining several other studies, both observational and numerical in nature, which describe anticyclonic/cyclonic flow structures similar to those found in the model.

The pairing of an anticyclone with one or more cyclones is evident from the model results— M1, an anticyclone, is paired with two cyclones, MC3 and MC4; M2, the westernmost anticyclone is paired with MC1 and MC2, to the north and south, respectively. This type of situation, that is, the pairing of an anticyclone with a cyclone in the western Gulf of Mexico, is well documented in the observational literature.

A comparison of the upper layer model thickness with an isothermal contour map of the Gulf of Mexico demonstrates how effective the model may be. In Figure 27a from Brooks and Legeckis (1982), the contours for the 14°C surface in the western Gulf of Mexico are shown. There is a large cyclone to the north of a large anticyclone. The broad band shows the front or the tongue of a cool water intrusion. Note the wave-like structures at the northeastern section of the

anticyclonic contours. Figures 27b and 27c depict the contours along 95°W for temperature and salinity, respectively. The intensity of the cyclonic flow is clearly evident; note that it extends below 800 m. This may be compared to the lower layer flow shown in Figure 16 where the surface cyclonic flow is reflected in the lower layer flow about a center located at 25°N 95°W. Thus, the cyclone observed by Brooks and Legeckis (1982) may be the result of a merger of two anticyclones along the slope.

Another comparison of the model data may be made with the isothermal data from SAIC (1988). The depth of the 8°C isotherm for the western Gulf during April 14 – November 24, 1987 is shown in Figure 28 from SAIC (1988). There is a qualitative similarity to Figure 17a. On the isothermal map, there are cyclonic structures in the vicinity of 27°N 93°W and 24.5°N 90°W which correspond to MC4 (26°N 93.5°W) and MC3 (25°N 90.5°W) of Figure17a, respectively. Figure 28 also depicts anticyclonic structures centered at 25°N 95°W and 25°N 92°W which correspond to the model anticyclones, M2 (24.5°N 95°W) and M1 (26°N 92.5°W), respectively. Although the comparison is between layer thicknesses and isotherms, the degree of similarity is remarkable.

In addition to observational evidence of cyclonic structures there are several numerical results which further support these results. Meid and Lindemann (1979) showed that as an anticyclone evolves on a β-plane, a cyclone is generated on its eastern side. Thus, MC3 is an expected occurrence in model day 1810. As seen in

model days 1840 through 1890 the two cyclones, MC3 and MC4, revolved around the anticyclone, M1. According to Hooker (1987), a cyclone to the east of an anticyclone tends to rotate anticyclonically towards the southeast portion of the anticyclone. This is also seen in the numerical results of Mied and Lindemann (1984). This occurs in the numerical model as the MC3 cyclone to the east of M1 does indeed move towards the southeast in an anticyclonic fashion. There is also some indication of a southwestward migration of cyclonic flow in the initial stages of the path from drifter 5839 shown in Figure 29.

In addition to these hydrographic and numerical studies, cyclonic flow structures are found in drifter trajectories and Hamilton's (1990) current meter observations. As mentioned in the preceeding paragraph, drifter 5839 exhibited cyclonic orbits in Figure 29. There is further observational evidence for the northern model cyclone, MC4. In Figure 7, the path of drifter 3353 reinforces the model results as there is northern cyclonic orbit centered around 27°N 92°W. In Figure 19a, MC4 is centered at 27°N 92°W.

From these comparisons it is seen that an anticyclonic ring migrates to the west and may interact with a fossil ring along the coast. This interaction results in the formation of several cyclones. These cyclones are energetic and they tend to move with the anticyclones. This movement may be an explanation for the ephemeral nature of these cyclonic structures.

The generation of these cyclones may due to an instability. The wave-like structure or cusp on the northeast edge of the anticyclone shown in Figure 27 which is also depicted in the model Figure 15a may be a Helmholtz-Kelvin instability which is due to the offset of the center of mass with the flow field (Stern, 1987). This instability is potentially a mechanism for the generation of cyclonic vorticity (Lewis *et al.*, 1989). This structure is also found in Deem and Zabusky's (1978) nonlinear dispersive wave solution for a perturbed finite-area vortex region.

From the model results presented here and the observational evidence it is likely that these cyclonic flow structures are ubiquitous in the Gulf. The presence of several cyclones may increase the likelyhood for mixing to proceed. Thus, these cyclones may play a role in which Gulf Common water is created from Subtropical water by enhancing mixing as suggested by Lewis and Kirwan (1985) and Lewis *et al.* (1989).

6.4 Lower Layer Flow

From the ninety day model results it seems the lower layer flow may affect the upper layer flow. The lower layer cyclonic flow in the Campeche Basin persists throughout the entire simulation. When the anticyclone, M1, begins to interact with the slope the cyclonic flow briefly loses some of its coherency. Eventually, however, MC5 manifests itself in the upper layer. This is in agreement with Smith and O'Brien (1983) who demonstrated numerically that the lower layer cyclones

evolved into upper layer expressions which may become out of phase with the lower layer and move independent of topography. The actual flow of the Campeche Bay is cyclonic and has caused some concern as Sturges and Blaha (1976) and Elliot (1982) thought it was a wind-driven response. Flierl (1984) in his analytical model of a warm-core ring generated from Gulf Stream meanders suggested that the lower layer flow is a factor influencing the steering of the upper layer ring. The model results presented here suggest the lower layer flow may contribute to the dynamics of the upper layer to a greater extent than previously thought.

Hamilton (1990) presented the mean currents for the deep Gulf (below 1000 m) which are shown in Figure 30a. The mean is about 3 cm/sec towards the south at 2000 m and about 4 cm/sec at 2500 m (Station GG). These means are all comparable to the lower layer currents in the model from days 1820–1850 (Figures 15-18). During this period, the southward flow along the western isobaths intensifies and the lower layer flow regime is in a state of flux due to the merger of M1 and M2 and the concomitant creation of an eastward offshore transport process.

In Figure 30b, the velocity time series of 40-hour low-passed currents recorded at Mooring R are shown. The current structure for the entire column is roughly coherent beginning on day 280 but at day 284 the flow below 1000 m is no longer coherent with the flow in the upper 300 m. This is the same time a rebound occurred at 24.5°N 94°W in Figure 6. These data support the contention of

Smith (1986) that the topography erodes the lower layer structure and enhances the tendency for the upper layer to become out of phase from the lower. This is seen in Figure 14 of the model results as the upper layer anticyclone, M1, has a weak anticyclonic signature in the lower layer. After M1 interacts with M2, the anticyclonic flow in the lower layer flow disappears as seen in Figure 18.

During the merging event, there is a transfer of energy to the lower layer. This is shown in panel *f* of Figure 23. This figure also shows there is an approximate conservation of kinetic energy in the system consisting of M1, M2 and MC5. This may indicate a mechanism by which the Gulf assimilates some of the negative vorticity introduced by the Loop Current rings.

As the ring migrates toward the slope, the lower layer flow of the ring is weakly anticyclonic. When the ring interacts with the fossil ring along the slope, it readjusts, the anticyclonic lower layer flow disappears and the lower layer cyclonic flow intensifies and becomes expressed in the upper layer. This coherent cyclonic flow of the entire water column probably has a major effect upon the dynamics along the slope.

The question of what is the fate of a portion of these large water masses shed from the Loop Current may be answered in part by the model results of the lower layer. There is a significant flow to the northeast along the Yucatan escarpment at the 3000 *m* isobath. This may be an indication of a leakage of some of the water that flows into the Gulf back through the Yucatan Straits. As there are no direct

current measurements in this area it is plausible that this is indeed occurring in the southern Gulf of Mexico.

6.5 Fission

A large gain of angular momentum and an intensification of the lower layer flow are two likely causes for the ring fission seen in the model results. Nof (1991) found that a large gain in angular momentum would enhance fission. In the model results presented here in Figure 23c, M2 gained angular momentum prior to spawning an anticyclone. The spawning of another eddy by M2 may be due to the intensification of the lower layer cyclonic flow seen in Figure 19c. Lewis and Kirwan (1985) demonstrated that the anticyclones may persist at least 3–5 months off of the Mexican coast suggesting fission products.

7. Conclusions

Based upon the results presented here, several conclusions may be made:

- The "peanut-shaped" orbits found in many of the drifter tracks result from the merging of an anticyclonic Loop Current ring with a fossil ring along the slope.
- During a merging event the two rings exchange mass.
- This merger is the cause of a large offshore transport.
- This merger results in a cyclonic flow structure developing to the north.
- Some of the ring energy is transferred into the lower layer.
- The fossil ring is renewed as it receives some energy from the Loop Current ring.
- The lower layer flow may be responsible for the appearance of the many observed cyclones.

Thus, there are several questions answered by this research. When a ring migrates into the western Gulf of Mexico it may merge partially with a fossil ring and exchange mass. The ring may transfer energy into the lower layer. During this interaction a cyclone is generated. As Figure 16 suggests, the "peanut-shaped" orbits are evidence of a merger of two rings. As this pattern is seen in many of the

drifter tracks, this type of ring/ring interaction is a common feature in the Gulf. As an exchange of mass is observed in the model merger, it seems likely that an exchange of mass is occurring along the western slope of the Gulf of Mexico. This merger also explains the two mesoscale features: a short-lived offshore transport which is directed toward the east and a northern cyclonic flow structure. Part of the development of the cyclone is attributed to the offshore transport of 30 Sverdrups seen in both the model and observations. The cyclone is not stationary but migrates to the north in tandem with the anticyclone.

The prevailing thought is that all Loop Current rings interact with the western slope of the Gulf of Mexico. The results of this research imply that this may not be the case. Some rings may interact with a fossil ring that is stationary along the slope and re-energize the fossil ring. In addition, the model results account for the ephemeral nature of the cyclones for they are associated with the anticyclones and do not remain stationary.

Several other questions are raised by this research. What mechanism is responsible for the transfer of energy to the lower layer? How much of an effect does the lower layer flow have on the dynamics along the slope? Do the cyclones play a major role in mixing processes and the formation of Gulf Common water? Hopefully future research will address these questions.

A unique aspect of this research is the ability to follow the evolution of a specific mesoscale feature, namely, a model ring that is interacting with other

flow structures and is encountering realistic topography. By following the evolution of integral quantities in an eddy-resolving general circulation model and by comparing model results with observations, this study has shed more light on the interaction of a Loop Current ring with another fossil ring along the western slope of the Gulf of Mexico. Success in the comparison of models with observations may lead to the isolation of the important dynamical factors of the system which is not possible with observations. In addition, the application of quantitative techniques to compare the model results with observed data, specifically, hydrography, Lagrangian kinematics and current meter data should prove useful for similar studies in other geographic regions.

References

Austin, R. M., Jr., 1955. Some recent oceanographic surveys of the Gulf of Mexico. *Trans. Amer. Geophys. Union*, **35**: 885–892.

Blaha, J. R. and W. Sturges, 1978. Evidence for wind forced circulation in the Gulf of Mexico, technical report, Dept. of Oceanogr., Fla. State. Univ., Tallahassee.

Brooks, D. A., 1984. Current and hydrographic variability in the northwestern Gulf of Mexico. *J. Geophys. Res.*, **89**: 8022–8032.

Brooks, D. A. and R. Legeckis, 1982. A ship and satellite view of hydrographic features in the western Gulf of Mexico. *J. Geophys. Res.*, **87**: 4195–4206.

Buzbee, B. L., F. W. Dorr, J. A. George and G. H. Golub, 1971. The discrete solution of the discrete Poisson equation on irregular regions. *SIAM J. Numer. Anal.*, **8**: 722–736.

Cochrane, J. D. and F. J. Kelly, 1986. Low-frequency circulation on the Texas-Louisiana continental shelf. *J. Geophys. Res.*, **91**: 10,645–10,659.

Cresswell, G. R., 1982. The coalescence of two East Australian Current warm-core eddies. *Science*, **215**: 161–164.

Cresswell, G. R. and R. Legeckis, 1987. Eddies off southeastern Australia, 1980/81. *Deep-Sea Res.*, **34**: 1527–1562.

Cooper, C., G. Z. Forristall and T. M. Joyce, 1990. Velocity and hydrographic

structure of two Gulf of Mexico warm-core rings. *J. Geophys. Res.*, **95**: 1663–1679.

Cox, M. O., 1979. A numerical model of Somali Current eddies. *J. Phys. Ocean.*, **9**: 311–326.

Cushman-Roisin, B., 1989. On the role of filamentation in the merging of anticyclonic lenses. *J. Phys. Ocean.*, **19**: 253–258.

Deem, G. S. and N. J. Zabusky, 1978. Vortex waves: stationary "*V* states," interactions, recurrence, and breaking. *Phys. Rev. Letters*, **40**: 859–862.

DeVorsey, L., Jr., 1980. William DeBrahm's "continuation of the Atlantic Pilot," An empirically supported eighteenth century model of North Atlantic circulation, in *Oceanography: The Past*, edited by M. Sears and D. Merriman, 812 pp., Springer-Verlag, New York.

Dinnel, S. P. and W. J. Wiseman, Jr., 1986. Fresh water on the Louisiana and Texas shelf. *Cont. Shelf Res*, **6**: 765–784.

Doblar, R. A. and R. E. Cheney, 1977. Observed formation of a Gulf Stream cold core ring. *J. Phys. Ocean.*, **7**: 944–994.

Elliot, B. A., 1979. Anticyclonic rings and the energetics of the circulation of the Gulf of Mexico, Ph.D. Dissertation, Department of Oceanography, Texas A&M Univ., College Station, Texas.

Elliot, B. A., 1982. Anticyclonic rings in the Gulf of Mexico. *J. Phys. Ocean.*, **12**: 1293–1309.

Flierl, G. R., 1984. Rossby wave radiation from a strongly nonlinear warm eddy. *J. Phys. Ocean.*, **14**: 47–58.

Hamilton, P., 1990. Deep Currents in the Gulf of Mexico. *J. Phys. Ocean.*, **20**: 1087–1104.

Hockney, R. W., 1965. A fast direct solution of Poisson's equation using Fourier analysis. *J. of the Assoc. for Computing Machinery*, **12**: 95–113.

Hofmann, E. E. and S. J. Worley, 1986. An investigation of the circulation of the Gulf of Mexico. *J. Geophys. Res.*, **91**: 14,221–14,236.

Hooker, S., 1987. Mesoscale eddy dynamics by the method of point vortices, Ph.D. Dissertation, Univ. of Miami, Miami, FL.

Hurlburt, H. E., and J. D. Thompson, 1980. A numerical study of Loop Current intrusions and eddy shedding. *J. Phys. Ocean.*, **10**: 1611–1651.

Hurlburt, H. E., and J. D. Thompson, 1982. The dynamics of the Loop Current and shed eddies in a numerical model of the Gulf of Mexico, in *Hydrodynamics of Semienclosed Seas*, edited by J. C. J. Nihoul, 243–297 pp., Elsevier Scientific Publishing Company, Amsterdam.

Ichiye, T., 1962. Circulation and water mass distribution in the Gulf of Mexico. *Geofis. Int.*, **2**: 47–76.

Indest, A. W., A. D. Kirwan, Jr., J. K. Lewis, and P. Reinersman, 1989. A synopsis of mesoscale eddies in the Gulf of Mexico, in *Mesoscale/Synoptic Coherent Structures in Geophysical Turbulence*, edited by Nihoul, J. C. J and B. M. Jamart, 485–500 pp., Elsevier Science Publishers, B. V. Amsterdam.

Kirwan, A. D., Jr., A. W. Indest, J. Liu, and N. Clark, 1990. Ring evolution in general circulation models from path analysis, J. Geophys. Res.. 95 18,057–18,073

Kirwan, A. D., Jr., J. K. Lewis, A. W. Indest, P. Reinersman, and I. Quintero, 1988. Observed and simulated kinematic properties of Loop Current rings. *J. Geophys. Res.*, **93**: 1189–1198.

Kirwan, A. D., Jr., W. J. Merrell, Jr., J. K. Lewis, R. E. Whitaker, and R. Legeckis, 1984a. A model for the analysis of drifter data with an application to a warm core ring in the Gulf of Mexico. *J. Geophys. Res.*, **89**: 3425–3428.

Kirwan, A. D., Jr., W. J. Merrell, Jr., J. K. Lewis, and R. E. Whitaker, 1984b. Lagrangian observations of an anticyclonic ring in the western Gulf of Mexico. *J. Geophys. Res.*, **89**: 3417–3424.

Lai, D. Y. and P. L. Richardson, 1977. Distribution and movement of Gulf Stream rings. *J. Phys. Ocean.*, **7**: 670–683.

Leben, R. R., G. H. Born, J. D. Thompson and C. A. Fox, 1990. Mean sea surface and variability of the Gulf of Mexico using Geosat altimetry data. *J. Geophys. Res.*, **95**: 3025–3032.

Lewis, J. K., and A. D. Kirwan, Jr., 1985. Some observations of ring topography and ring-ring interactions in the Gulf of Mexico. *J. Geophys. Res.*, **90**: 9017–9028.

Lewis, J. K., and A. D. Kirwan, Jr., 1987. Genesis of a Gulf of Mexico ring as determined from kinematic analyses. *J. Geophys. Res.*, **92**: 11,727–11,740.

Lewis, J. K., A. D. Kirwan, Jr., G. Z. Forristall, 1989. Evolution of a warm-core ring in the Gulf of Mexico: Lagrangian observations. *J. Geophys. Res.*, **94**: 8163–8178.

McCreary, J. and P. Kundu, 1987. A numerical investigation of Somali Current during the Southwest Monsoon. *J. Mar. Res.*, **46**: 25–58.

Meid, R. P. and G. J. Lindemann, 1979. The propagation and evolution of cyclonic Gulf Stream rings. *J. Phys. Ocean.*, **9**: 1183–1206.

Meid, R. P. and G. J. Lindemann, 1984. Mass transfer between Gulf Stream Rings. *J. Geophys. Res*, **89**: 6365–6372.

Merrell, W. J., and J. M. Morrison, 1981. On the circulation of the western Gulf of Mexico with observations from April 1978. *J. Geophys. Res*, **86**: 4181–4185.

Merrell, W. J., and A. M. Vasquez, 1983. Observations of changing mesoscale circulation patterns in the western Gulf of Mexico. *J. Geophys. Res.*, **88**: 7721–7723.

Müller-Karger, F. E., J. J. Walsh, R. H. Evans and M. B. Myers, 1991. The seasonal phytoplankton concentration and sea surface temperature cycles of the Gulf of Mexico as determined by satellites. *J. Geophys. Res.*, **96**: 12,645–12,665.

Nakamoto, S., 1986. Application of soliton wave theory to mesoscale eddies in the Gulf of Mexico, Ph.D. Dissertation, Dept. of Oceanography, Texas A&M University, College Station, Texas.

Nakamoto, S., 1989. Solitonlike solutions in Loop Current Eddies. *J. Geophys. Res.*, **94**: 14,567–14,574.

Nof, D., 1988. The fusion of isolated nonlinear eddies. *J. Phys. Ocean.*, **18**: 887–905.

Nof, D., 1991. Fission of single and multiple eddies. *J. Phys. Ocean.*, **21**: 40–52.

Nowlin, W. D., Jr. and H. J. McLellan, 1967. A characterization of the Gulf of Mexico waters in winter. *J. Mar. Res.*, **25**: 29–59.

Nowlin, W. D., Jr., J. M. Hubertz and R. O. Reid, 1968. A detached eddy in the Gulf of Mexico. *J. Mar. Res.*, **26**: 185–186.

Nowlin, W. D., Jr., 1972. Winter circulation patterns and property distributions, in *Contributions on the Physical Oceanography of the Gulf of Mexico, Tex. A&M Univ. Oceangr. Stud.,vol.2*, edited by Capurro, L. R. A. and J. L. Reid, 3–53 pp., Gulf, Houston, TX.

Nowlin, W. D., Jr. and J. M. Hubertz, 1972. Contrasting summer circulation patterns for the eastern gulf, in *Contributions on the Physical Oceanography of the Gulf of Mexico, Tex. A&M Univ. Oceangr. Stud.,vol.2*, edited by Capurro, L. R. A. and J. L. Reid, 119–137 pp., Gulf, Houston, TX.

Okubo, A., 1970. Horizontal disperson of floatable particles in the vicinity of velocity singularities such as convergences. *Deep-Sea Res.*, **17**: 445–454.

Orlanski, I., 1976. A simple boundary condition for unbounded hyperbolic flows. *J. Comp. Phys.*, **21**: 251–269.

Press, W. H., Flannery, B. P, Terikesky, S. A, Vetterlin, W. T., 1988. *Numerical Recipes in C, The Art of Scientific Computing*, Cambridge University Press, Cambridge, 735 pp.

Schott, F. A., T. N. Lee and R. Zantopp, 1988. Variability of structure and transport of the Florida Current in the period of days to seasonal. *J. Phys. Ocean.*, **18**: 1209–1230.

Science Applications International Corporation, 1988. Gulf of Mexico physical oceanography program, final report: year 3 Volume II: technical report, Mineral Management Service Contract No. 14-12-0001-29158, OCS Report/MMS 88-0046, 241pp.

Smith, D. C., IV, 1986. A numerical study of Loop Current eddy interaction with topography in the western Gulf of Mexico. *J. Phys. Ocean.*, **16**: 1260–1272.

Smith, D. C., IV and J. J. O'Brien, 1983. The interaction of a two-layer isolated mesoscale eddy with bottom topography. *J. Phys. Ocean.*, **13**: 1681–1697.

Stern, M. E., 1987. Horizontal entrainment and detrainment in large-scale eddies. *J. Phys. Ocean.*, **17**: 1688–1695.

Sturges, W. and J. R. Blaha, 1976. A western boundary current in the Gulf of Mexico. *Science*, **192**: 367–369.

Sweitzer, N. B., Jr., 1898. Origin of the Gulf Stream and circulation of waters in the Gulf of Mexico with special reference to the effect on jetty construction. *Trans. Am. Soc. Civ. Eng.*, 40: 86–98.

Vukovich, F. M., and B. W. Crissman, 1986. Aspects of warm rings in the Gulf of Mexico. *J. Geophys. Res.*, **91**: 2645–2660.

Vukovich, F. M., and G. A. Maul, 1985. Cyclonic eddies in the eastern Gulf of Mexico. *J. Phys. Ocean.*, **15**: 105–117.

Vukovich, F. M., and E. Waddell, 1991. Interaction of a warm ring with the western slope in the Gulf of Mexico. *J. Phys. Ocean.*, **21**: 1062–1074.

Wallcraft, A. J., 1985. Gulf of Mexico circulation modeling study, Annual Progress Report, Year 1, report to Mineral Management Service, 9411, JAYCOR, Vienna, Virginia.

Wallcraft, A. J., 1986. Gulf of Mexico circulation modeling study, Annual Progress Report, Year 2, report to Mineral Management Service, 9411, JAYCOR, Vienna, Virginia.

Walsh, J. J., D. A. Dieterle, M. B. Myers and F. E. Müller-Karger, 1989. Nitrogen exchange at the continental margin: A numerical study of the Gulf of Mexico. *Prog. Oceanogr.*, **23**: 248–301.

Wert, R. T. and R. O. Reid, 1972. A baroclinic prognostic numerical circulation model, in *Contributions on the Physical Oceanography of the Gulf of Mexico, Tex. A&M Univ. Oceangr. Stud.,vol.2*, edited by Capurro, L. R. A. and J. L. Reid, 177–209 pp., Gulf, Houston, TX.

Wilson, R. J., 1967. Amount and distribution of water masses in February and March, 1962, in the Gulf of Mexico, M. S. Thesis, Department of Oceanography, Texas A&M Univ., College Station, Texas.

Figure 1. (a) Cruise tracks for XBT data collected during May 26-31, 1985. The arrows denote the flow at the edges of the Loop Current (maximum horizontal temperature gradient) based on the vertical temperature structure shown in (b) temperature data from the Stena Hispania cruise, May 27-28, 1985 (from Lewis and Kirwan, 1987)

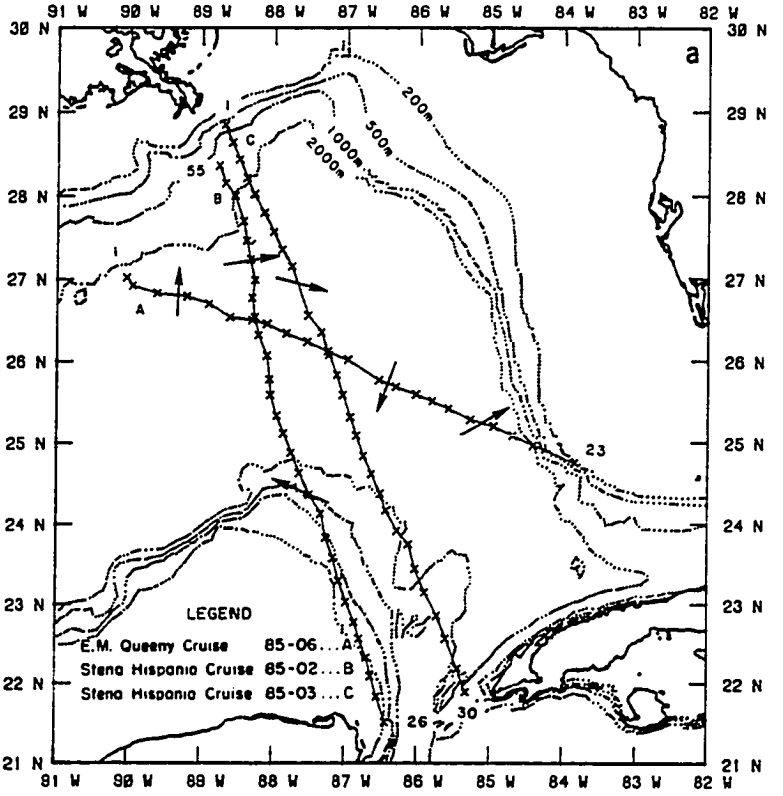

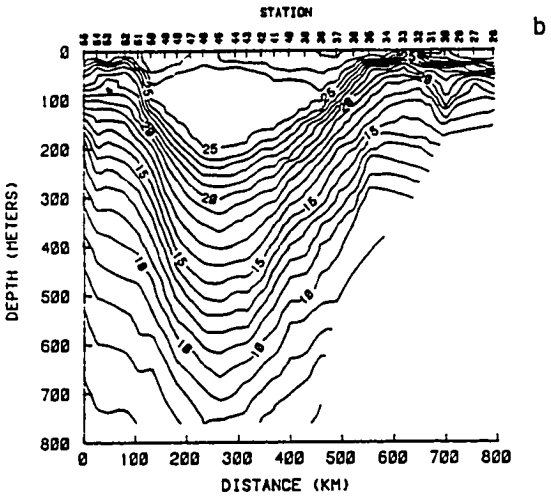

Figure 2a. Path trajectory and center track of drifter 1599. The solid line is the actual path of the drifter low-pass filtered at 100 hours and the dashed line is the center track as calculated from a kinematic analysis. Arrows denote 10 day intervals. The solid dot and X mark the start and end, respectively. The red outline encloses a peanut-shaped path.

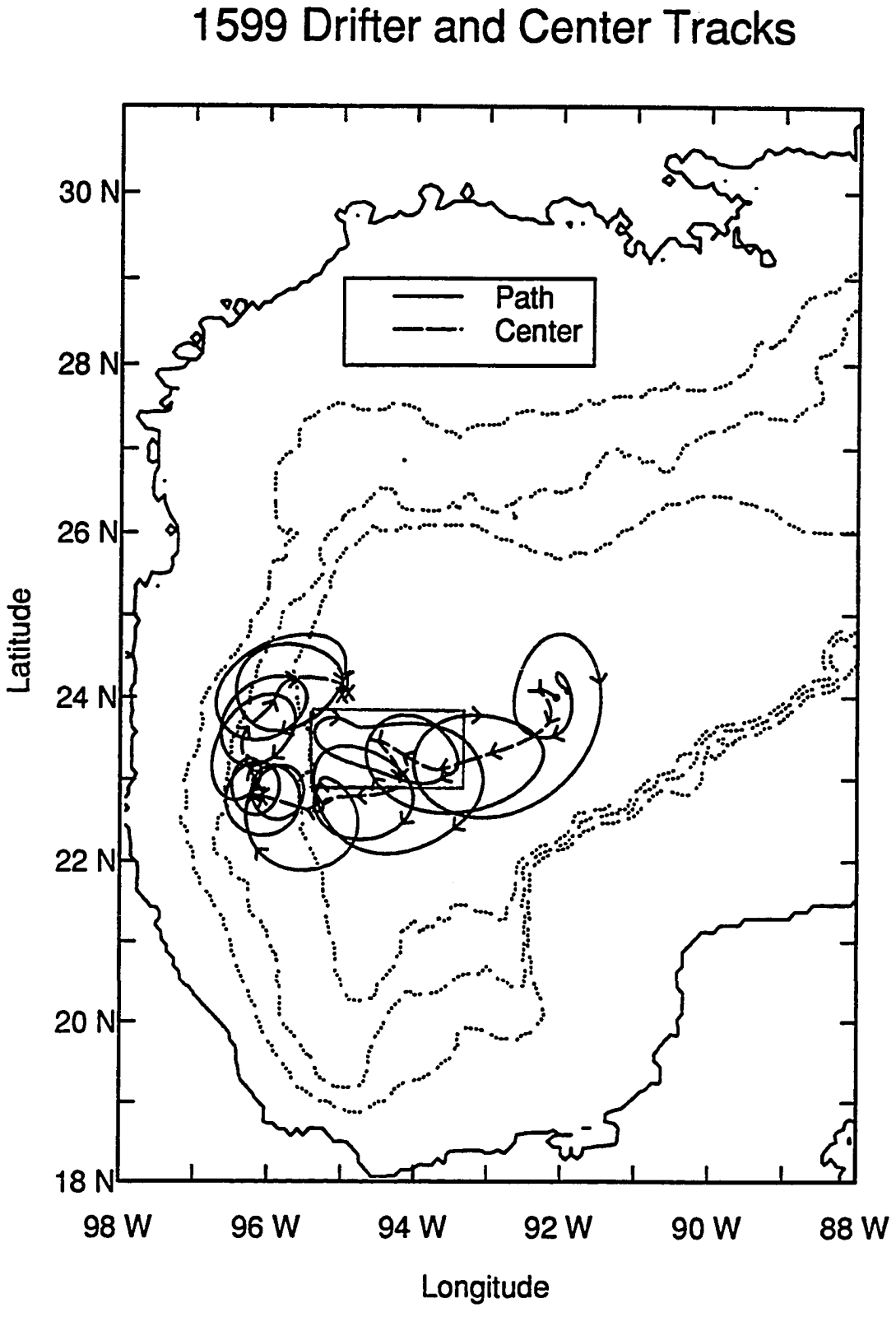

Figure 2b. Kinematic properties of Drifter 1599. a) Normal deformation. b) Shear deformation. c) Vorticity.

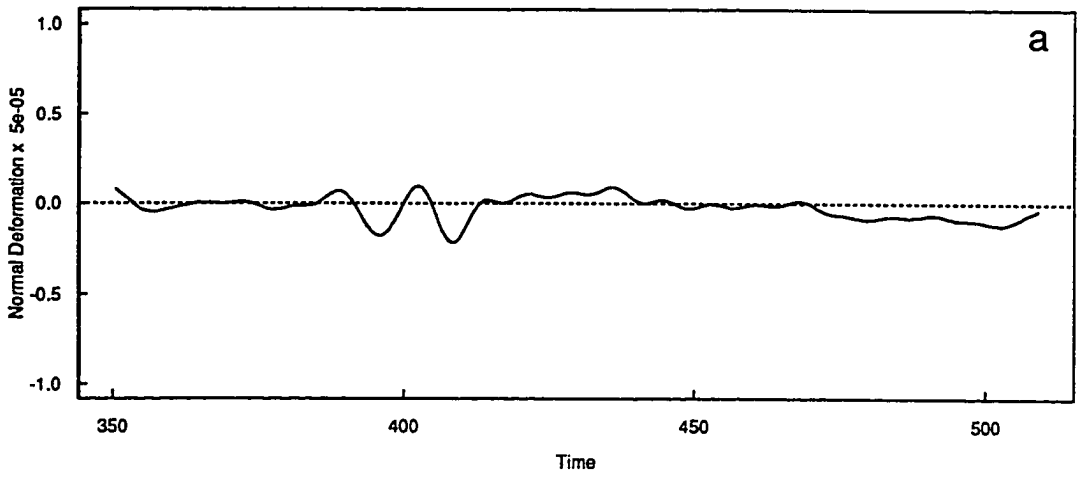

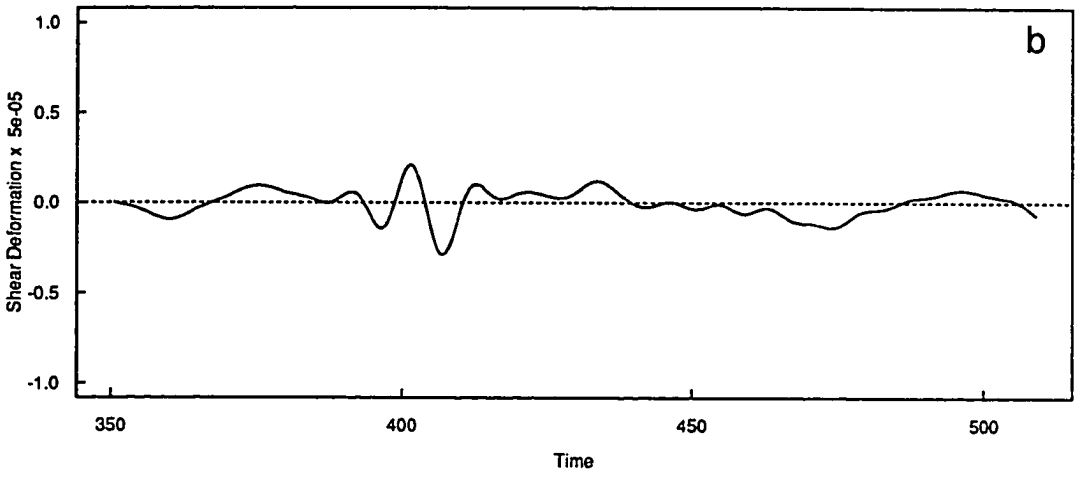

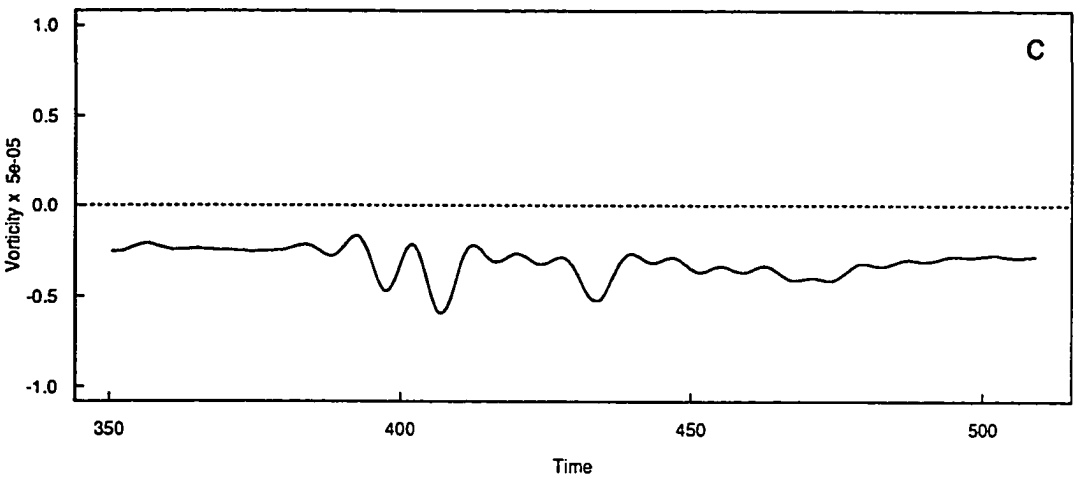

Figure 3a. Path trajectory and center track of drifter 3374. The solid line is the actual path of the drifter low-pass filtered at 100 hours and the dashed line is the center track as calculated from a kinematic analysis. Arrows denote 10 day intervals. The red outline encloses a peanut-shaped path. The solid dot and X mark the start and end, respectively.

3374 Drifter and Center Tracks

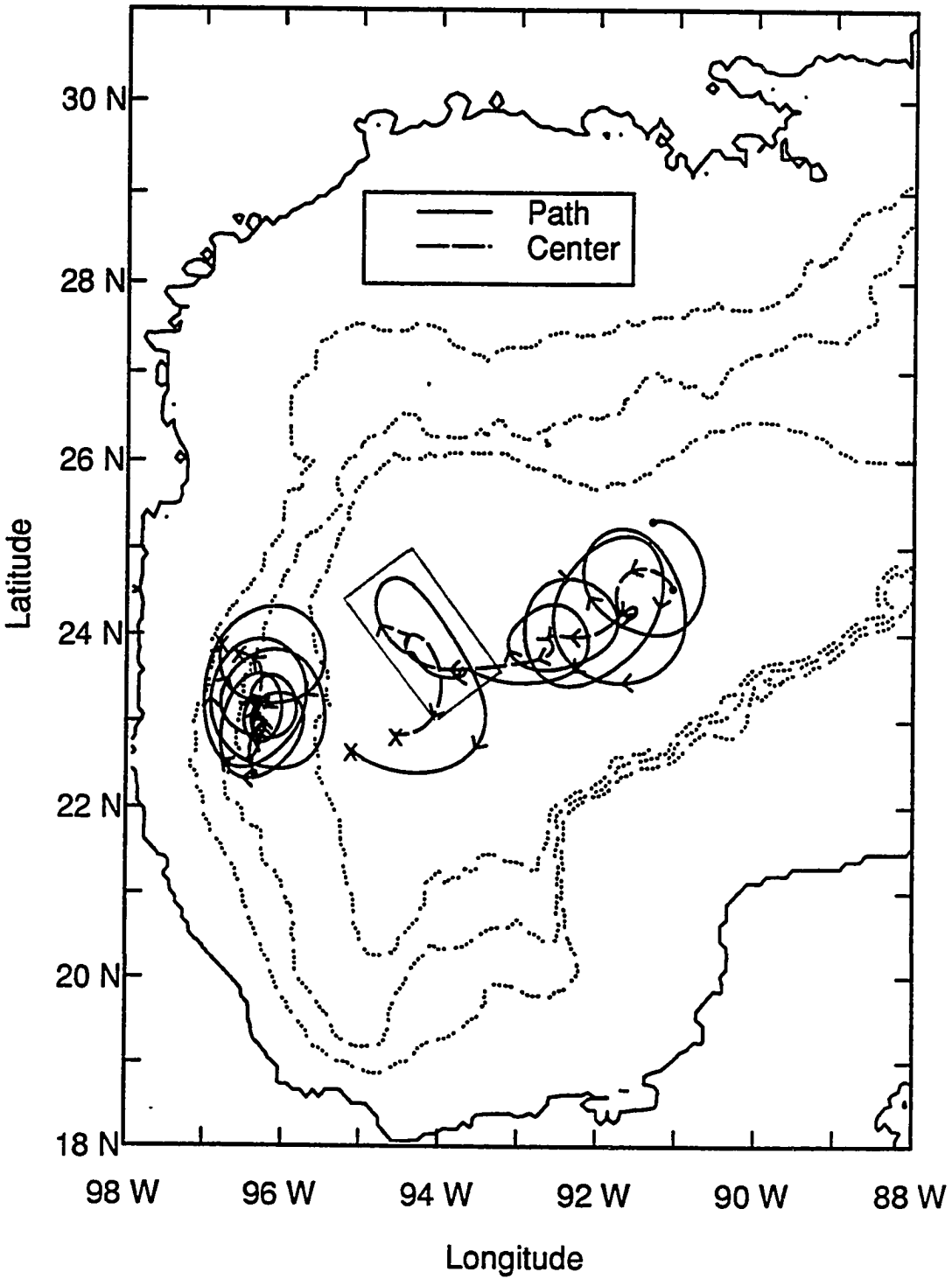

Figure 3b. Kinematic properties of Drifter 3374. a) Normal deformation. b) Shear deformation. c) Vorticity.

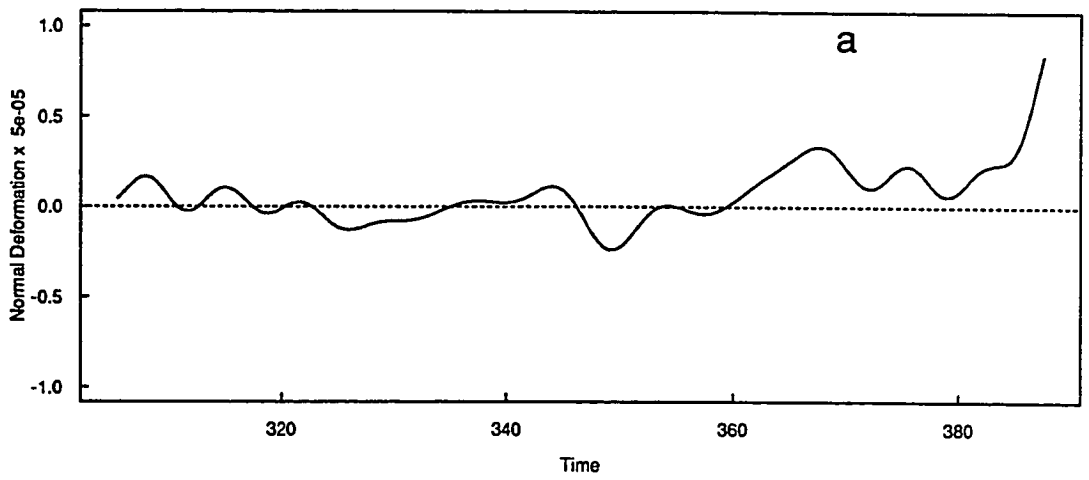

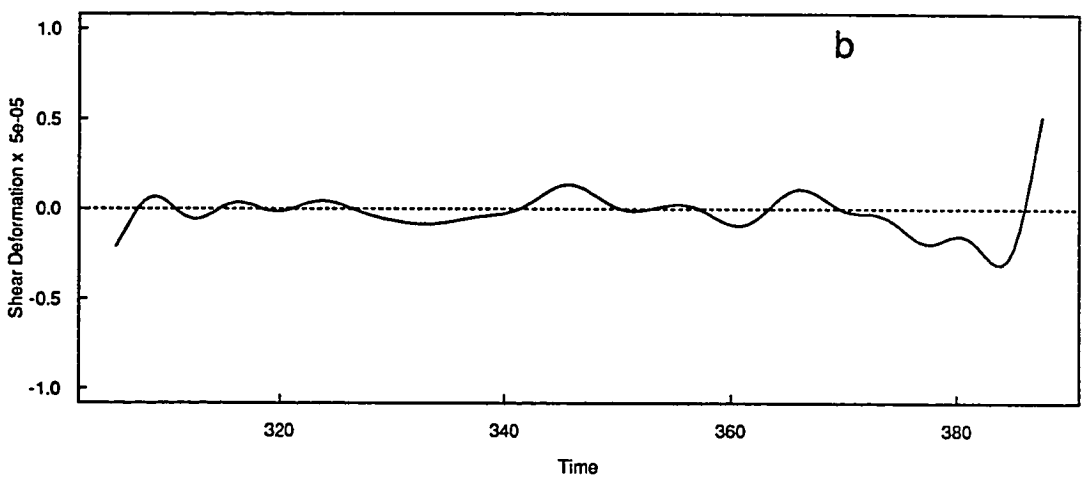

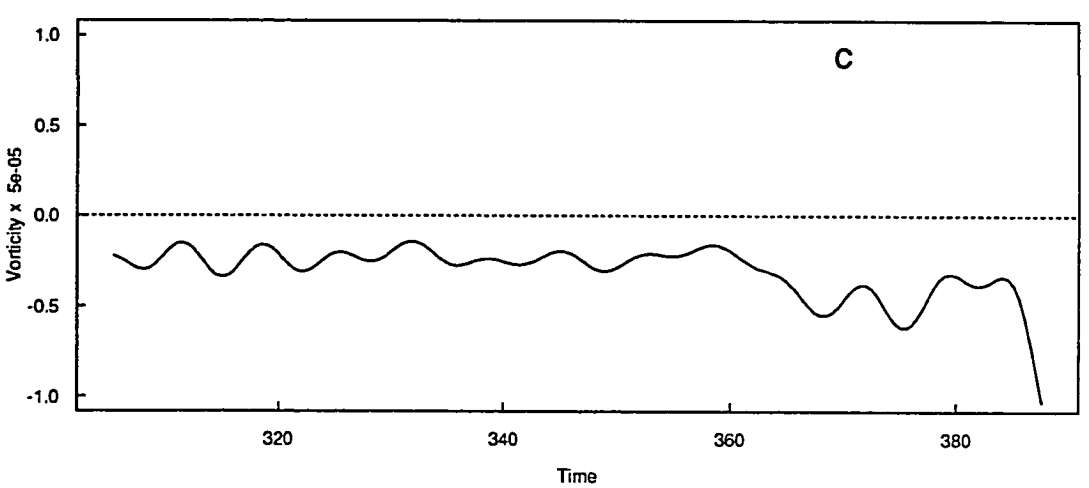

Figure 4. Path trajectory and center track of drifter 3375. The solid line is the actual path of the drifter low-pass filtered at 100 hours and the dashed line is the center track as calculated from a kinematic analysis. Arrows denote 10 day intervals. The solid dot and X mark the start and end, respectively.

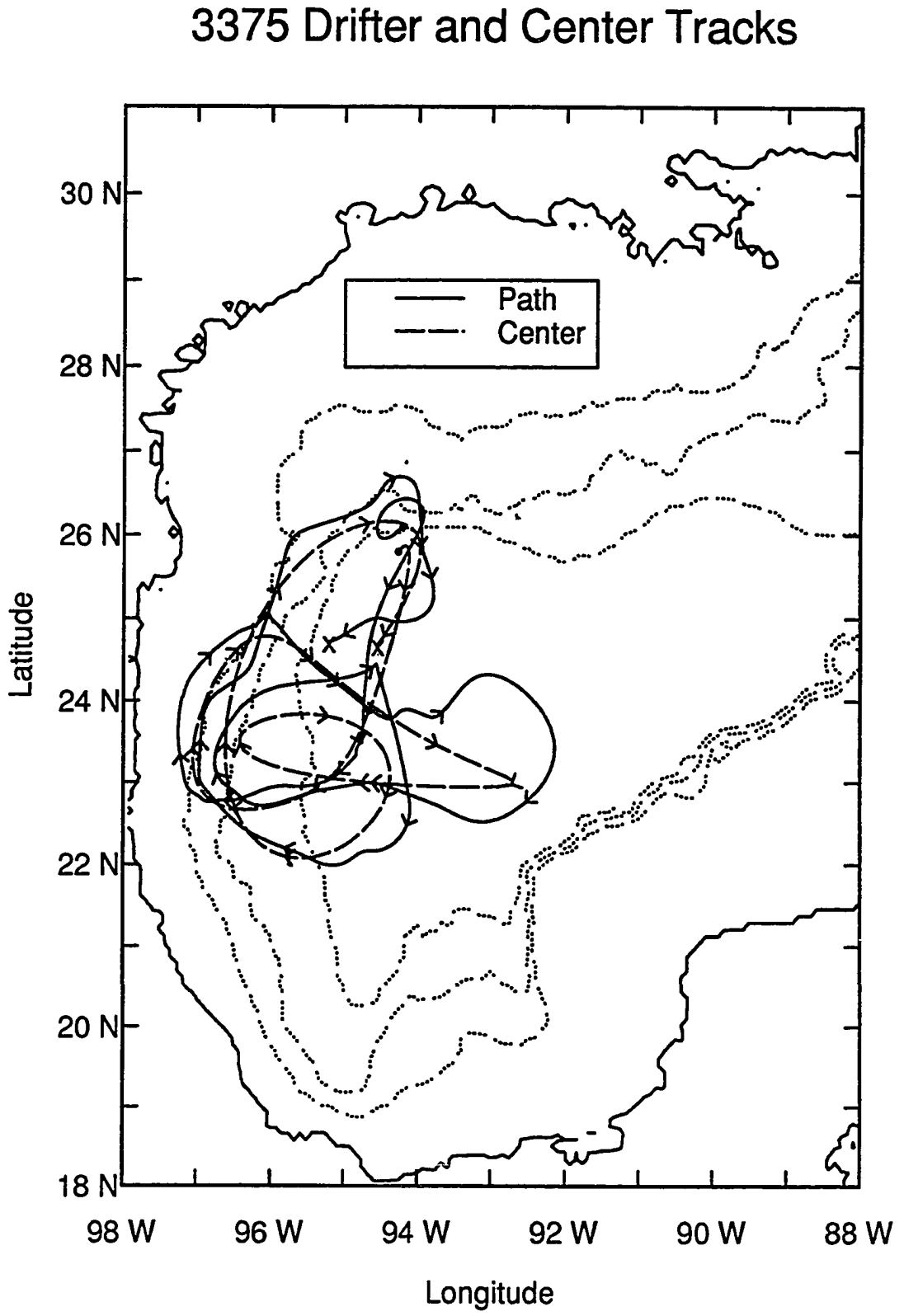

Figure 5. Path trajectory and center track of drifter 5495. The solid line is the actual path of the drifter low-pass filtered at 100 hours and the dashed line is the center track as calculated from a kinematic analysis. Arrows denote 10 day intervals. The solid dot and X mark the start and end, respectively.

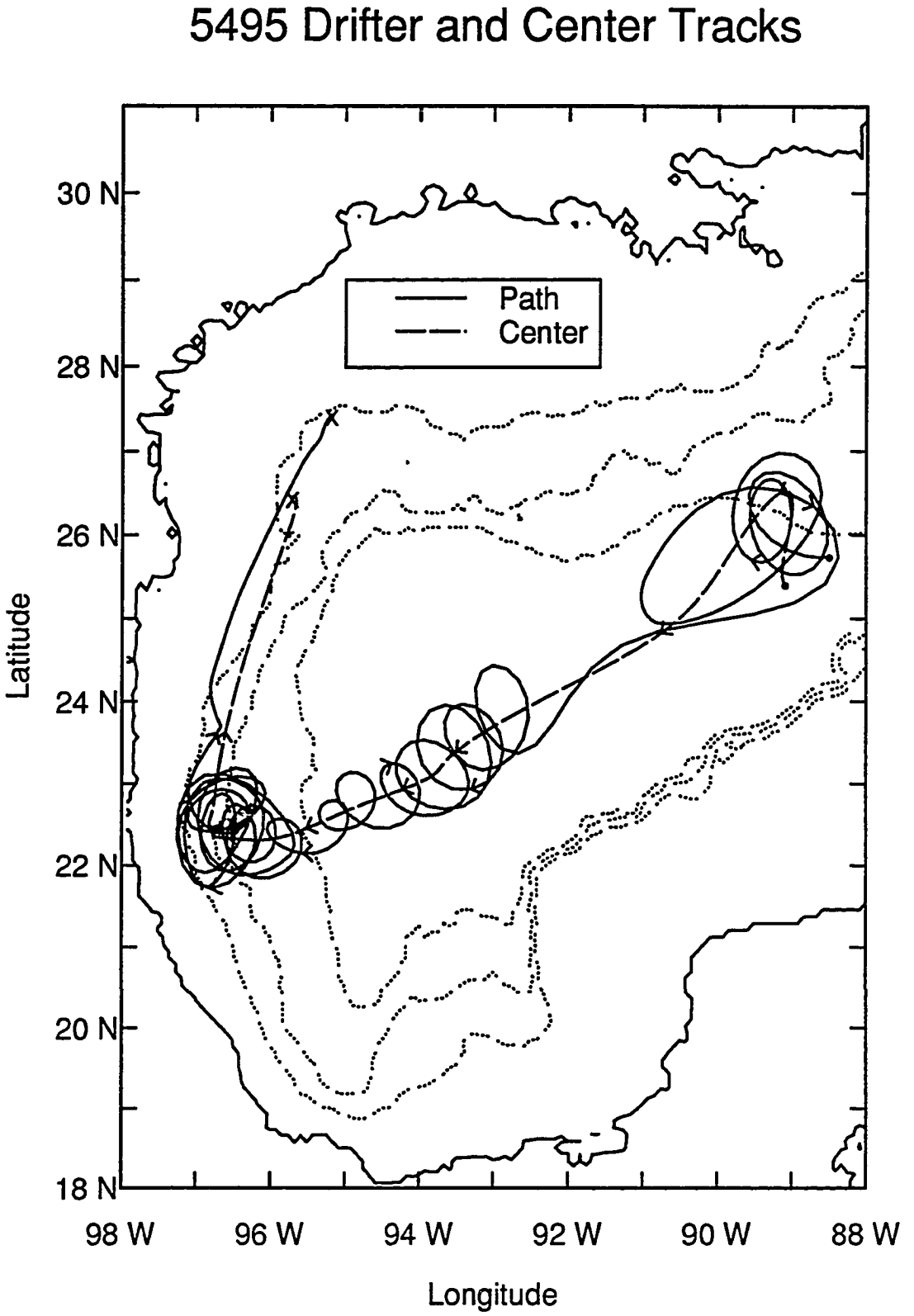

Figure 6a. Path trajectory and center track of drifter 3378. The solid line is the actual path of the drifter low-pass filtered at 100 hours and the dashed line is the center track as calculated from a kinematic analysis. Arrows denote 10 day intervals. The red outline encloses a peanut-shaped path. The solid dot and X mark the start and end, respectively.

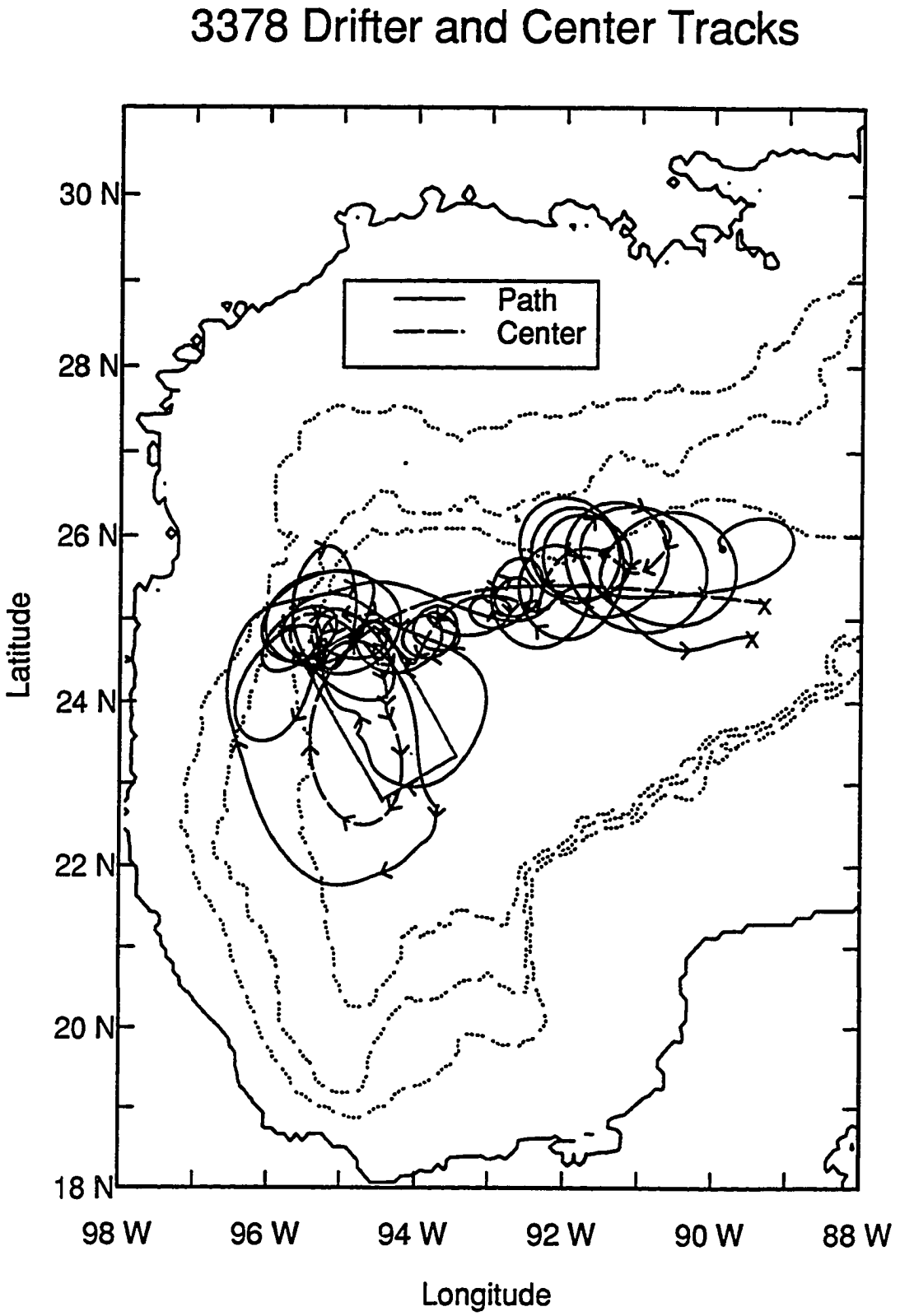

Figure 6b. Kinematic properties of Drifter 3378. a) Normal deformation. b) Shear deformation. c) Vorticity.

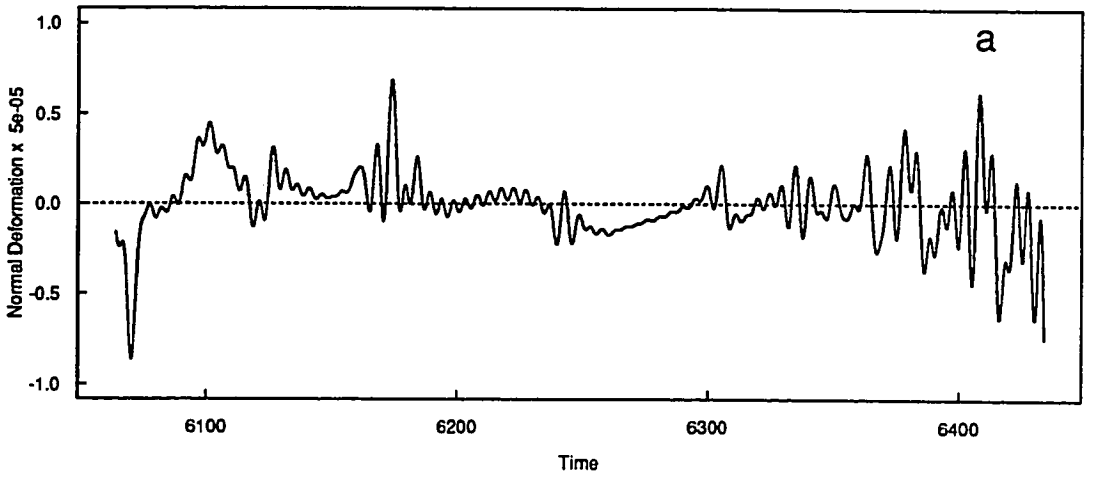

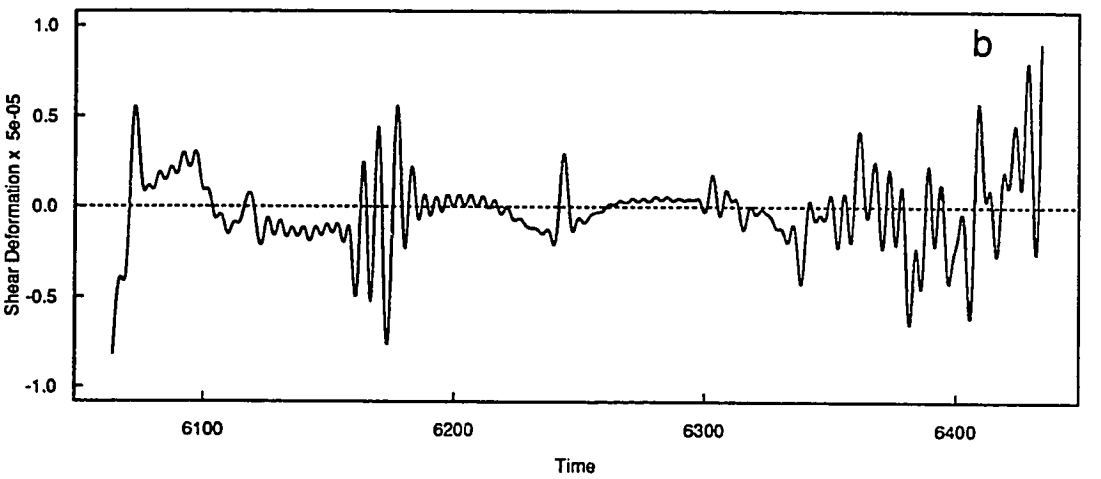

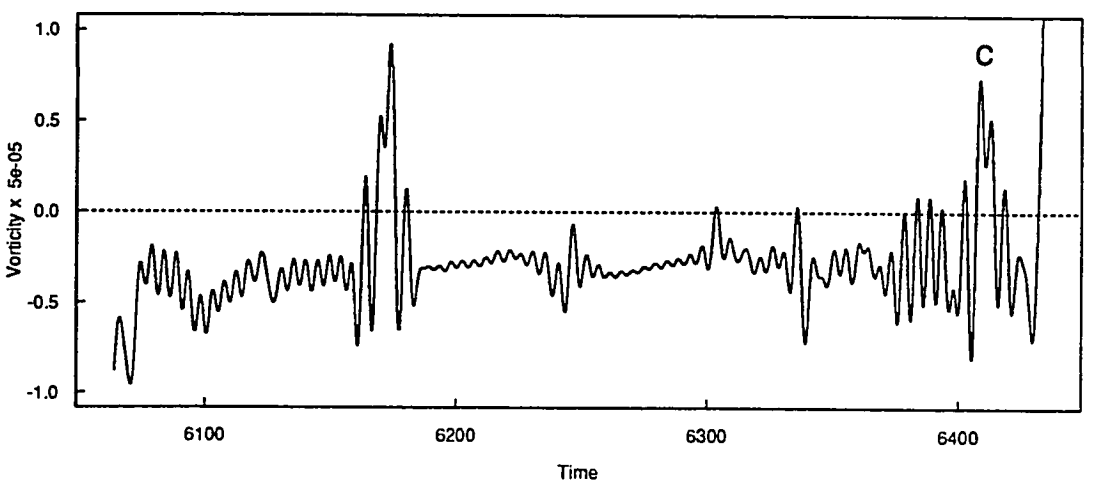

Figure 7a. Path trajectory and center track of drifter 3353. The solid line is the actual path of the drifter low-pass filtered at 100 hours and the dashed line is the center track as calculated from a kinematic analysis. Arrows denote 10 day intervals. The solid dot and X mark the start and end, respectively.

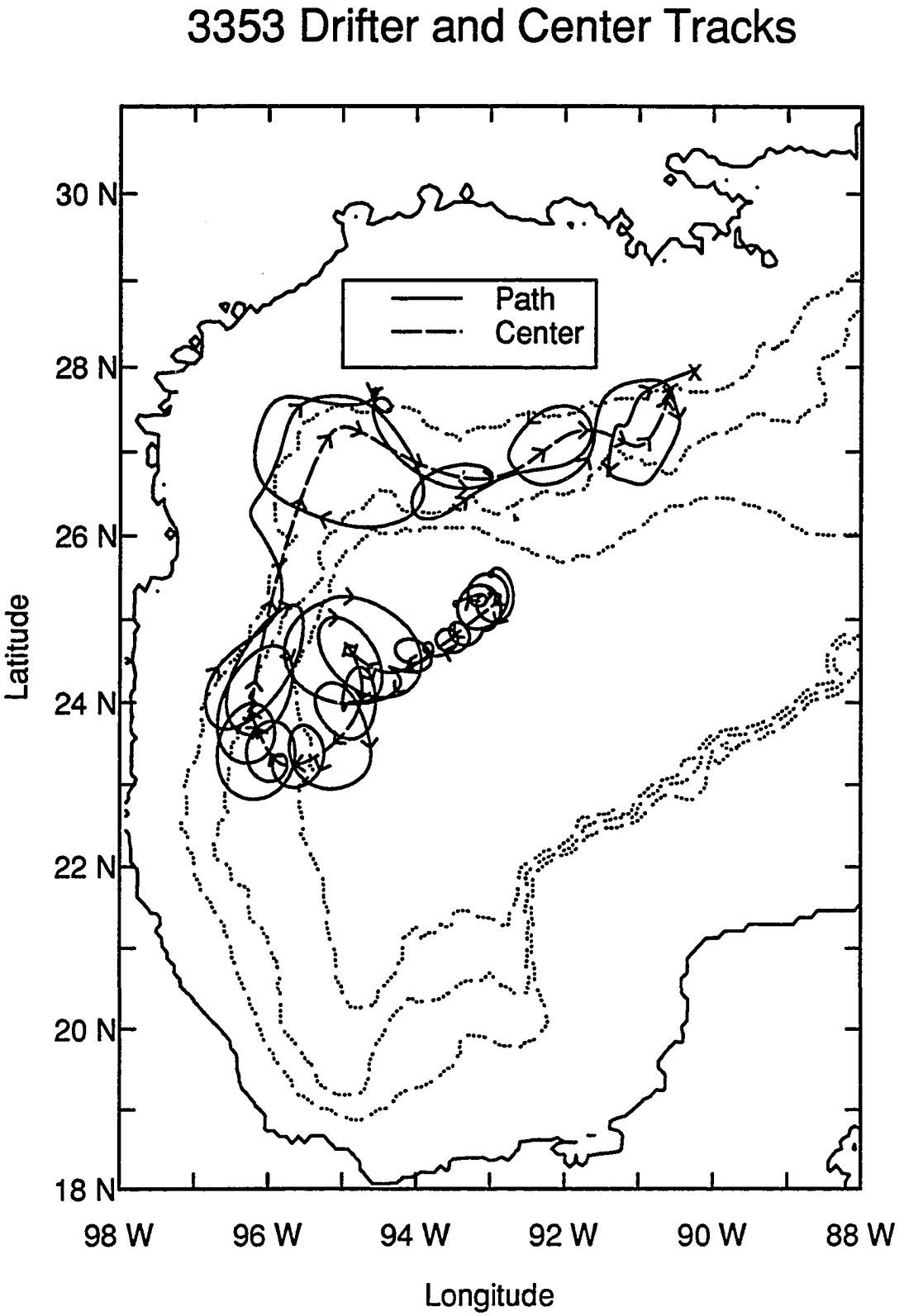

Figure 7b. Kinematic properties of Drifter 3553. a) Normal deformation. b) Shear deformation. c) Vorticity.

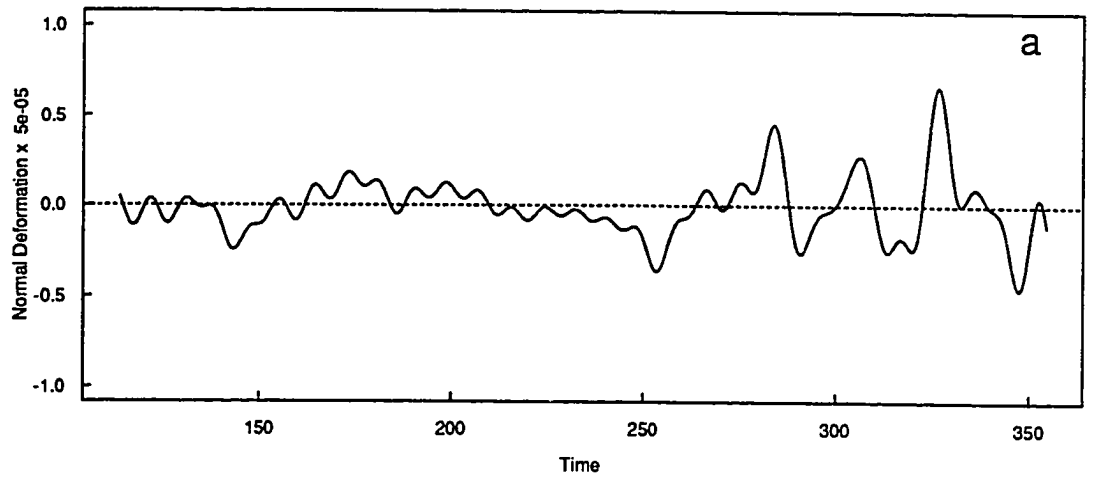

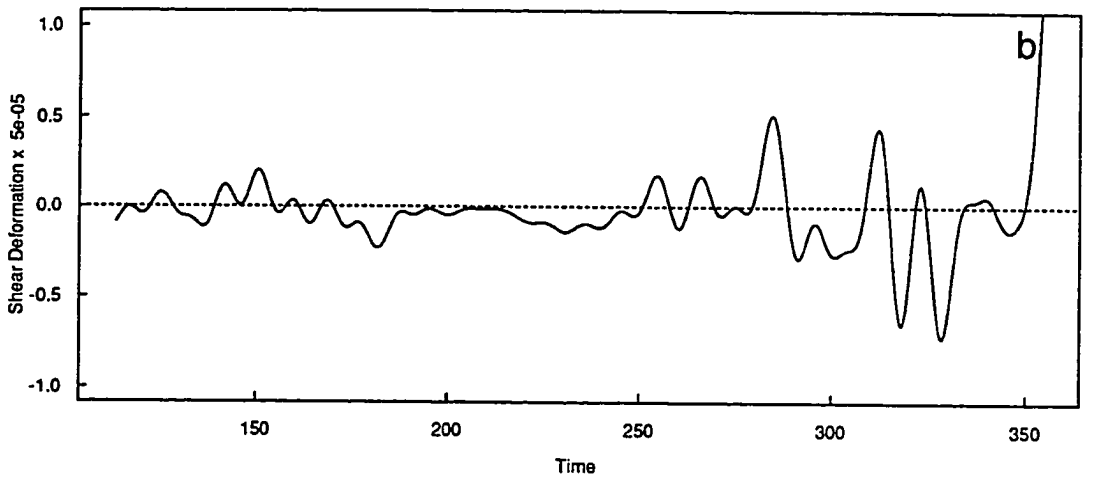

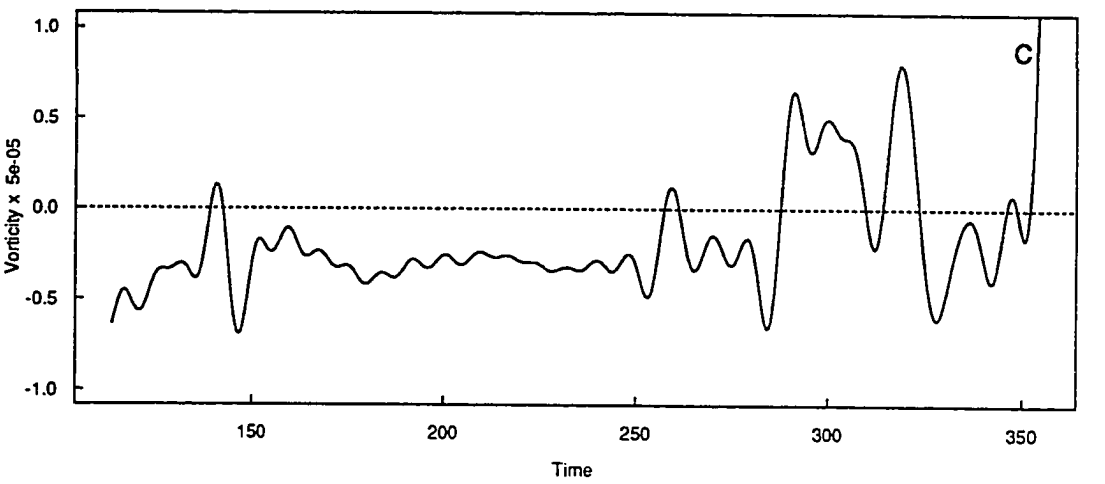

Figure 8a. Path trajectory and center track of drifter 3379. The solid line is the actual path of the drifter low-pass filtered at 100 hours and the dashed line is the center track as calculated from a kinematic analysis. Arrows denote 10 day intervals. The red outline encloses a peanut-shaped path. The solid dot and X mark the start and end, respectively.

3379 Drifter and Center Tracks

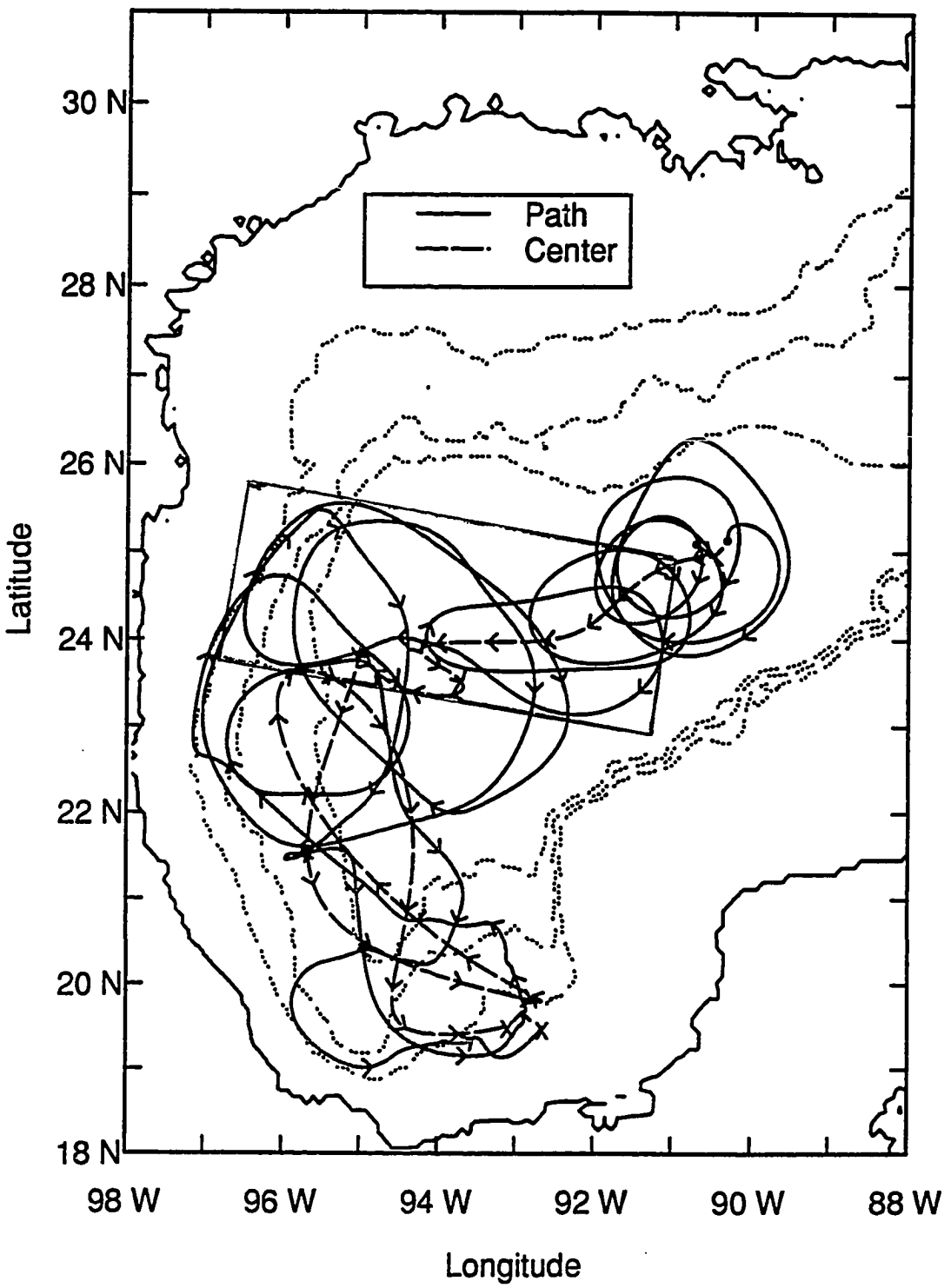

Figure 8b. Kinematic properties of Drifter 3379. a) Normal deformation. b) Shear deformation. c) Vorticity.

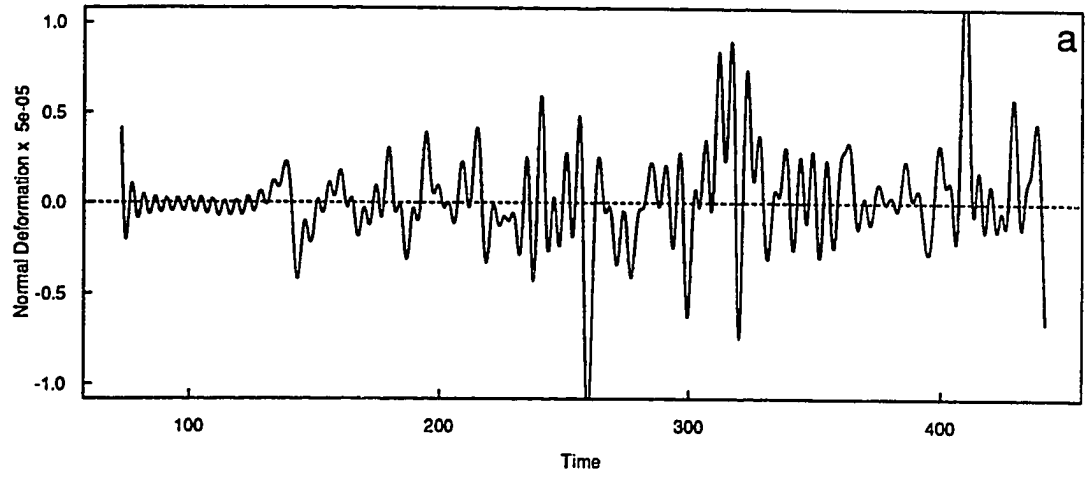

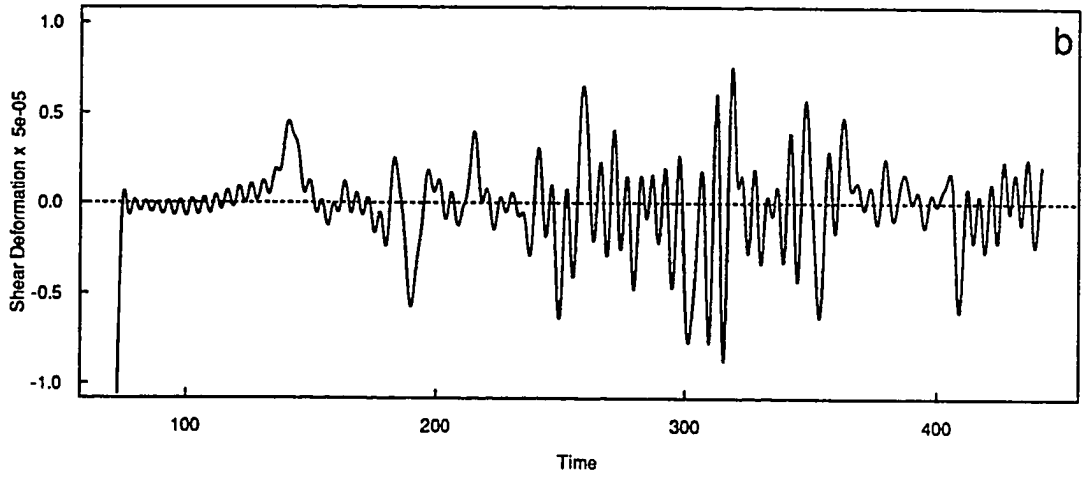

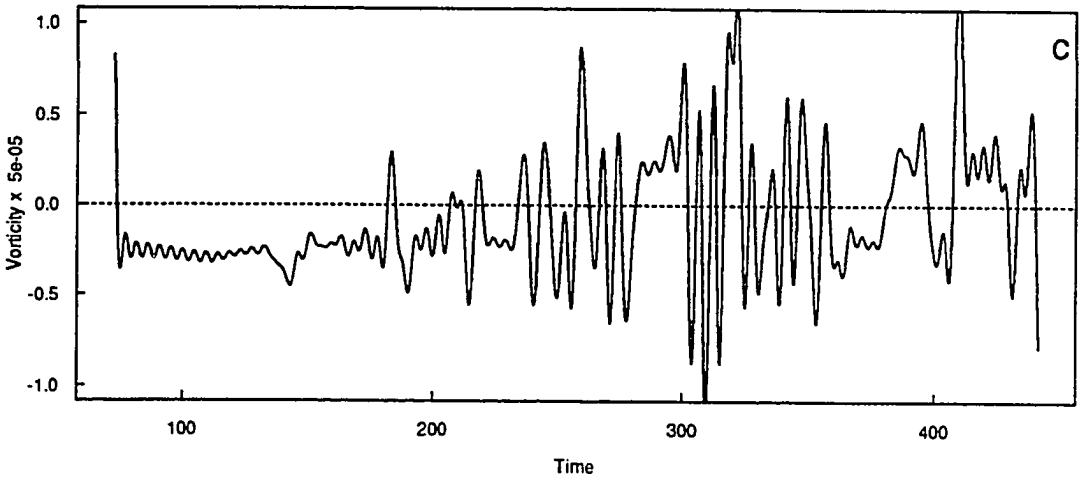

Figure 9. Path trajectory and center track of drifter 3345. The solid line is the actual path of the drifter low-pass filtered at 100 hours and the dashed line is the center track as calculated from a kinematic analysis. Arrows denote 10 day intervals. The solid dot and X mark the start and end, respectively.

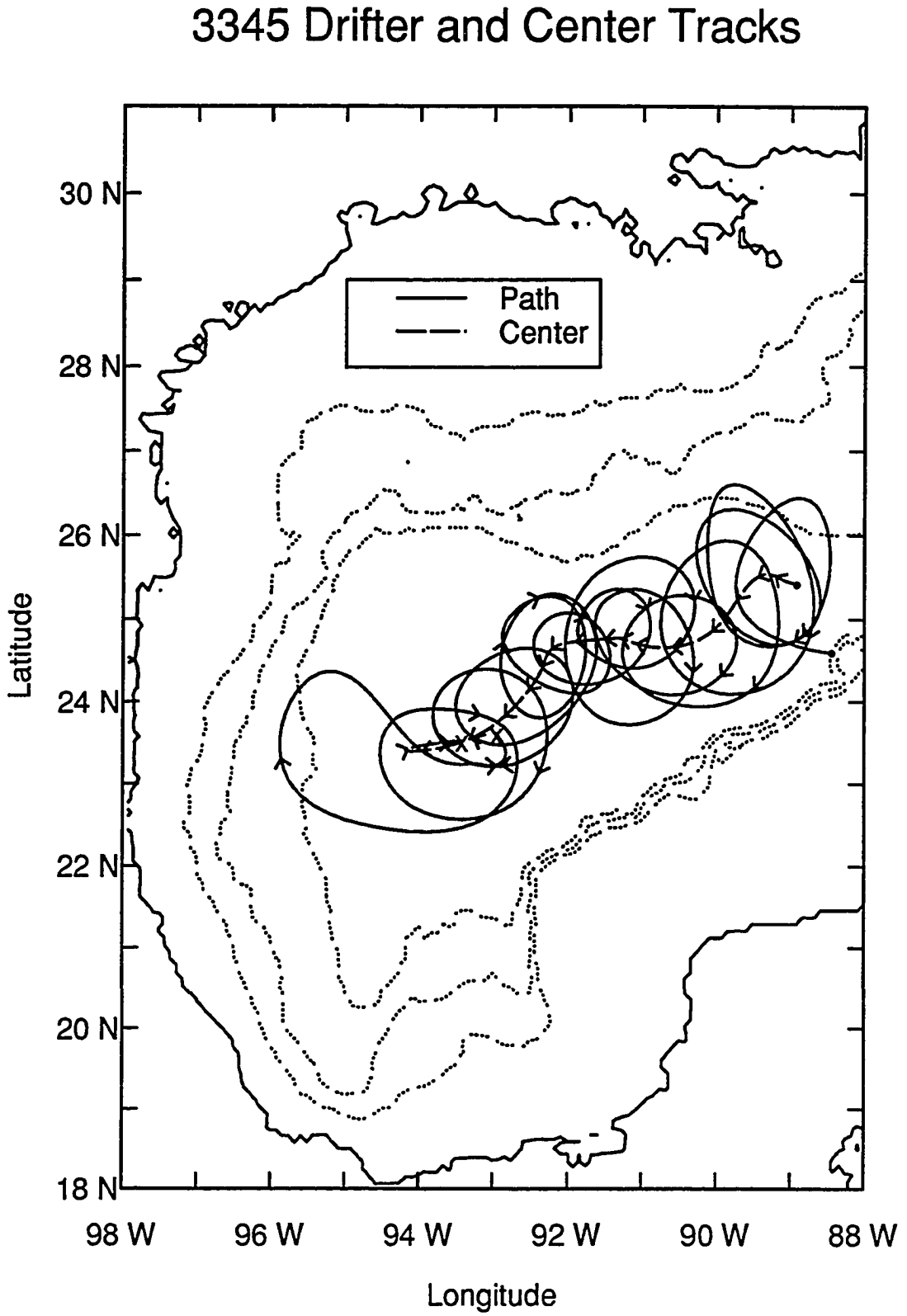

Figure 10. Path trajectory and center track of drifter 3347. The solid line is the actual path of the drifter low-pass filtered at 100 hours and the dashed line is the center track as calculated from a kinematic analysis. Arrows denote 10 day intervals. The solid dot and X mark the start and end, respectively.

3347 Drifter and Center Tracks

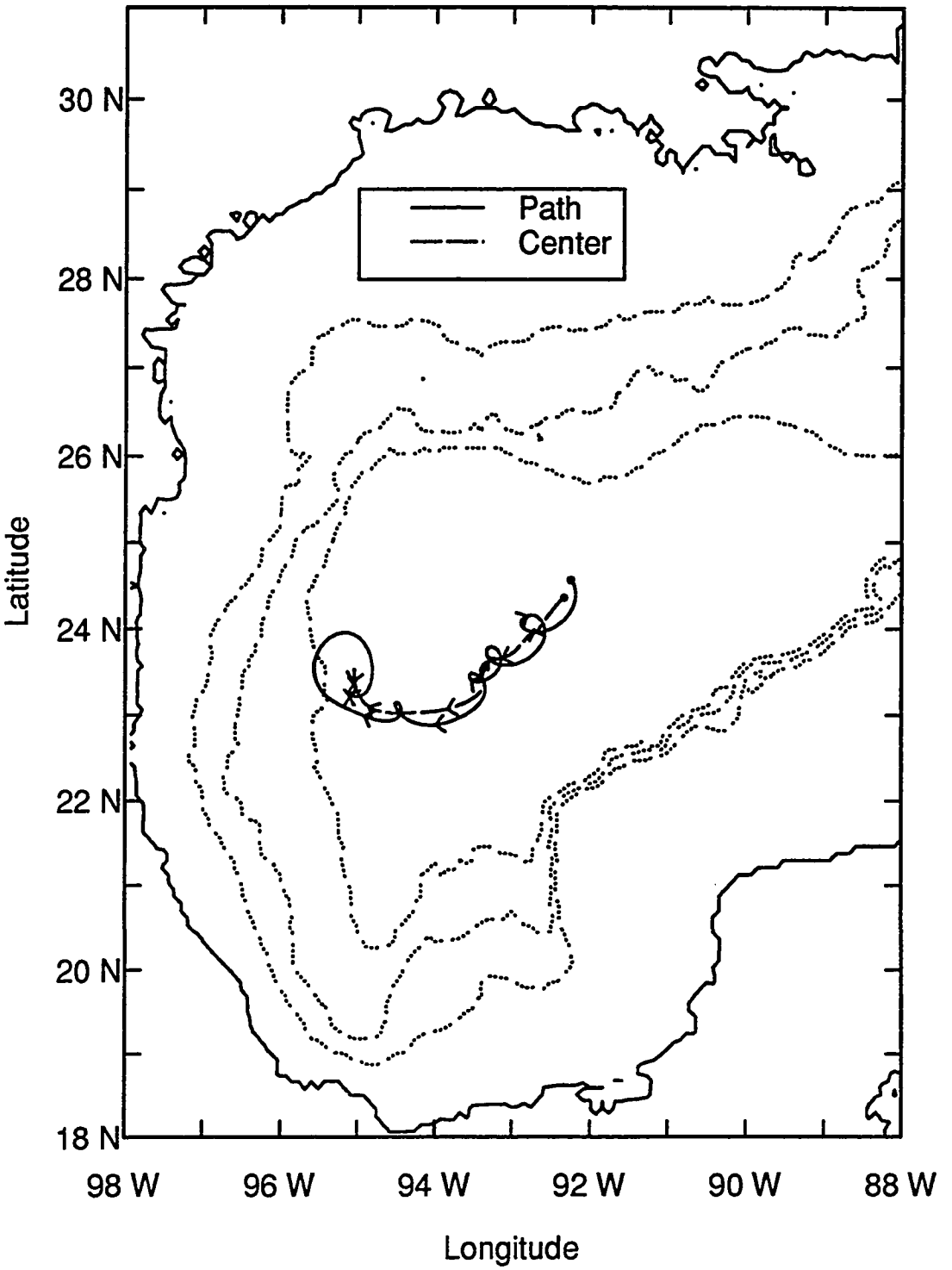

Figure 11. Center paths as determined from observed drifter paths (1599, 3374, 3375 and 5495) and paths generated from the NOARL model (Drifters 1 and 2). The solid dot and X mark the start and end, respectively, of each path.

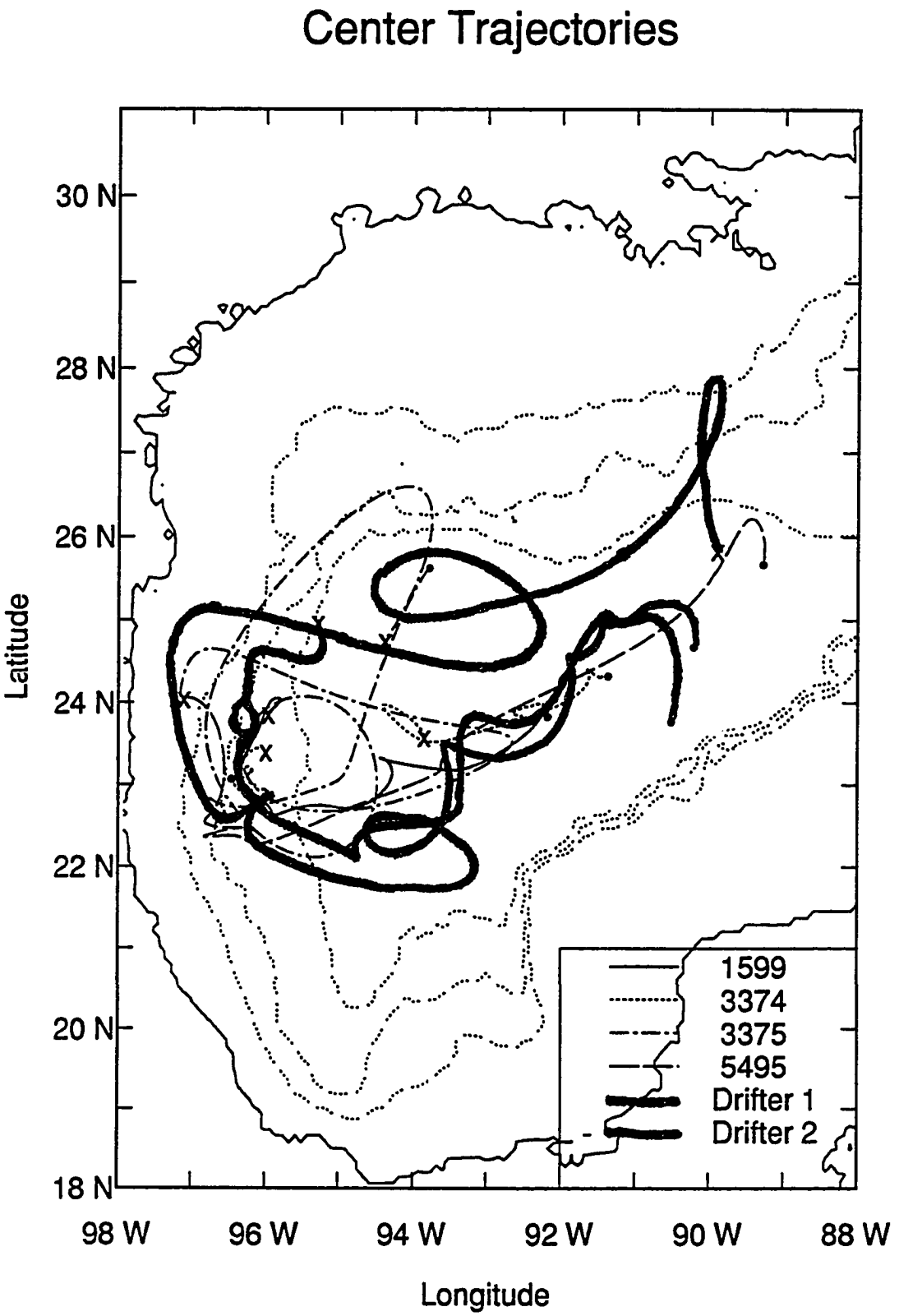

Figure 12. Center paths as determined from observed drifter paths (3353, 3378, 3379, 3345 and 3347) and paths generated from the NOARL model (Drifters 1 and 2). The solid dot and X mark the start and end, respectively, of each path.

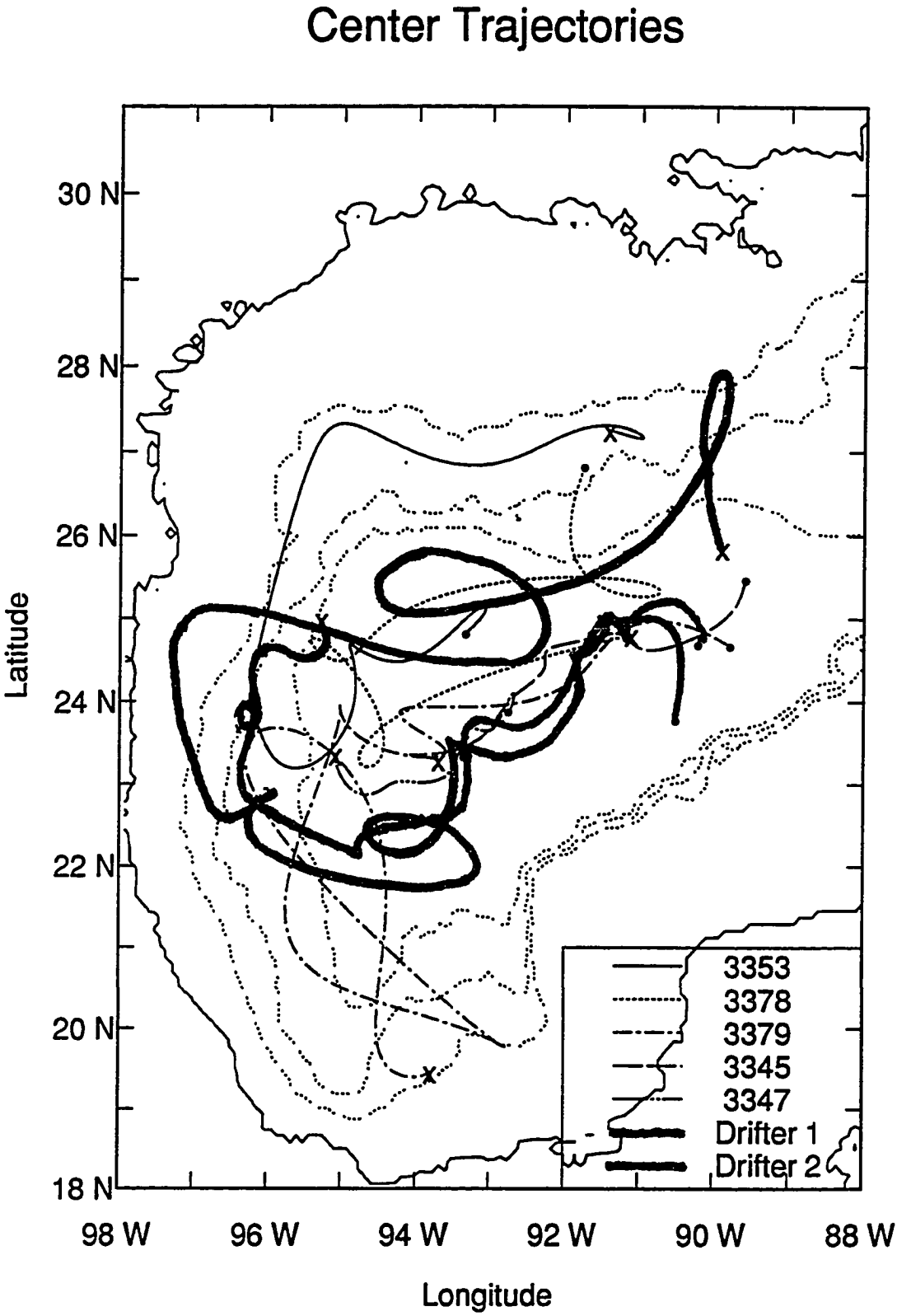

Figure 13. a) Upper layer thickness in the western Gulf of Mexico for NOARL model day 1800. The contour interval is 10 meters. The rest thickness for all upper layer thickness plots is 200 m. The minimum and maximum thickness are 133.56 and 353.15 m.

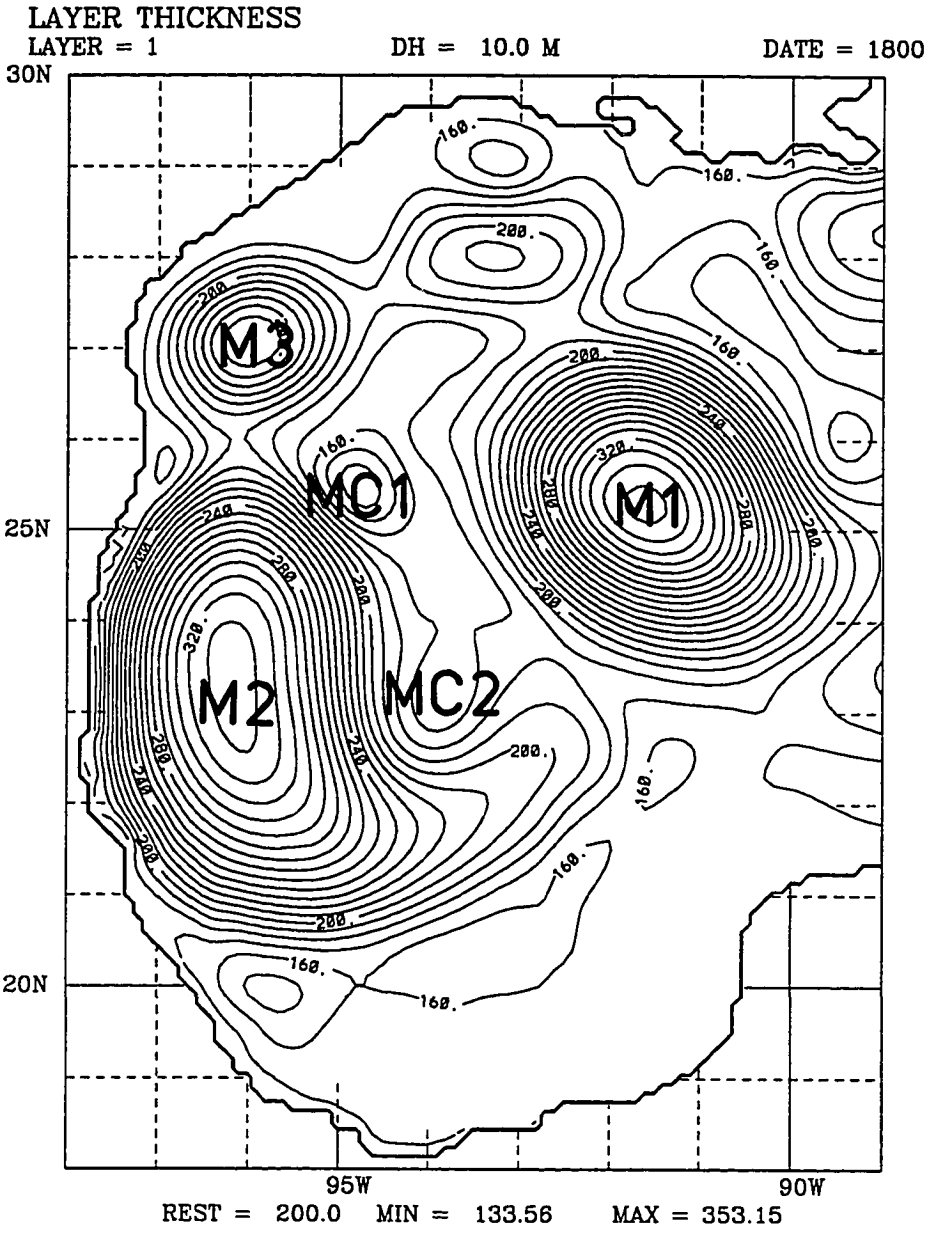

Figure 13. b) Upper layer current velocities in the western Gulf of Mexico for NOARL model day 1800. The maximum speed is 1.234 $m/sec.$ Isobaths are shown in meters.

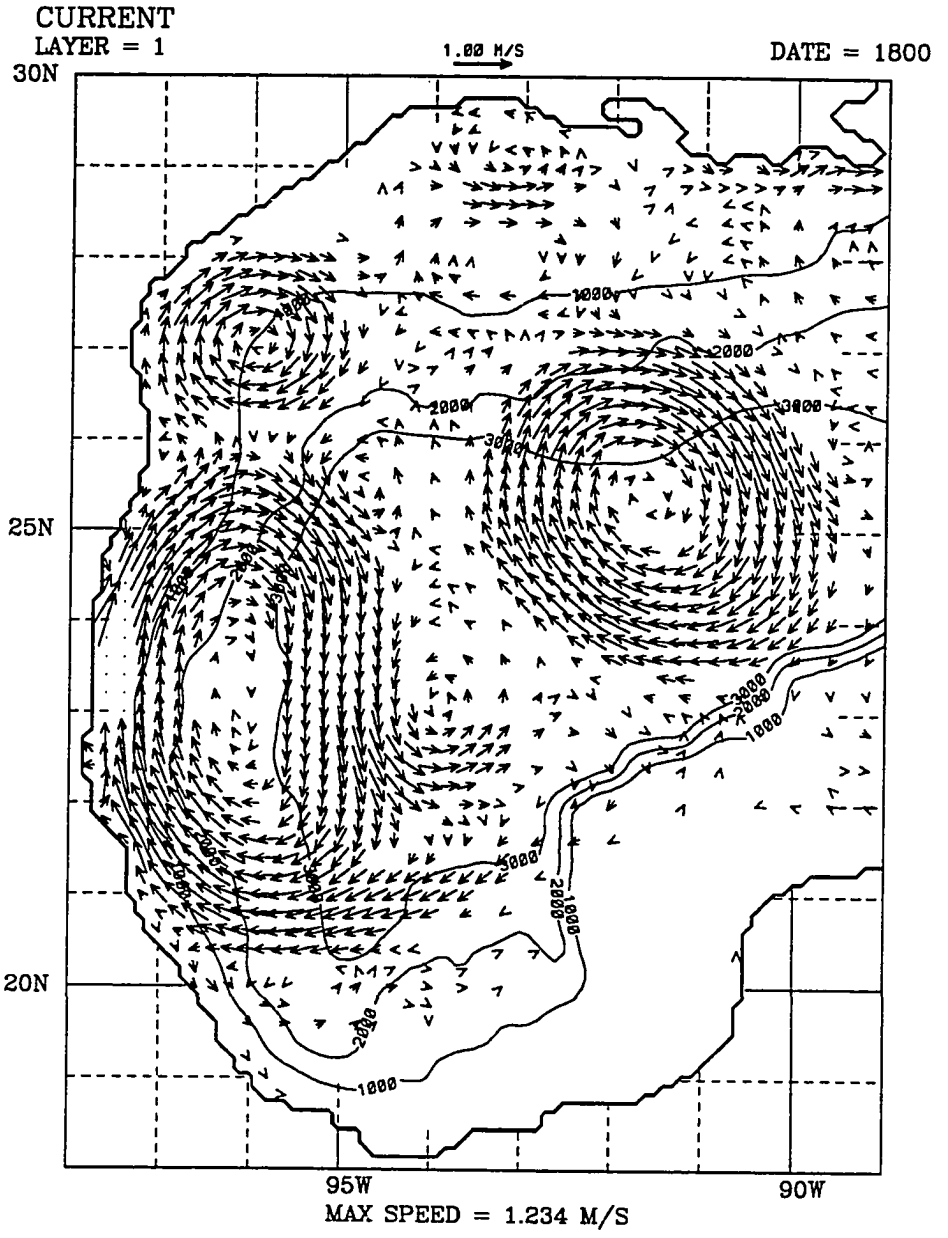

Figure 13. c) Lower layer current velocities in the western Gulf of Mexico for NOARL model day 1800. The maximum speed is .23 $m/sec.$

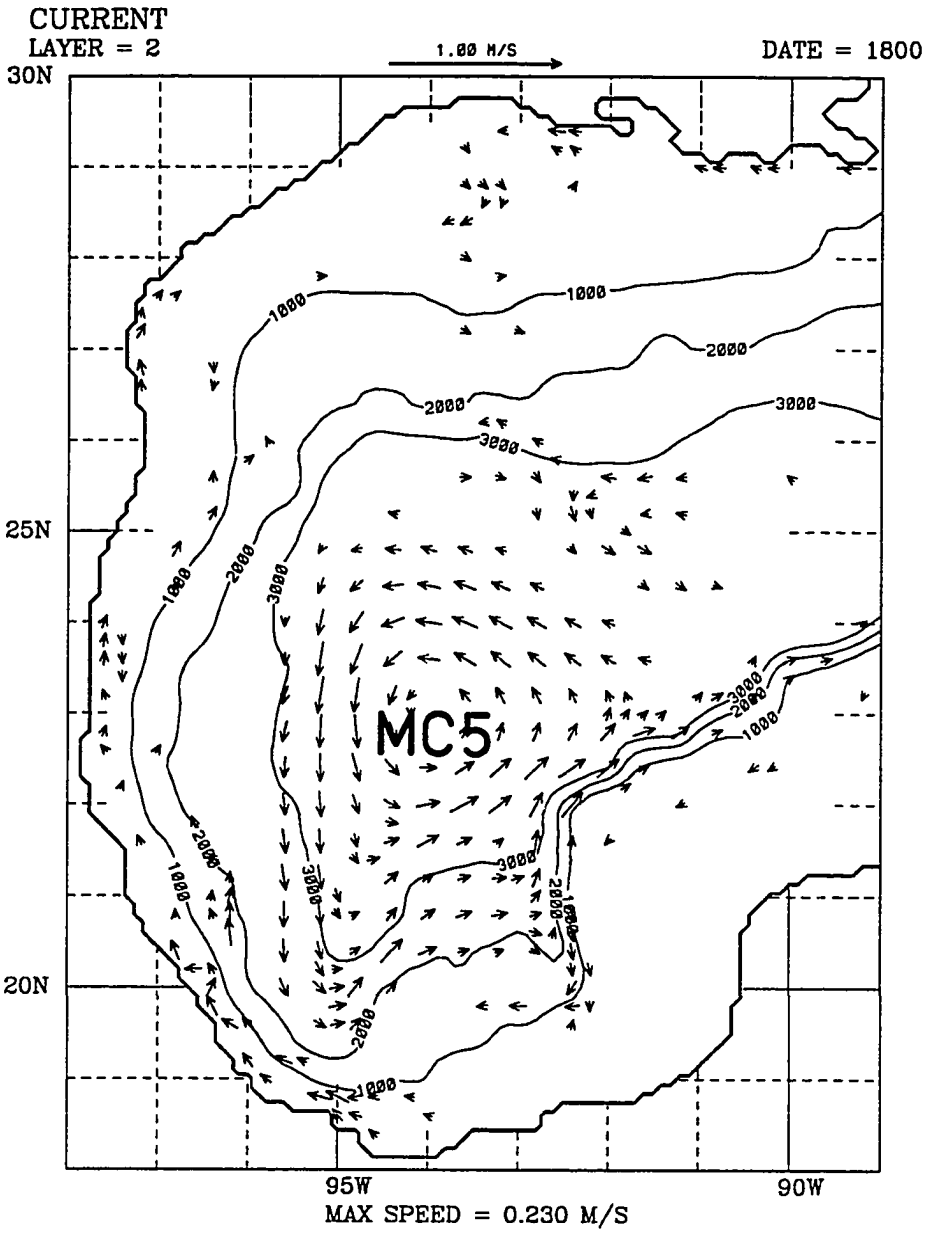

Figure 14. a) Upper layer thickness in the western Gulf of Mexico for NOARL model day 1810. The minimum and maximum thickness are 135.70 and 351.33 m.

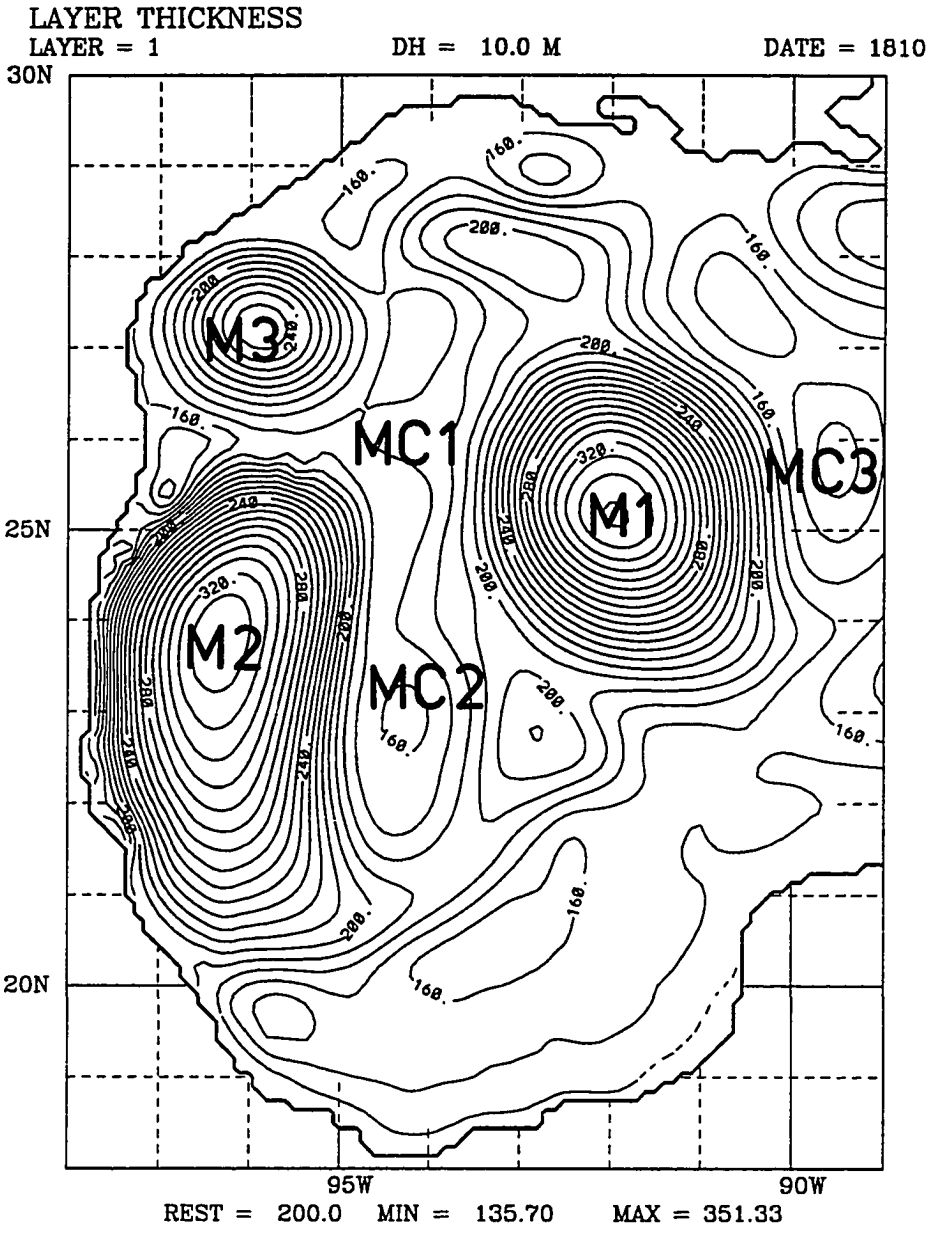

Figure 14. b) Upper layer current velocities in the western Gulf of Mexico for NOARL model day 1810. The maximum speed is 1.575 $m/sec.$ Isobaths are shown in meters.

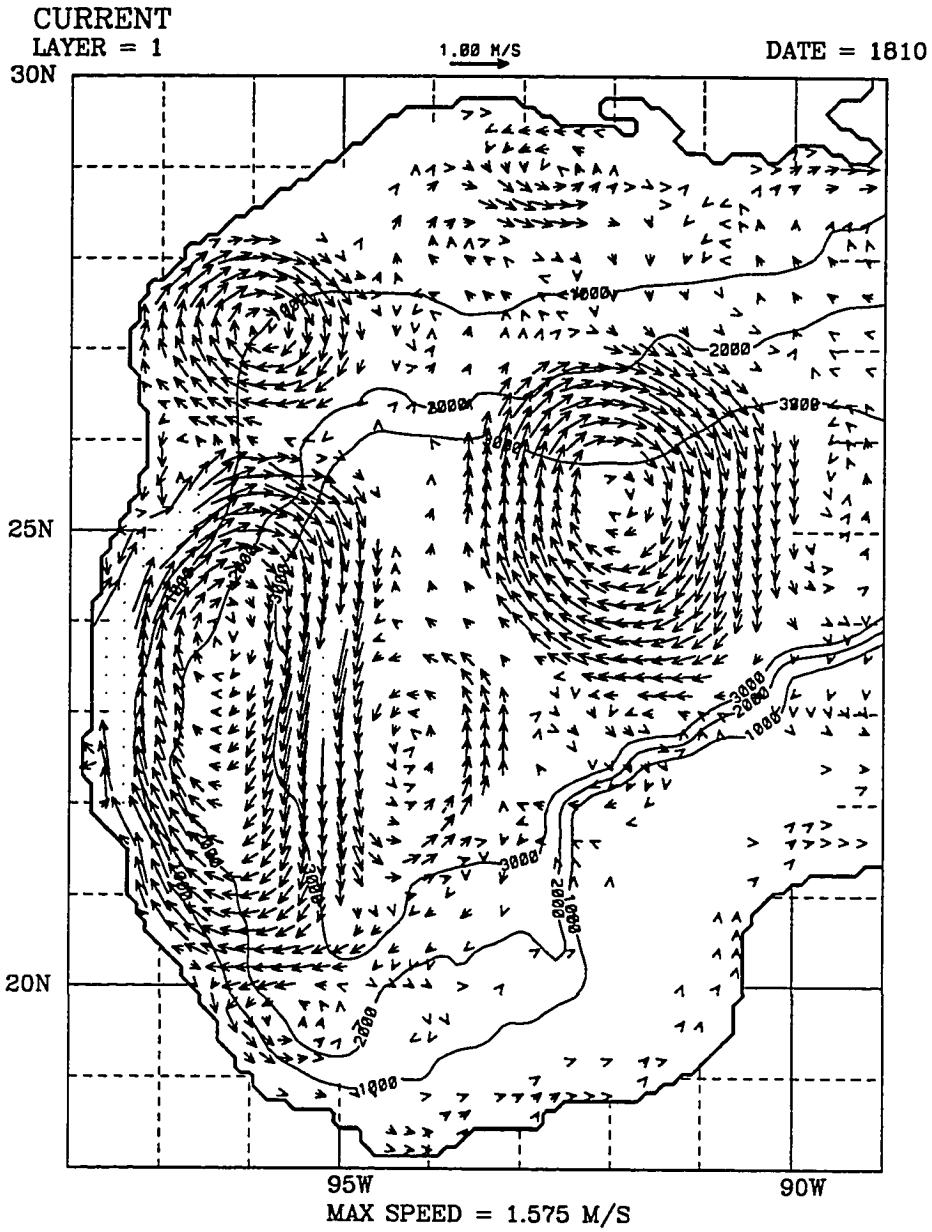

Figure 14. c) Lower layer current velocities in the western Gulf of Mexico for NOARL model day 1810. The maximum speed is .28 m/sec.

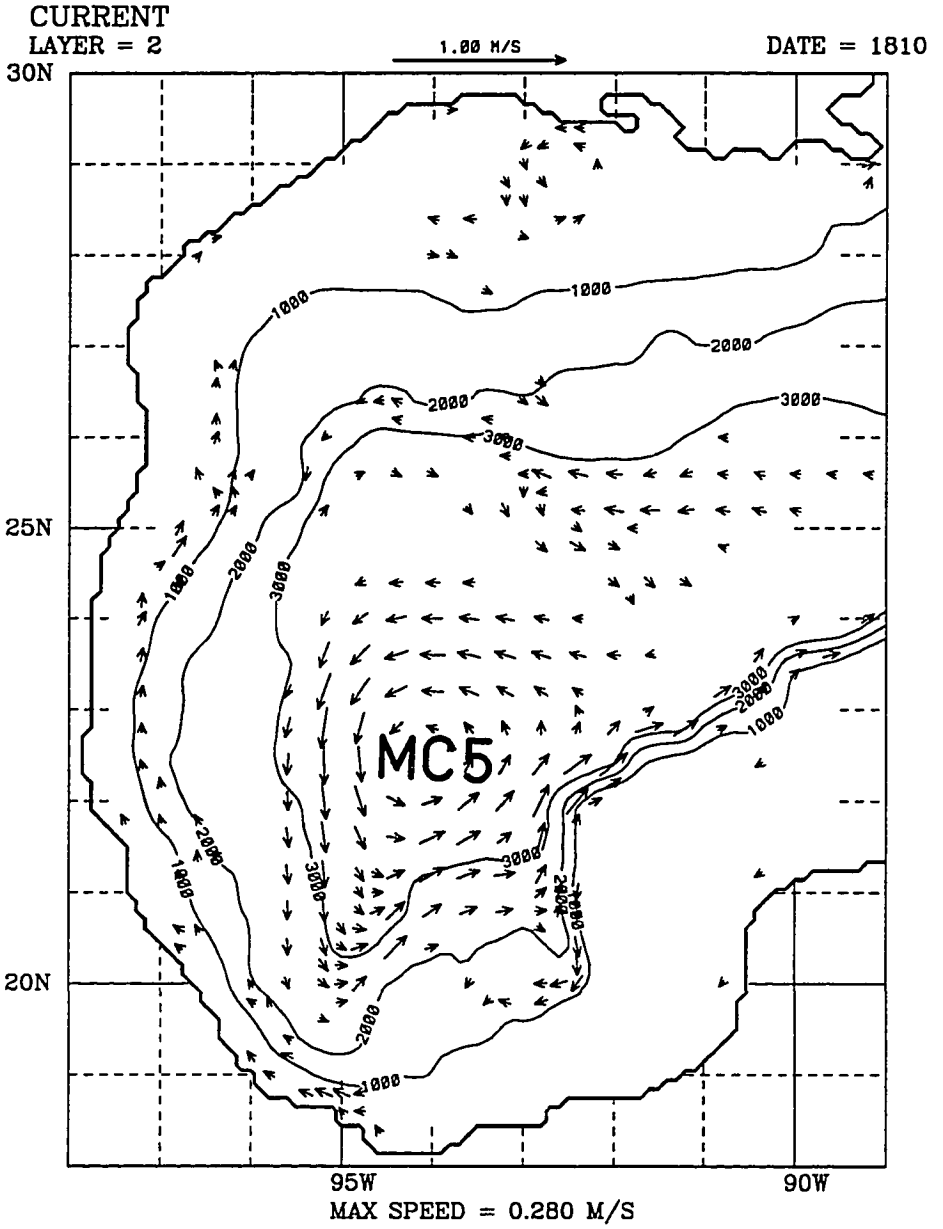

Figure 15. a) Upper layer thickness in the western Gulf of Mexico for NOARL model day 1820. The minimum and maximum thickness are 108.97 and 347.80 m.

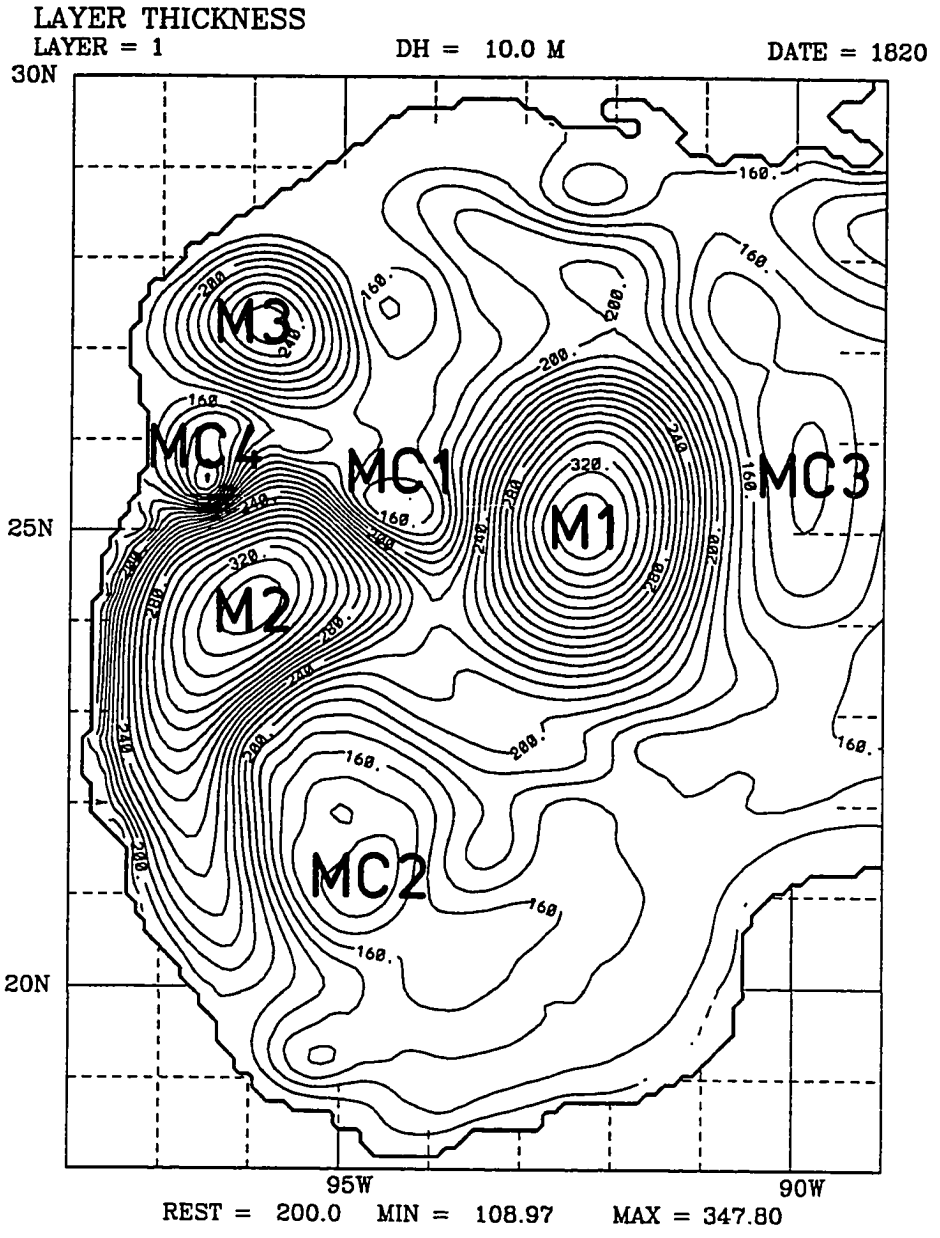

Figure 15. b) Upper layer current velocities in the western Gulf of Mexico for NOARL model day 1820. The maximum speed is 1.620 m/sec. Isobaths are shown in meters.

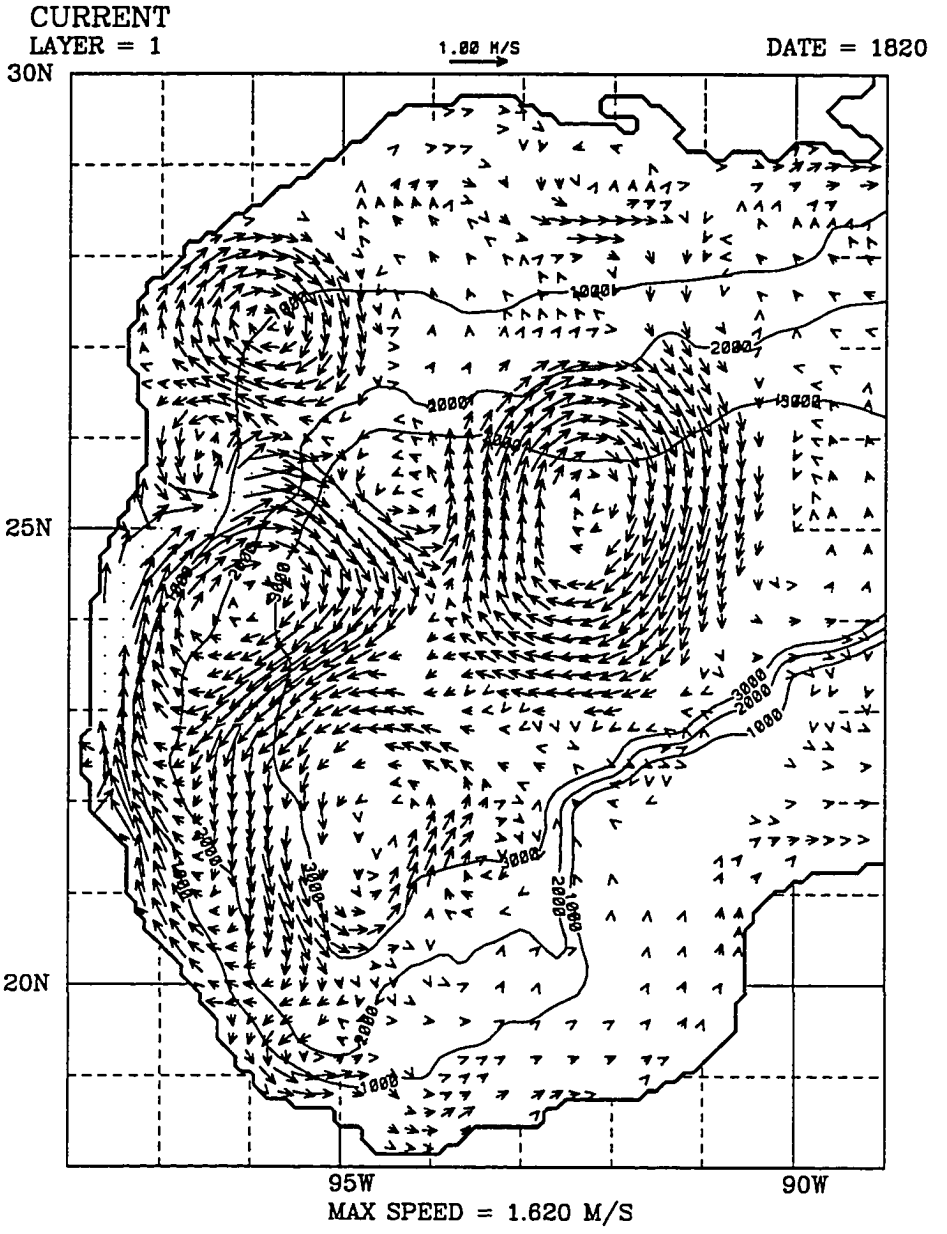

Figure 15. c) Lower layer current velocities in the western Gulf of Mexico for NOARL model day 1820. The maximum speed is .258 m/sec.

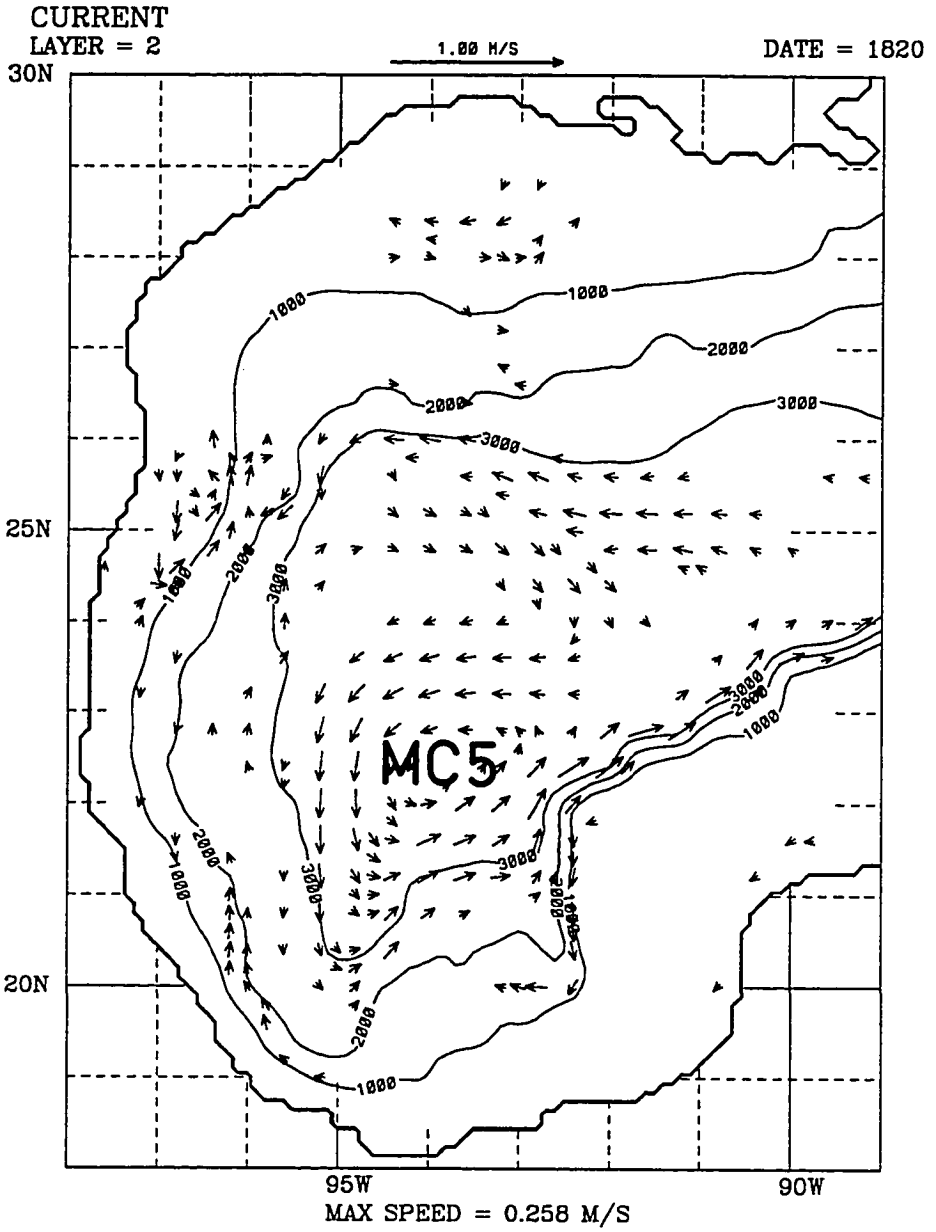

Figure 16. a) Upper layer thickness in the western Gulf of Mexico for NOARL model day 1830. The minimum and maximum thickness are 127.76 and 348.57 m. A partial trajectory from Drifter 3375 is shown by the thickline.

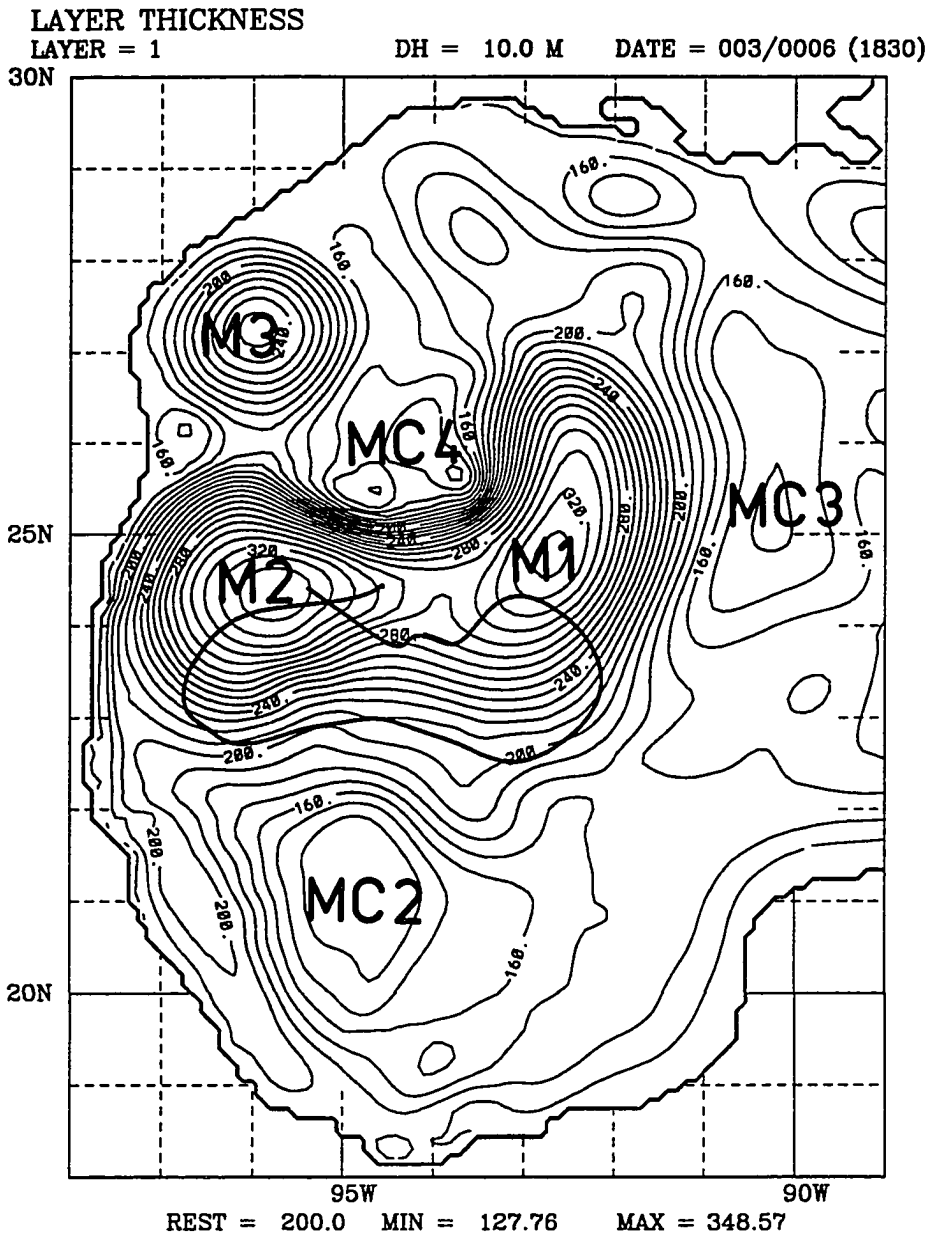

Figure 16. b) Upper layer current velocities in the western Gulf of Mexico for NOARL model day 1830. The maximum speed is 1.416 m/sec. Isobaths are shown in meters.

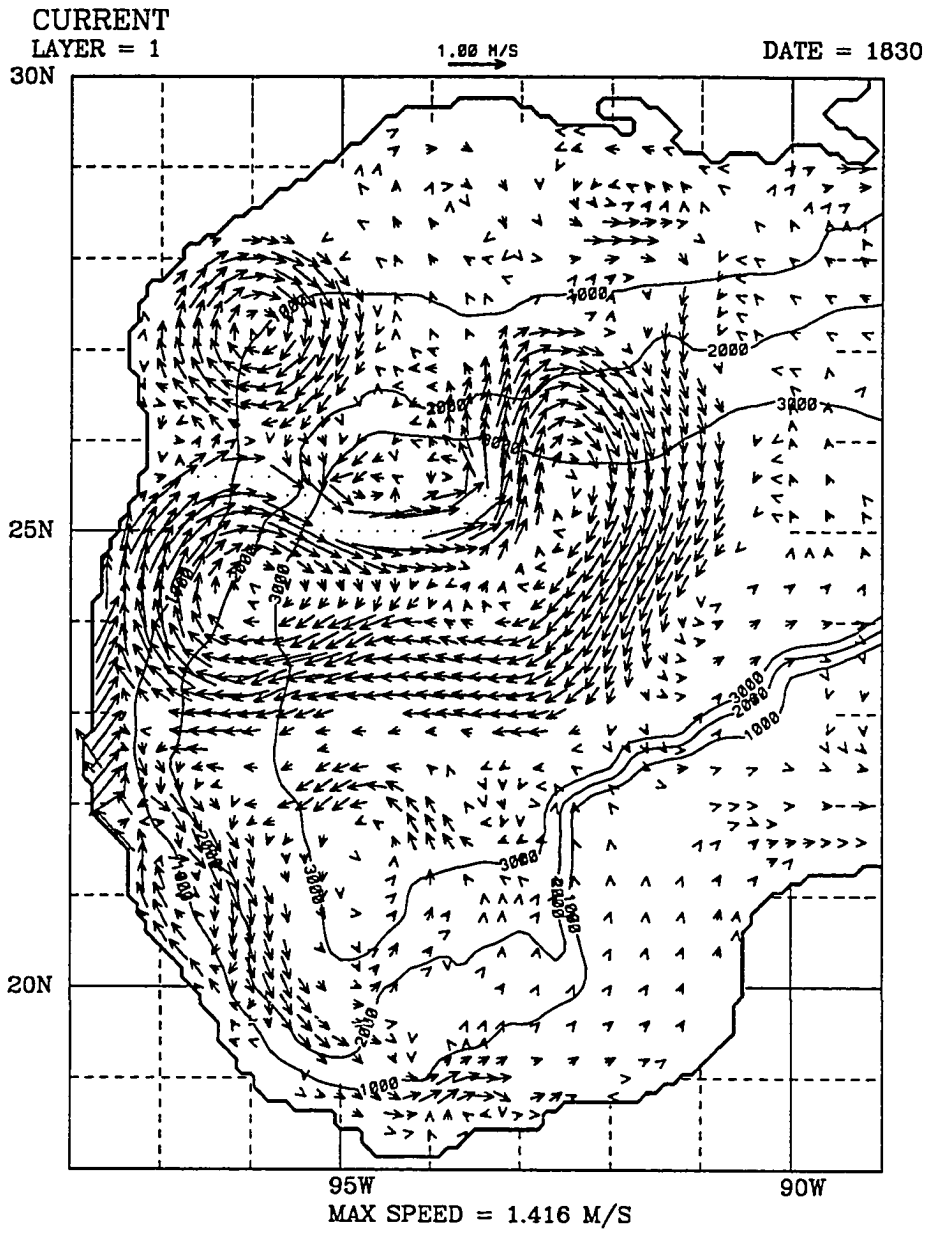

Figure 16. c) Lower layer current velocities in the western Gulf of Mexico for NOARL model day 1830. The maximum speed is .229 m/sec.

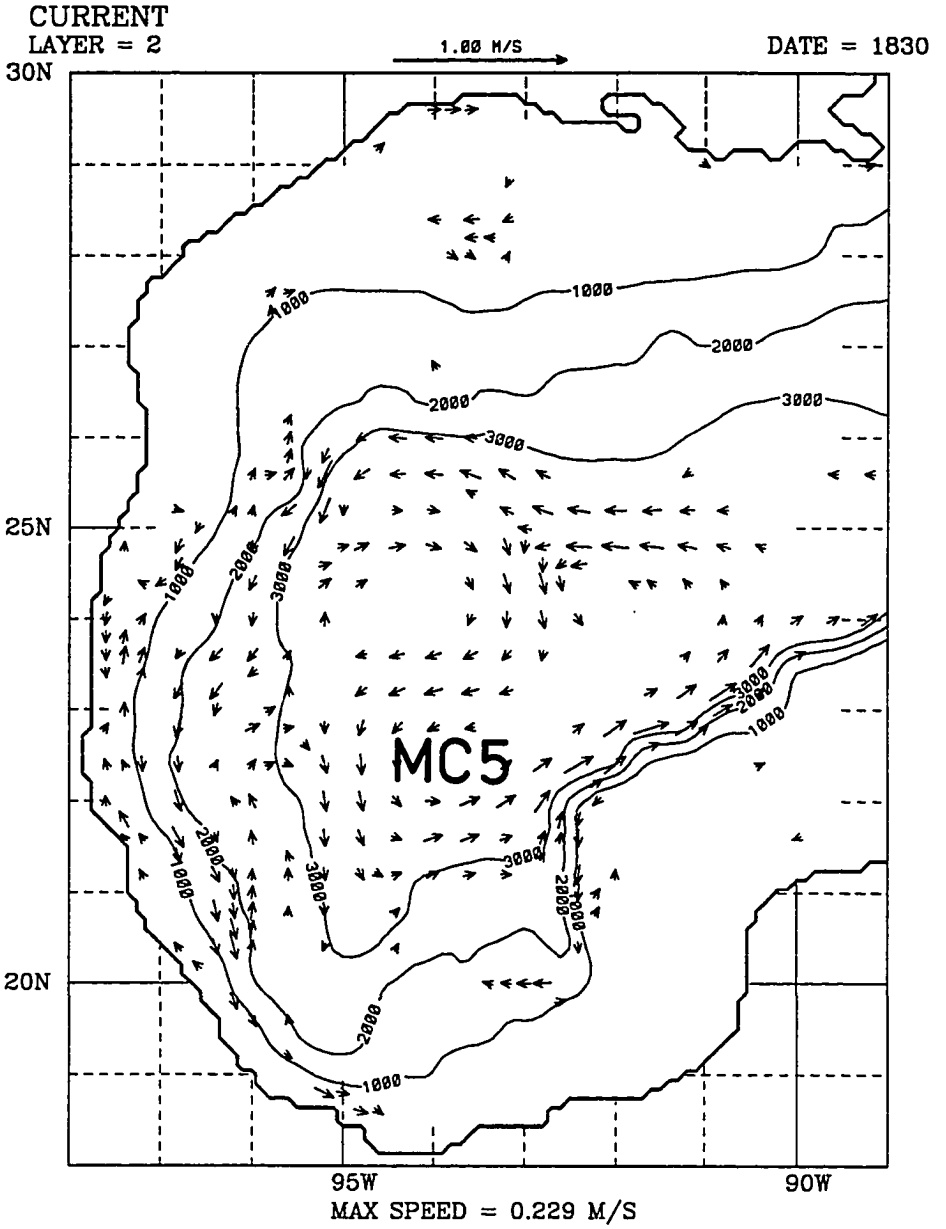

Figure 17. a) Upper layer thickness in the western Gulf of Mexico for NOARL model day 1840. The minimum and maximum thickness are 92.40 and 350.98 m.

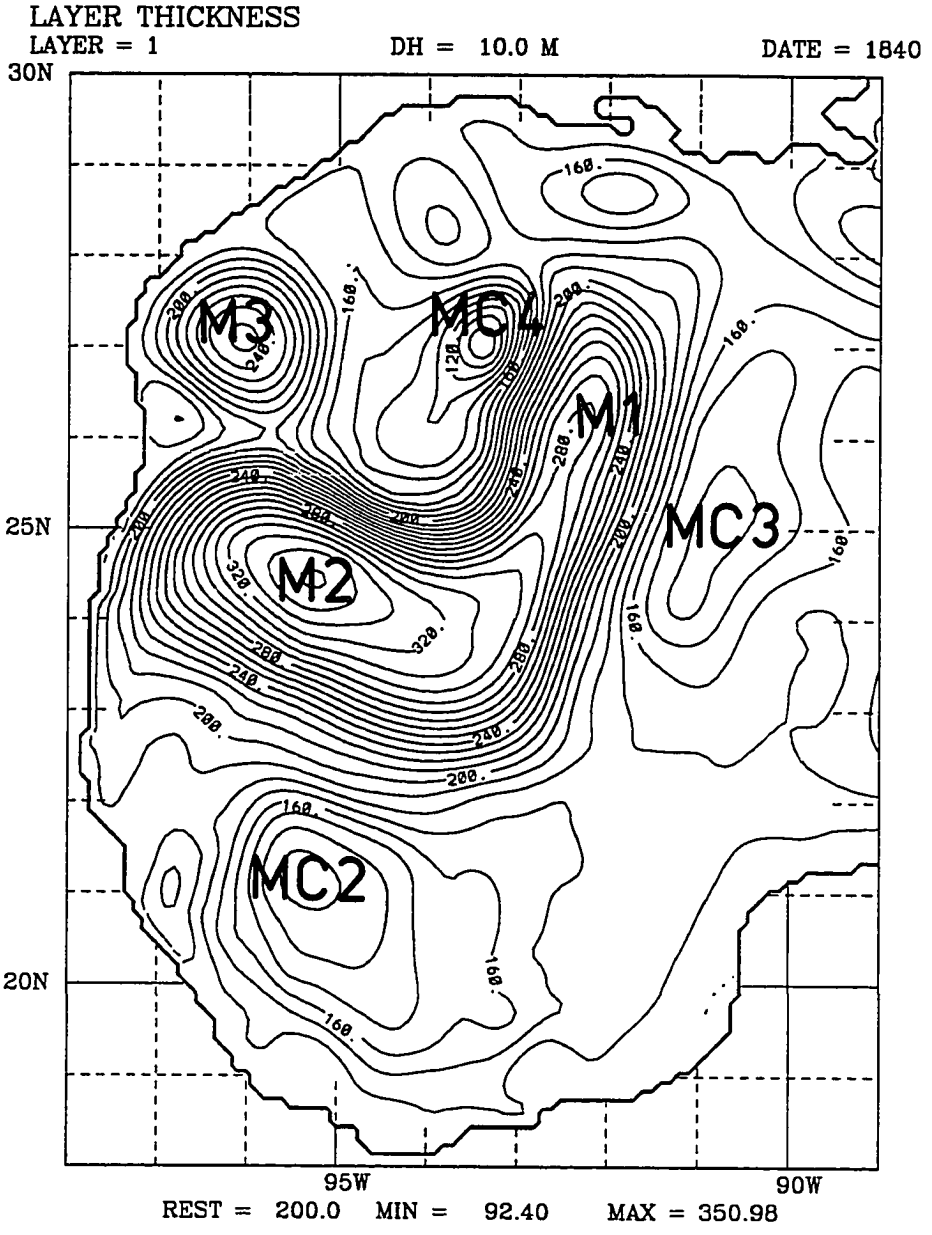

Figure 17. b) Upper layer current velocities in the western Gulf of Mexico for NOARL model day 1840. The maximum speed is 1.136 m/sec. Isobaths are shown in meters.

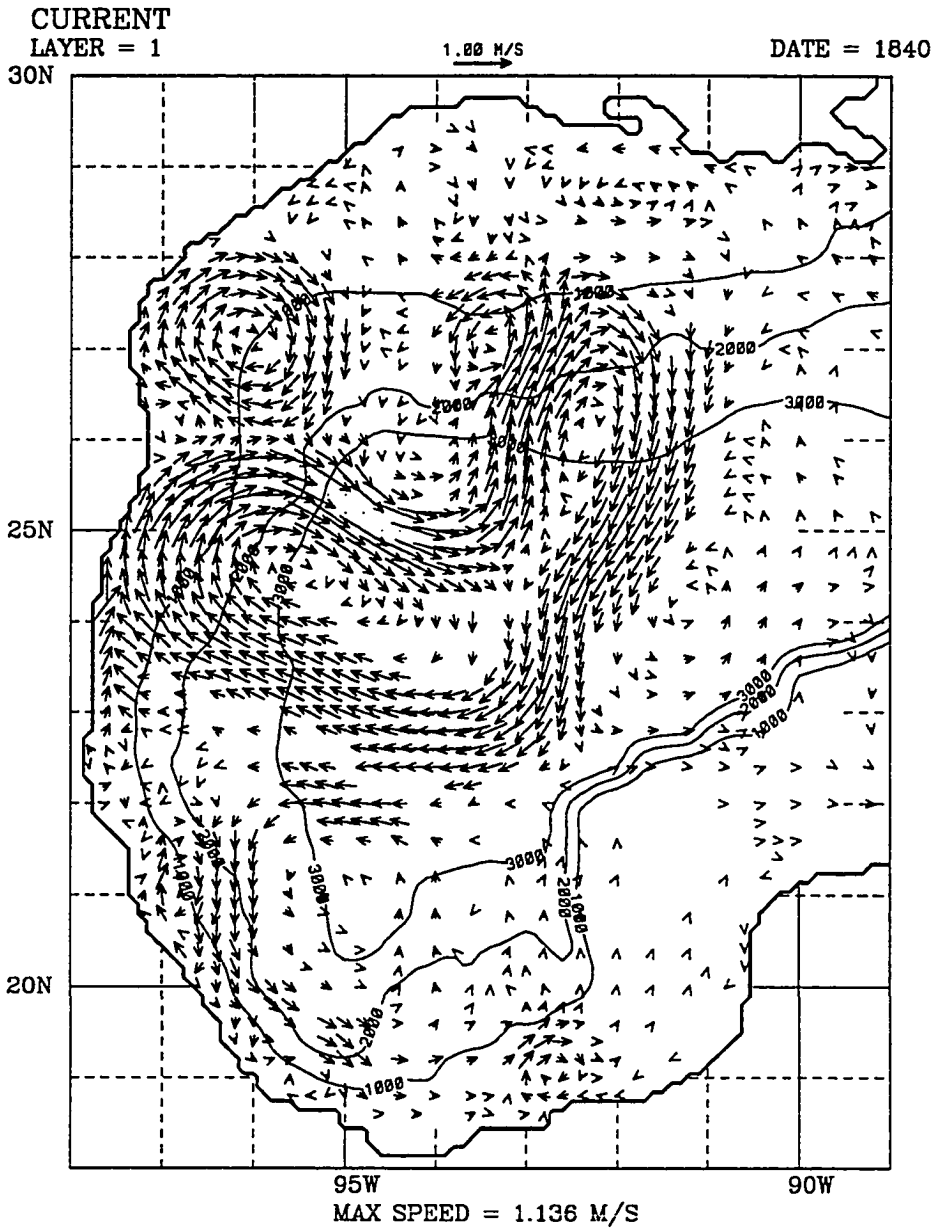

Figure 17. c) Lower layer current velocities in the western Gulf of Mexico for NOARL model day 1840. The maximum speed is .248 m/sec.

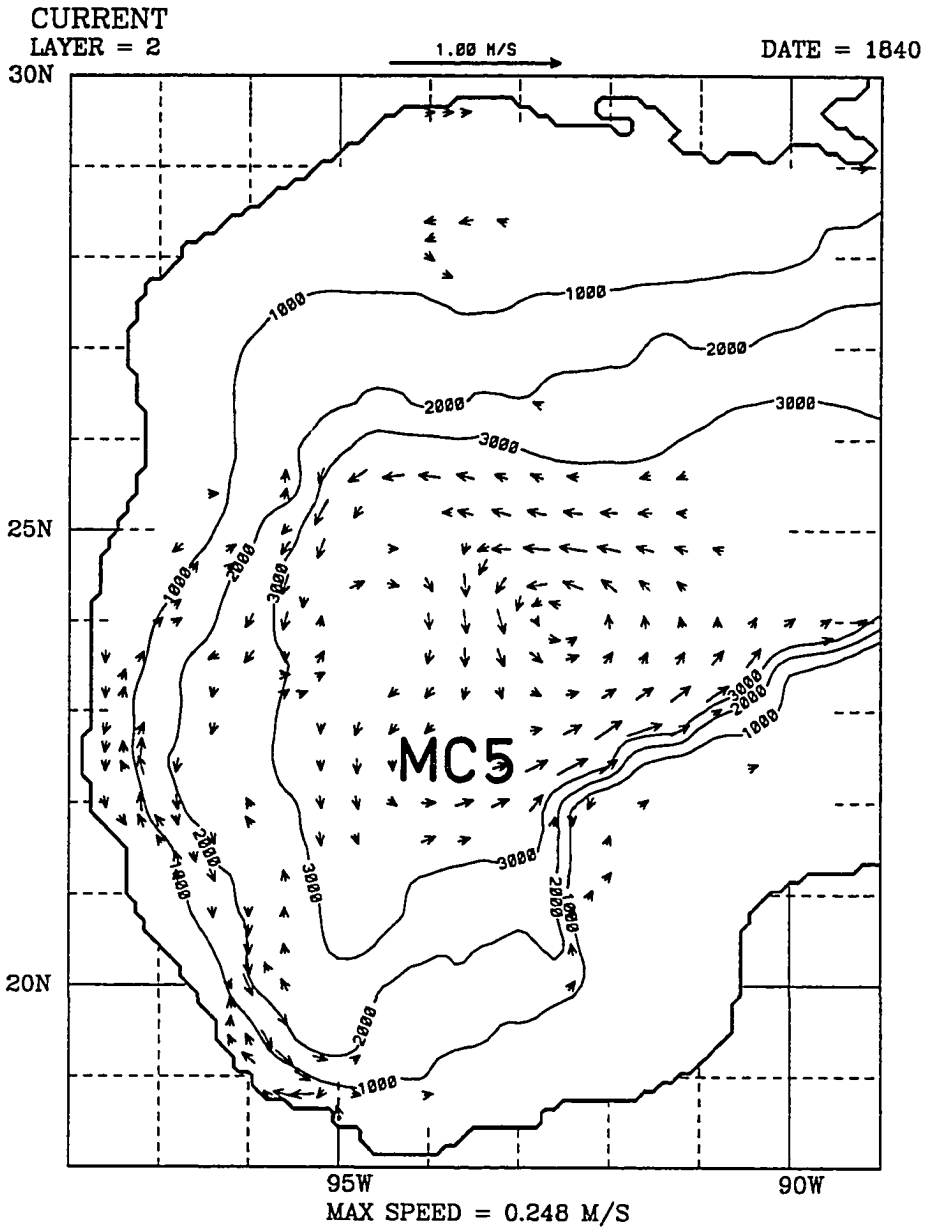

Figure 18. a) Upper layer thickness in the western Gulf of Mexico for NOARL model day 1850. The minimum and maximum thickness are 95.47 and 345.63 m.

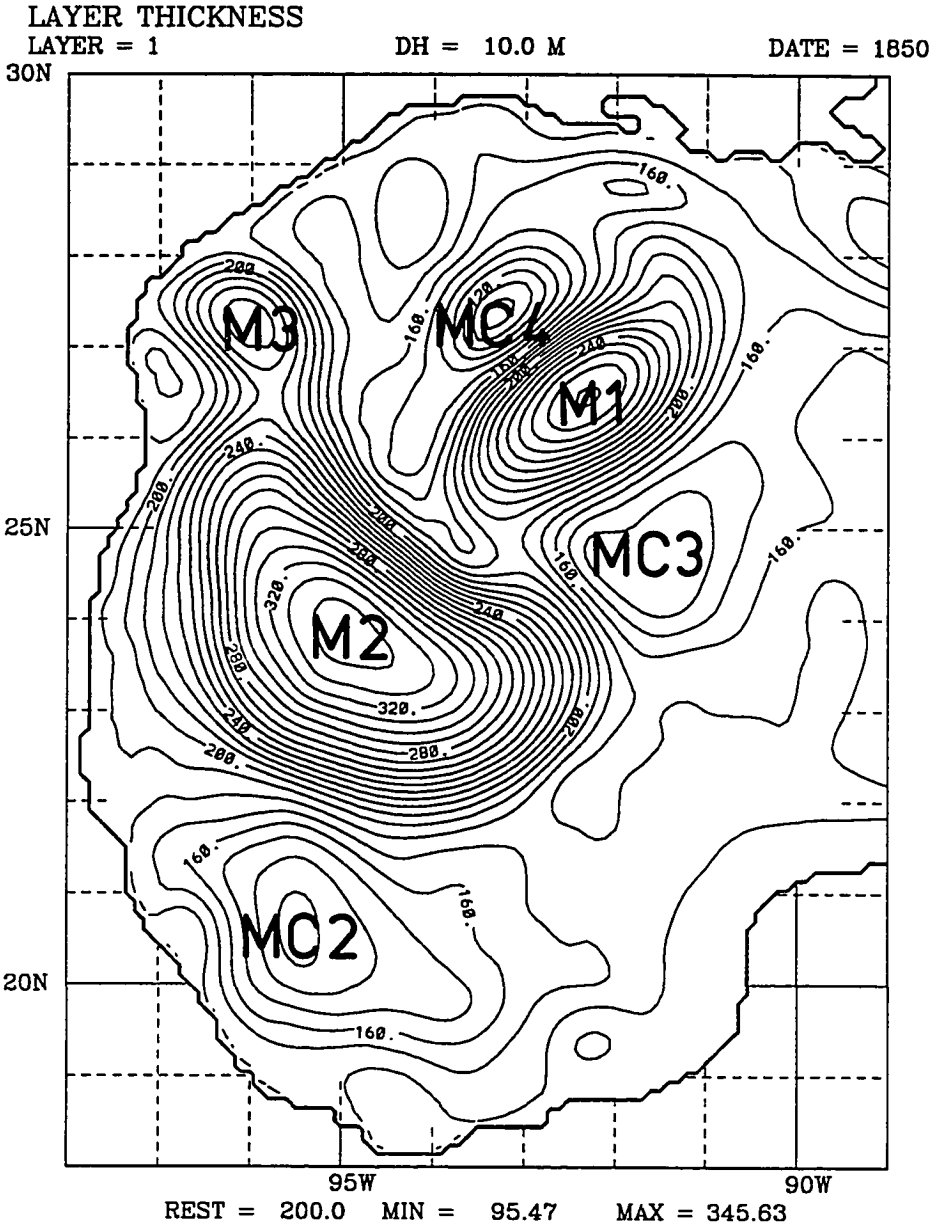

Figure 18. b) Upper layer current velocities in the western Gulf of Mexico for NOARL model day 1850. The maximum speed is 1.155 m/sec. Isobaths are shown in meters.

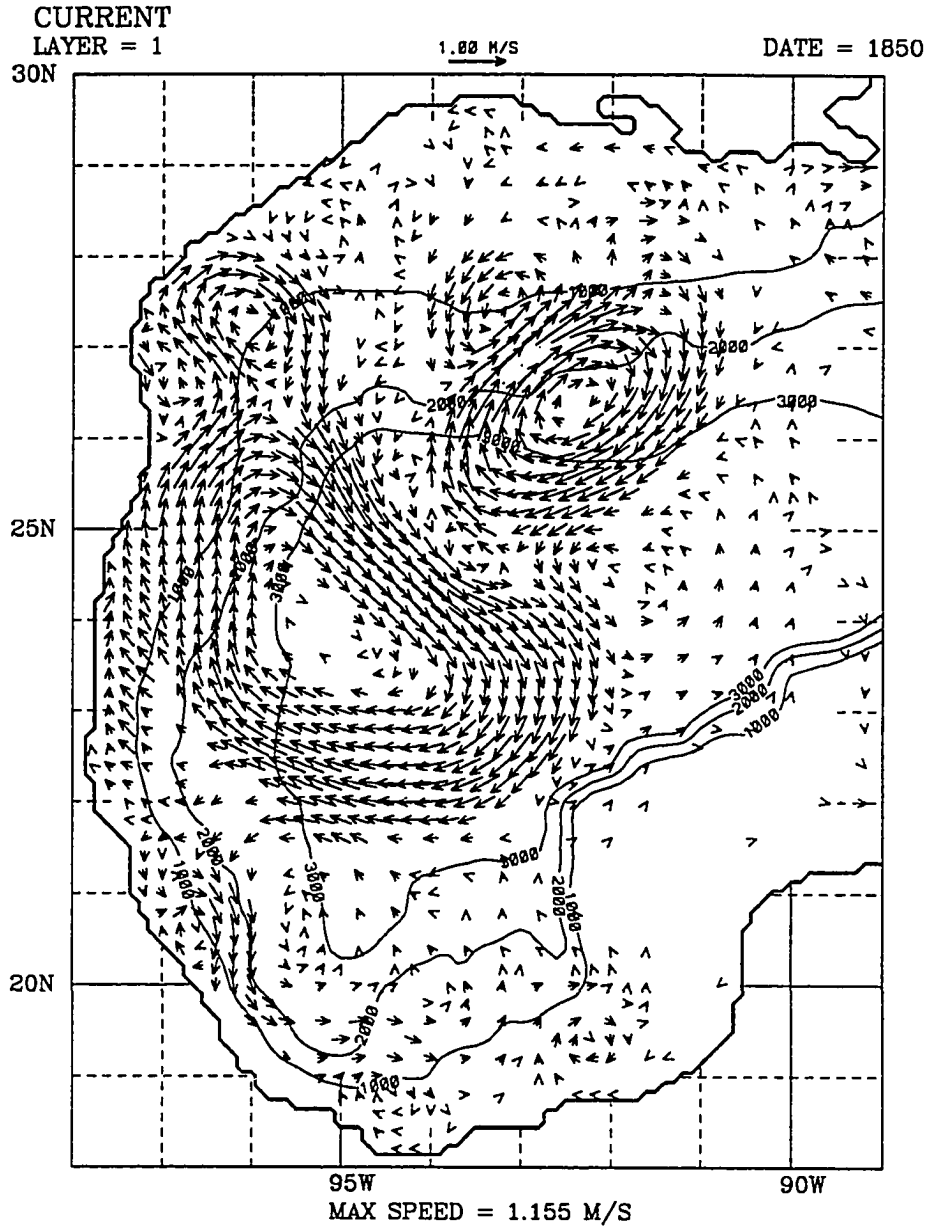

Figure 18. c) Lower layer current velocities in the western Gulf of Mexico for NOARL model day 1850. The maximum speed is .208 m/sec.

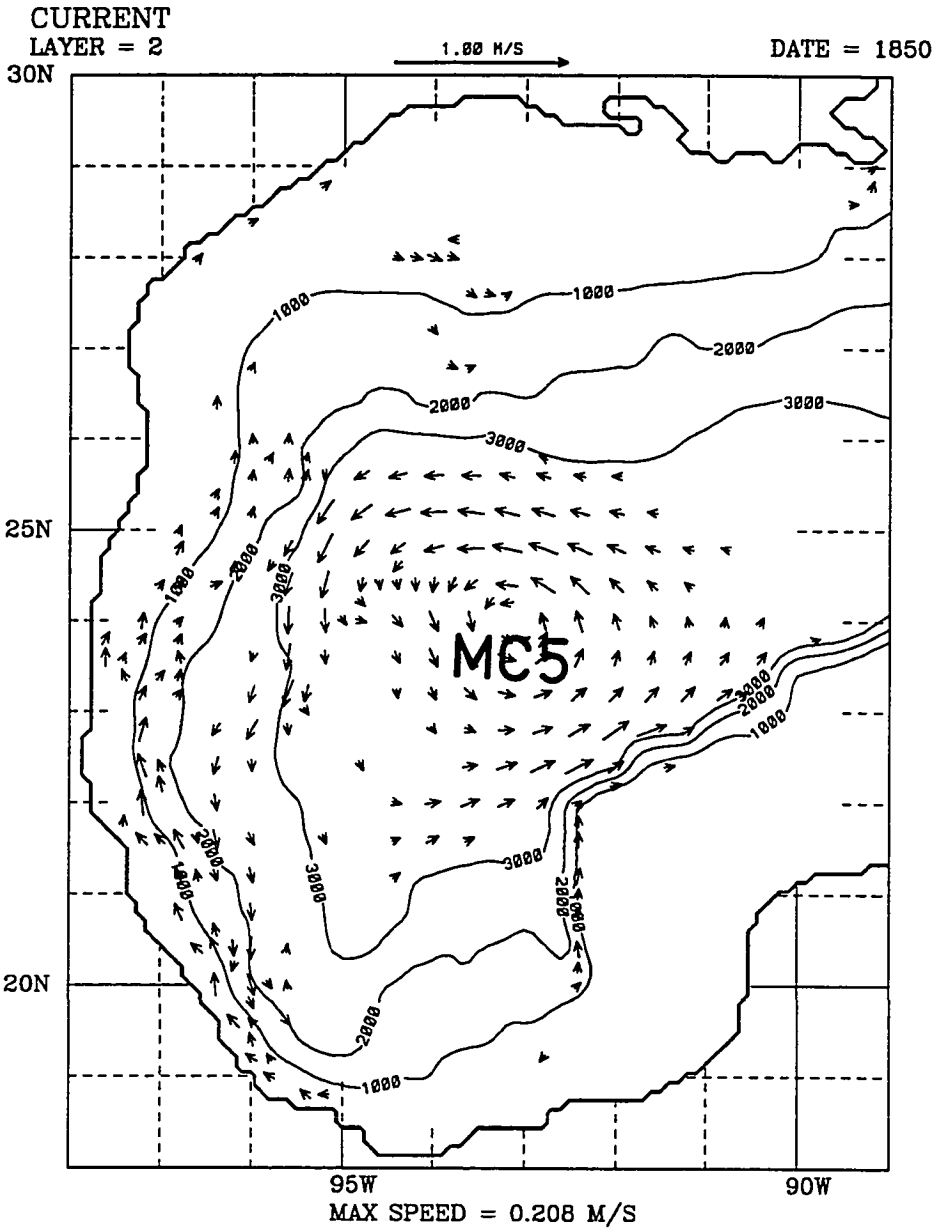

Figure 19. a) Upper layer thickness in the western Gulf of Mexico for NOARL model day 1860. The minimum and maximum thickness are 100.2 and 335.87 m.

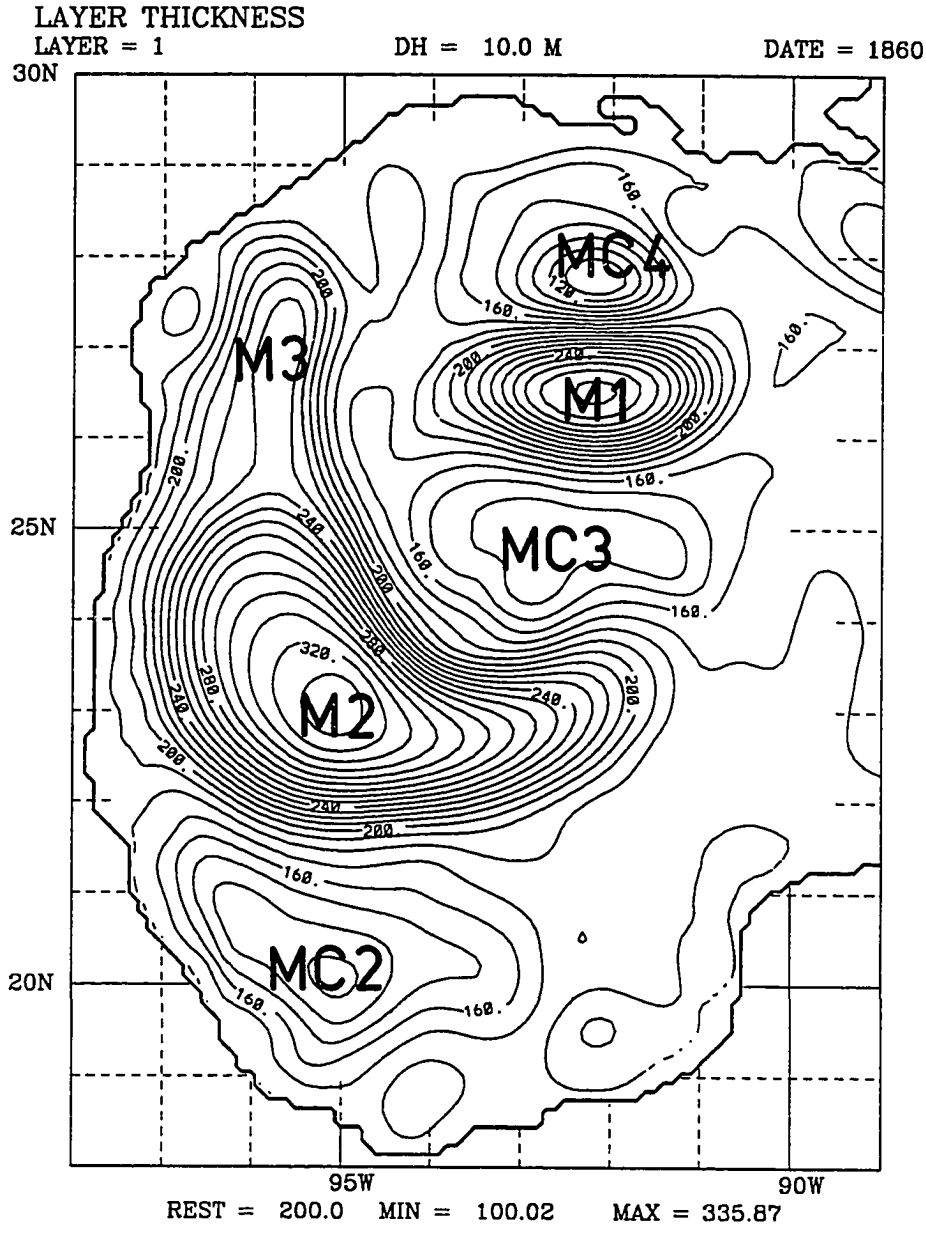

Figure 19. b) Upper layer current velocities in the western Gulf of Mexico for NOARL model day 1860. The maximum speed is 1.002 $m/sec.$ Isobaths are shown in meters.

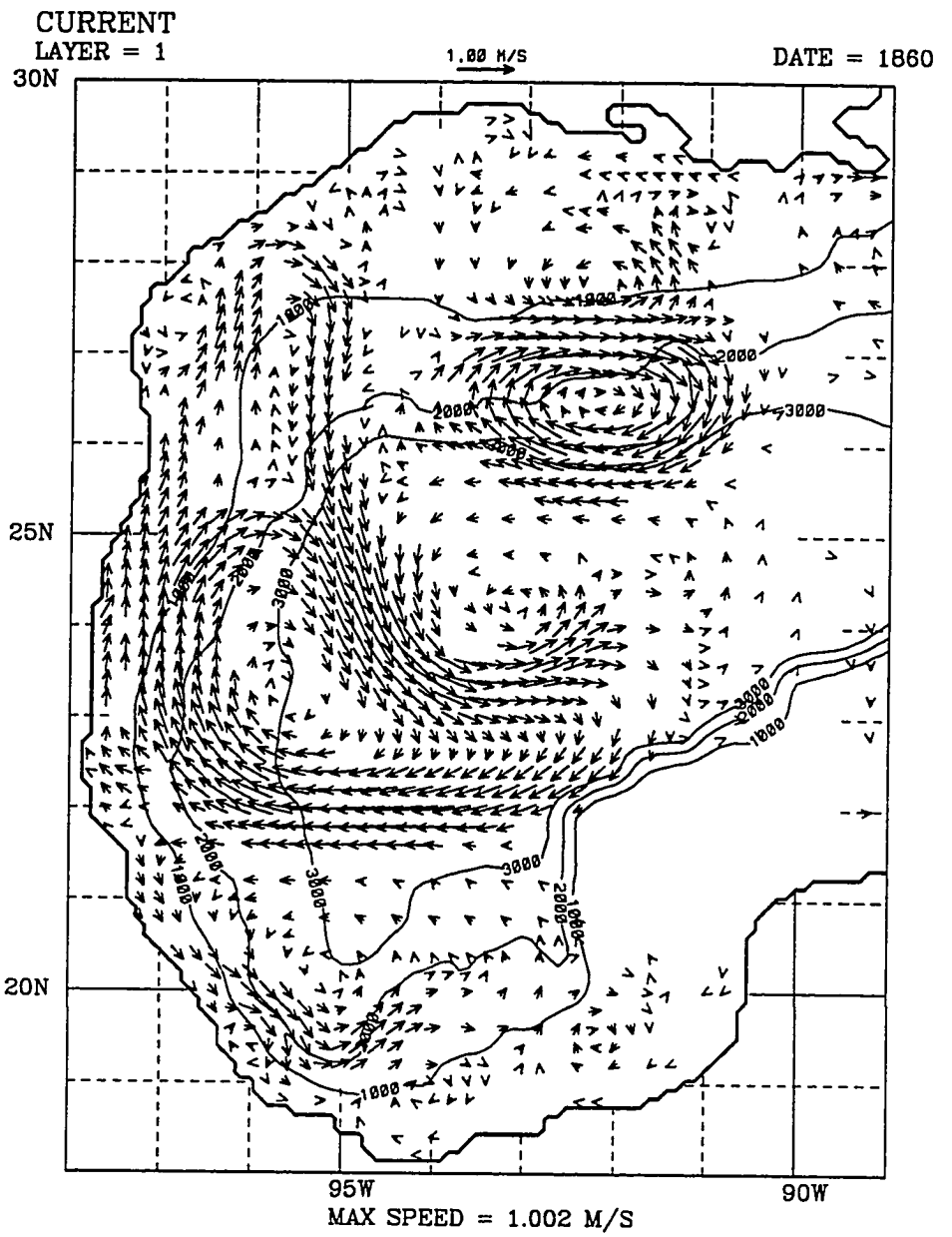

Figure 19. c) Lower layer current velocities in the western Gulf of Mexico for NOARL model day 1860. The maximum speed is .292 m/sec.

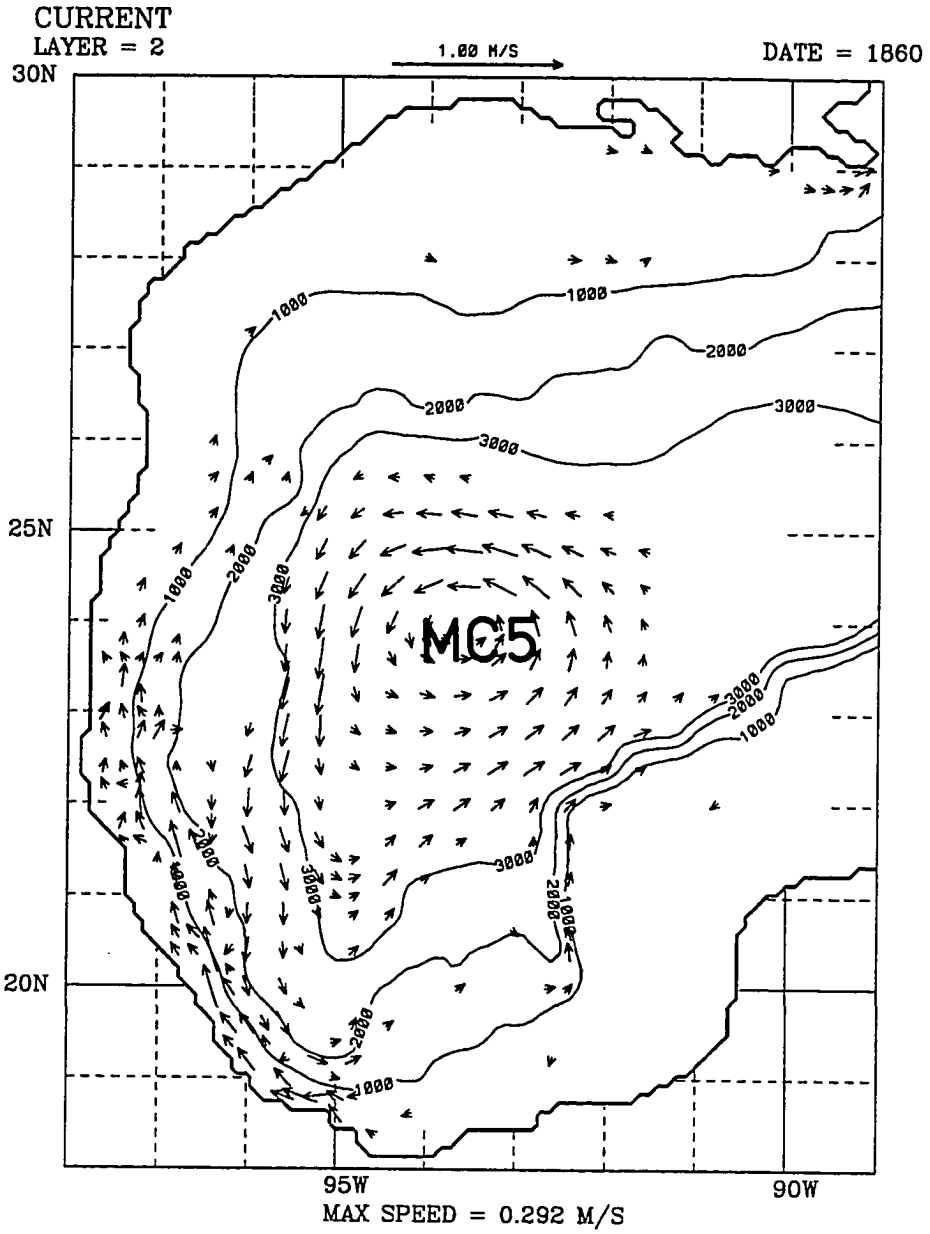

Figure 20. a) Upper layer thickness in the western Gulf of Mexico for NOARL model day 1870. The minimum and maximum thickness are 98.19 and 323.47 m.

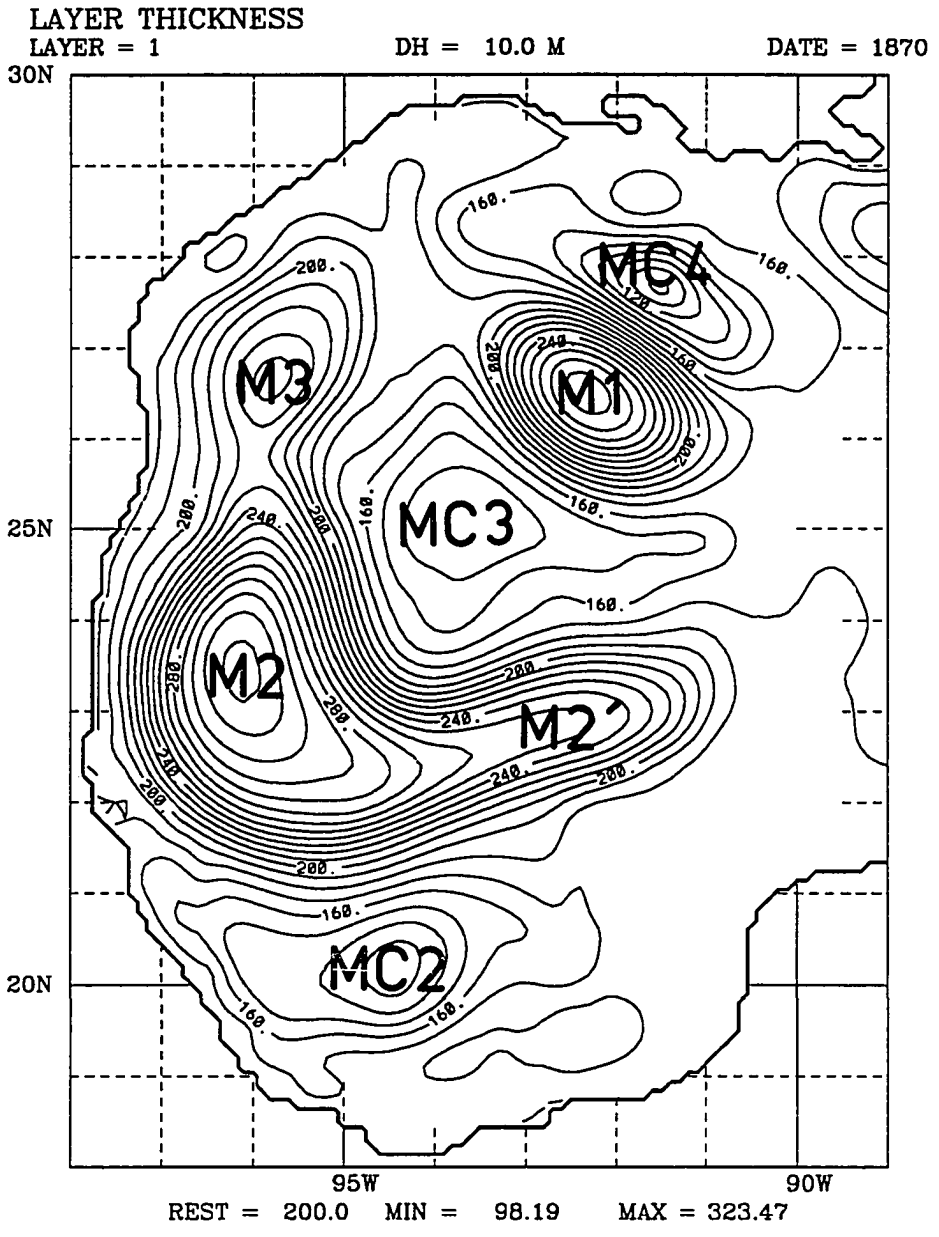

Figure 20. b) Upper layer current velocities in the western Gulf of Mexico for NOARL model day 1870. The maximum speed is .944 $m/sec.$ Isobaths are shown in meters.

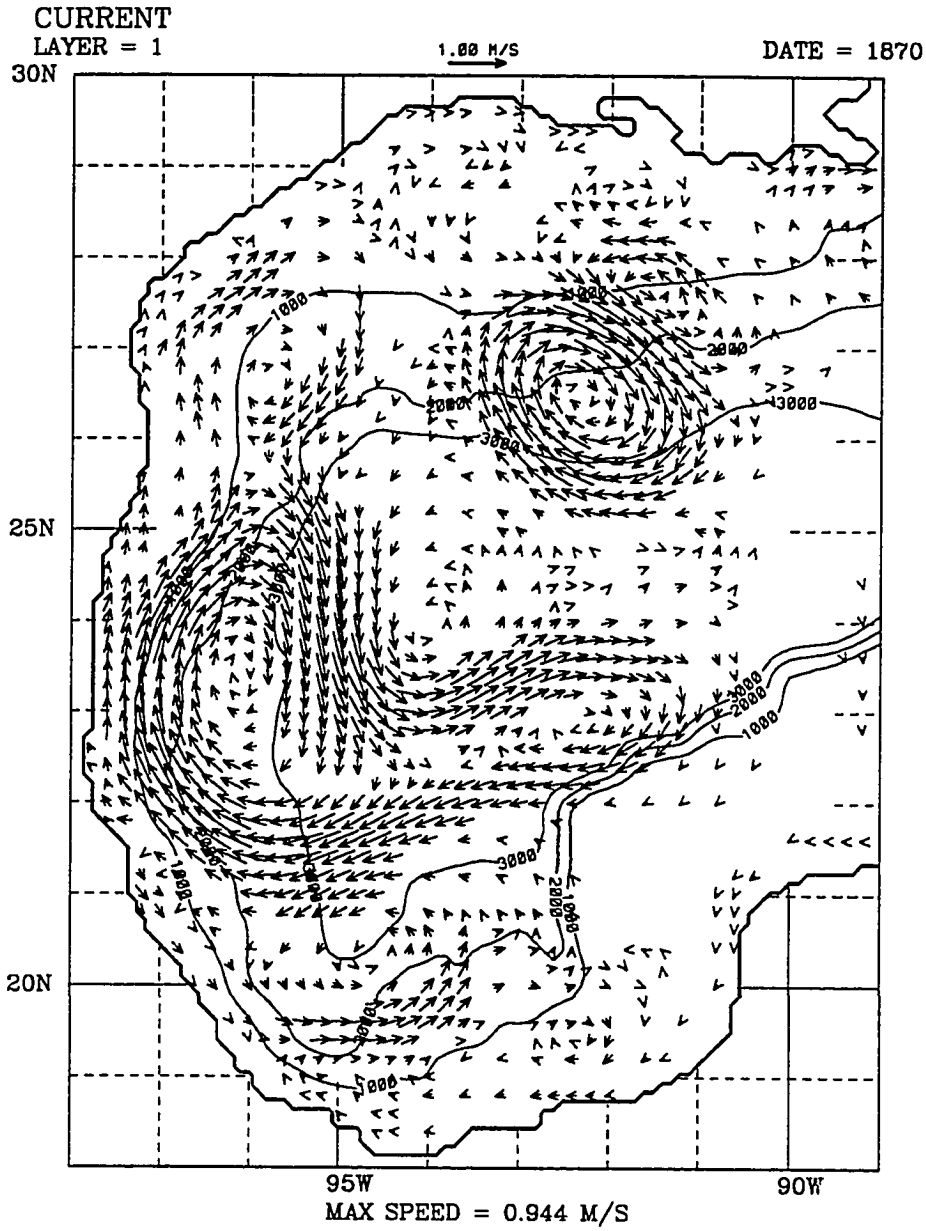

Figure 20. c) Lower layer current velocities in the western Gulf of Mexico for NOARL model day 1870. The maximum speed is .347 m/sec.

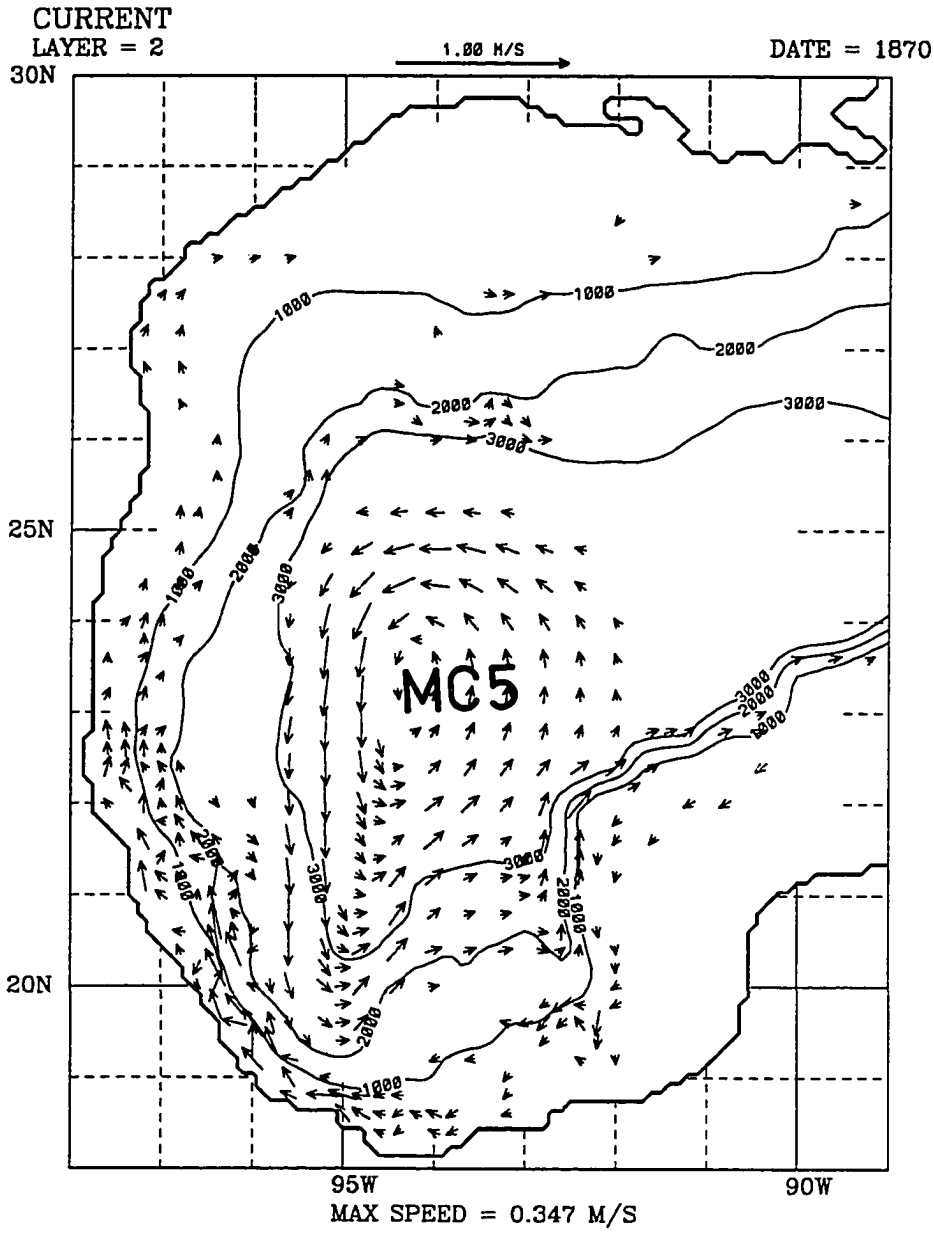

Figure 21. a) Upper layer thickness in the western Gulf of Mexico for NOARL model day 1880. The minimum and maximum thickness are 95.03 and 320.56 m.

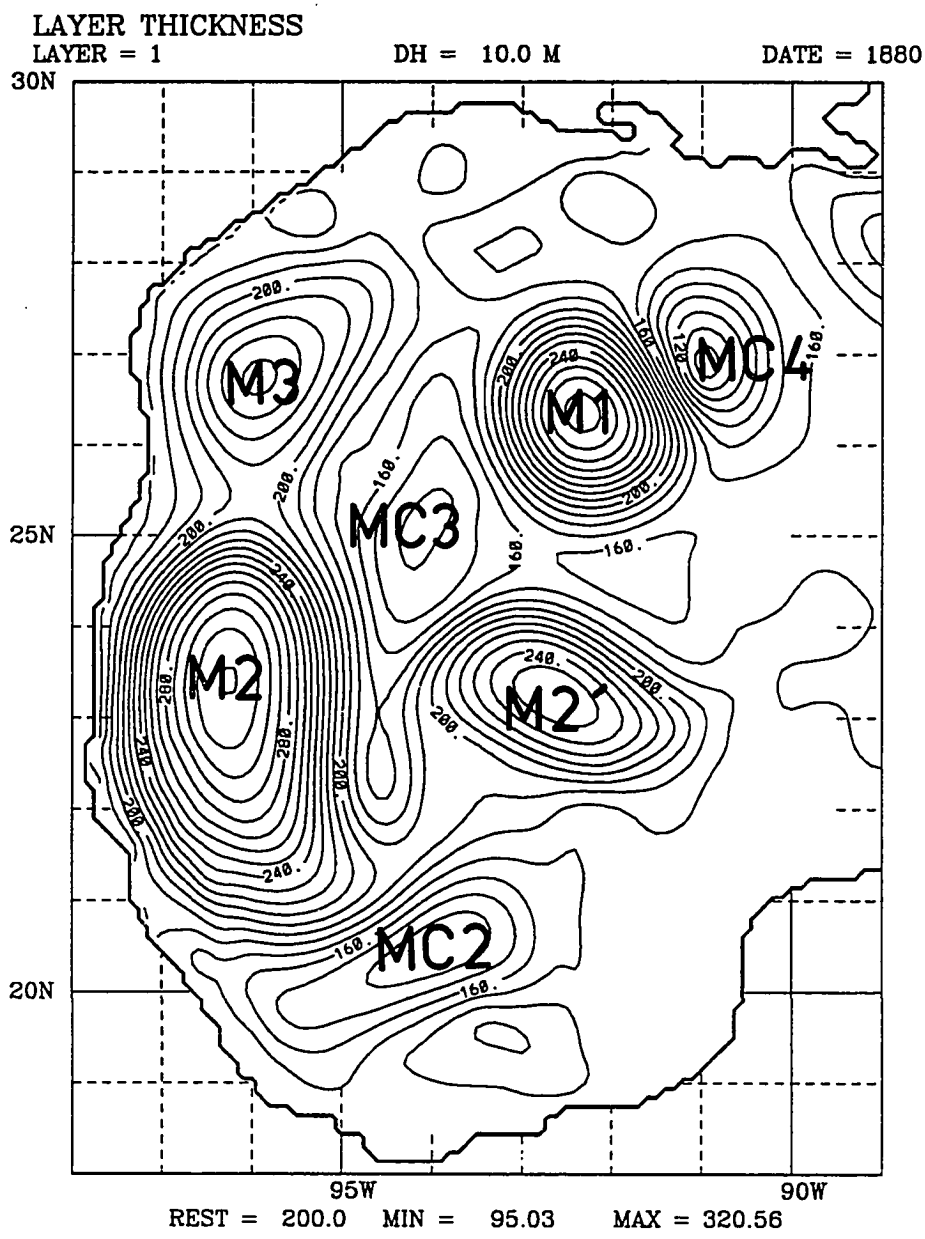

Figure 21. b) Upper layer current velocities in the western Gulf of Mexico for NOARL model day 1880. The maximum speed is 1.052 m/sec. Isobaths are shown in meters.

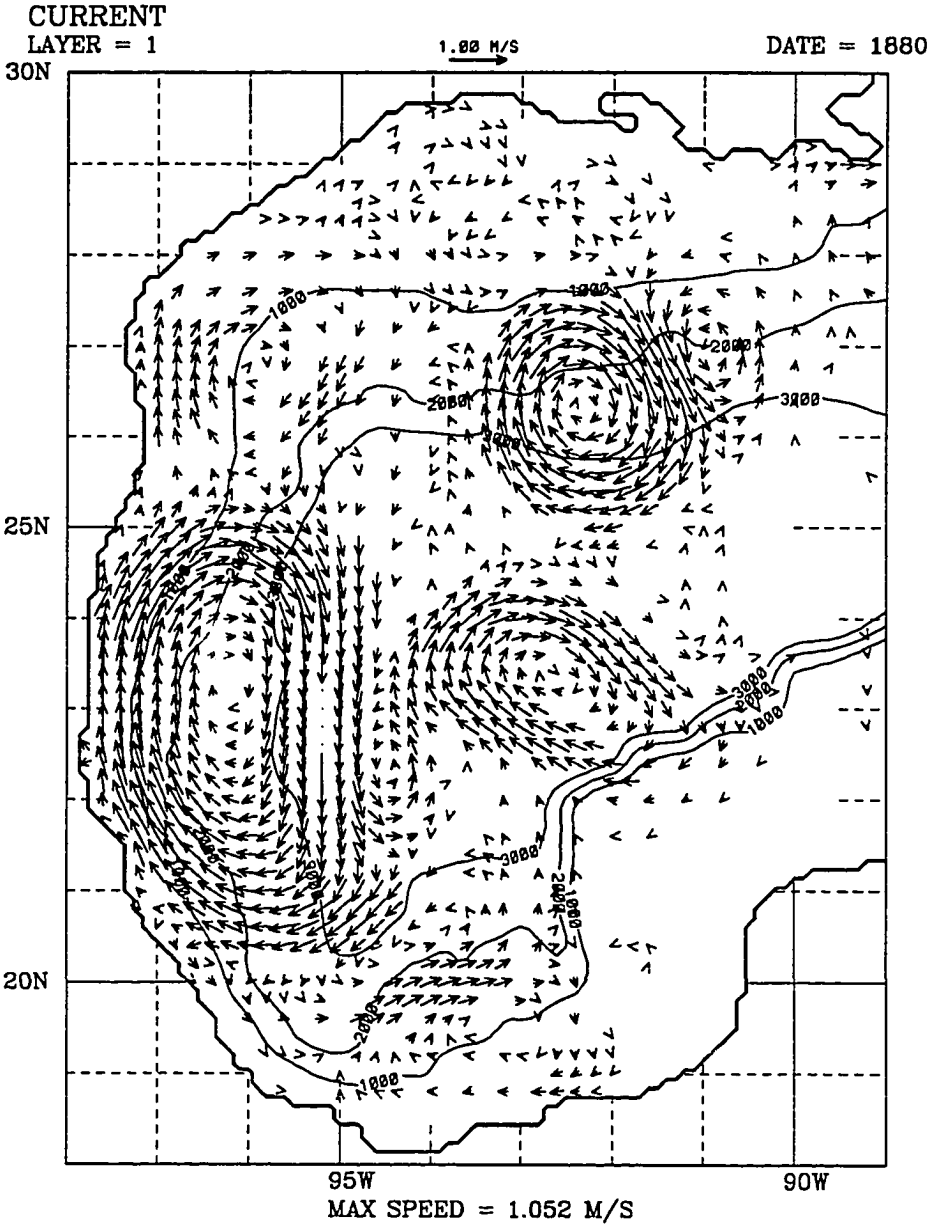

Figure 21. c) Lower layer current velocities in the western Gulf of Mexico for NOARL model day 1880. The maximum speed is .305 m/sec.

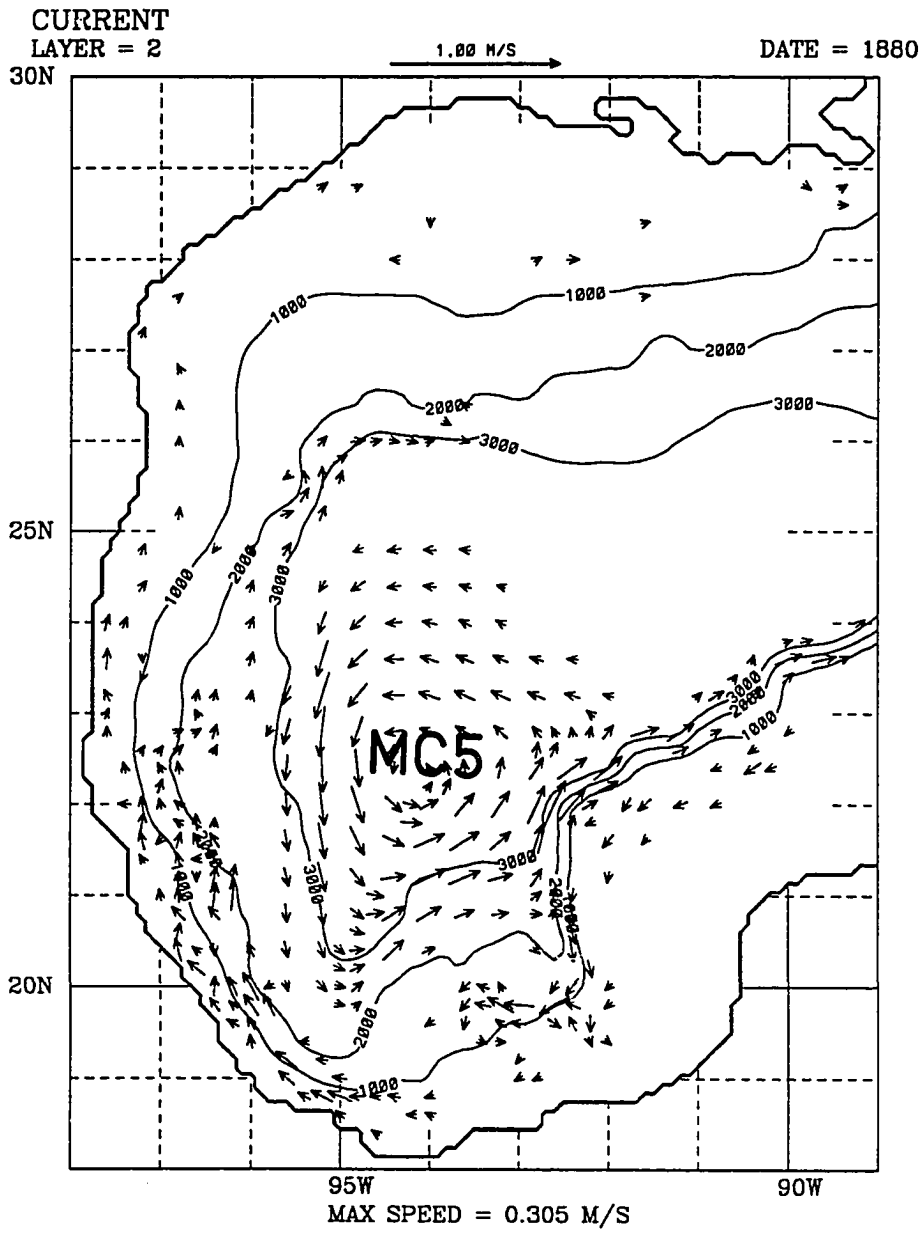

Figure 22. a) Upper layer thickness in the western Gulf of Mexico for NOARL model day 1890. The minimum and maximum thickness are 99.73 and 324.82 m.

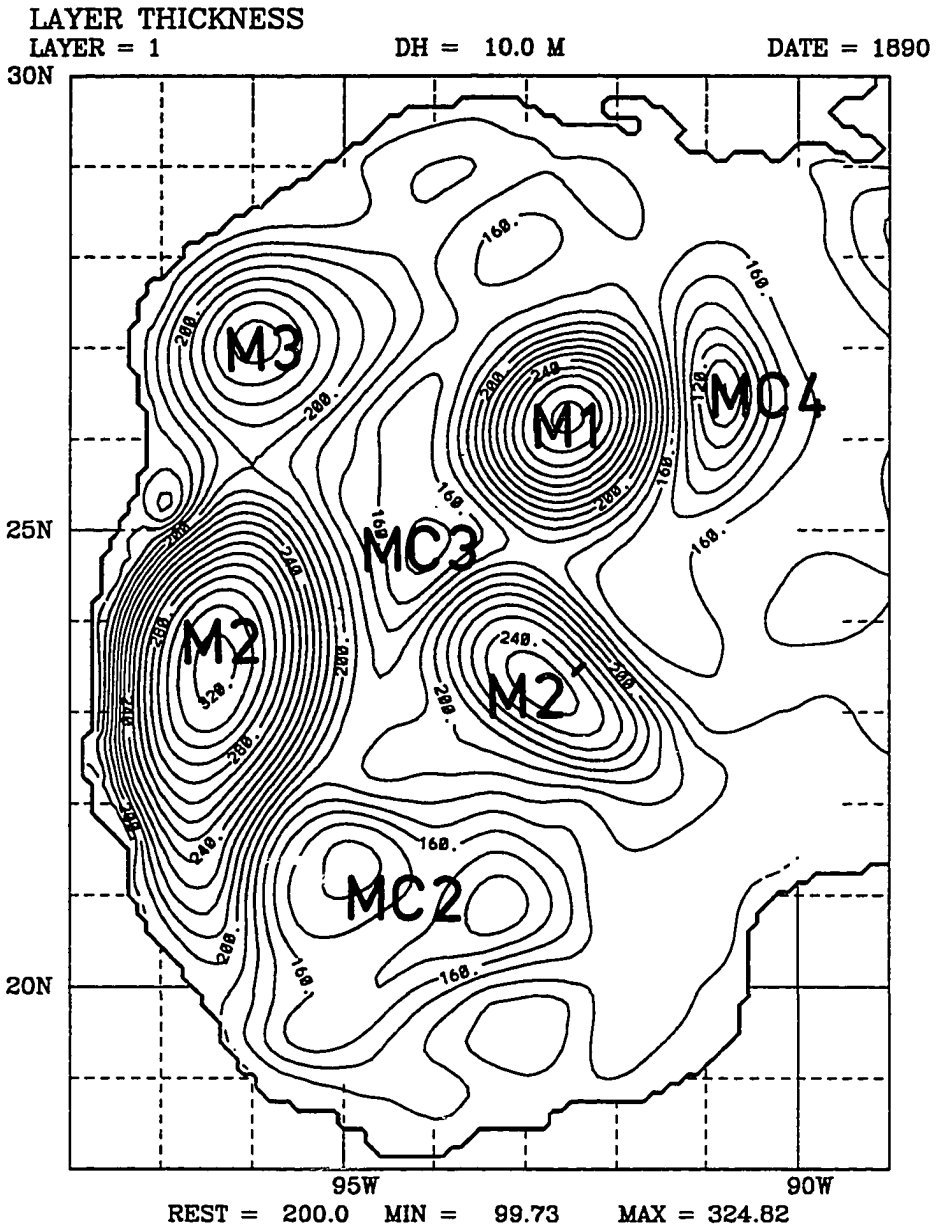

Figure 22. b) Upper layer current velocities in the western Gulf of Mexico for NOARL model day 1890. The maximum speed is 1.376 m/sec. Isobaths are shown in meters.

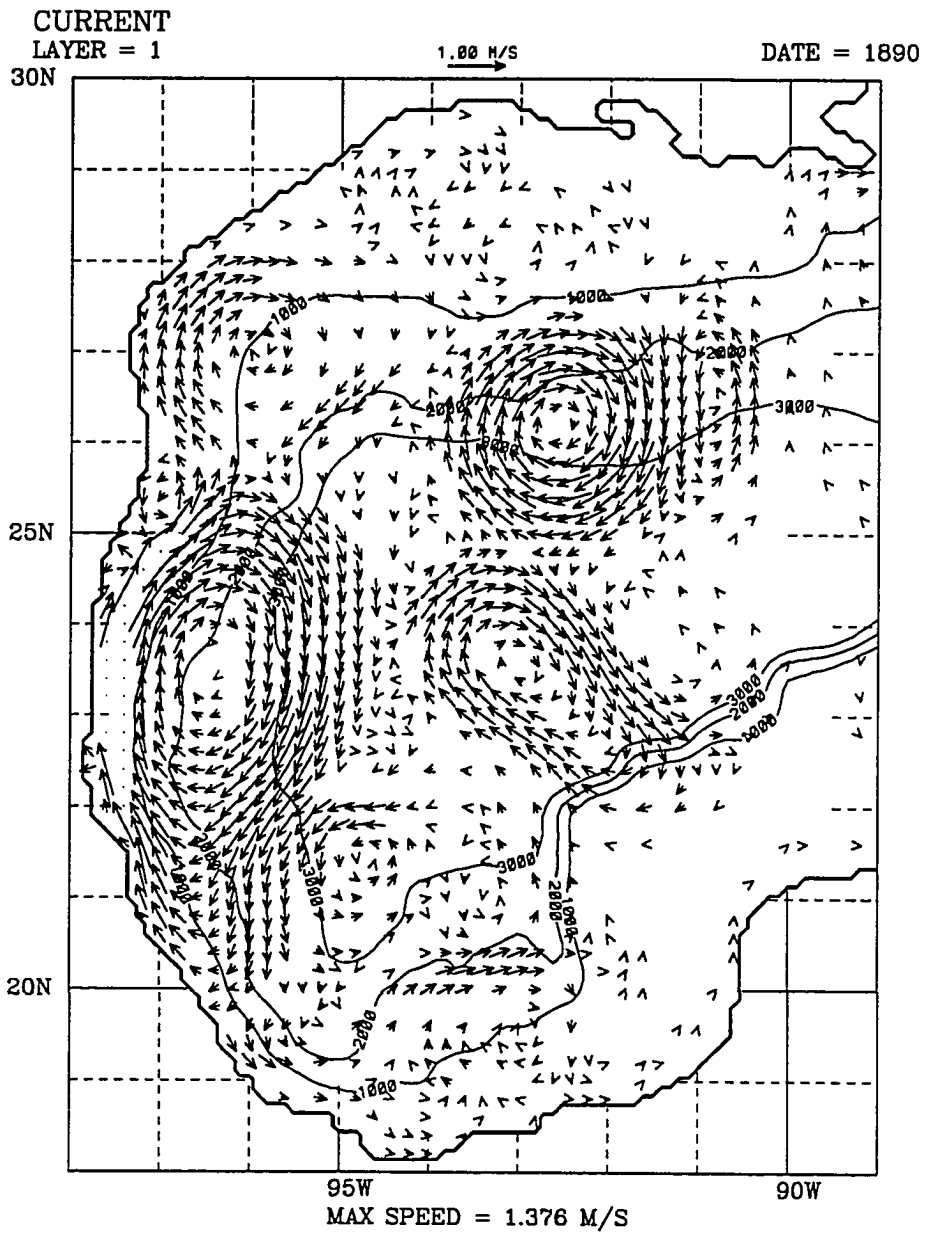

Figure 22. c) Lower layer current velocities in the western Gulf of Mexico for NOARL model day 1890. The maximum speed is .305 m/sec.

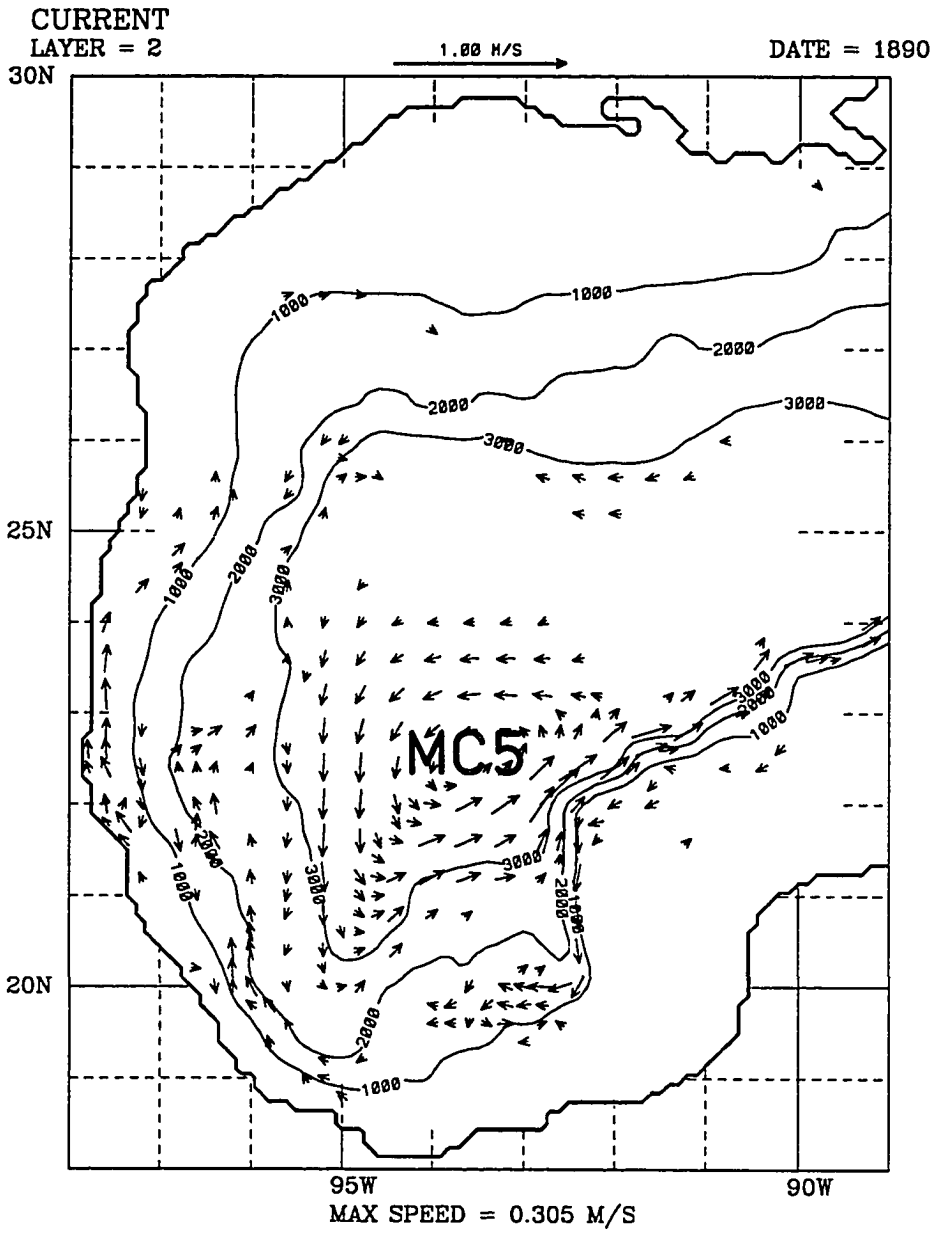

Figure 23. a) Volume as calculated from NOARL model results of days 1800–1890 for anticyclones M1, M2 and M3. The number in the time series corresponds to the number of the anticyclone: 1—M1, 2—M2, 3—M3. b) Kinetic energy as calculated from NOARL model results of days 1800–1890 for anticyclones M1, M2 and M3. c) Angular momentum as calculated from NOARL model results of days 1800–1890 for anticyclones M1, M2 and M3.

Anticyclonic Model Rings M1, M2 and M3

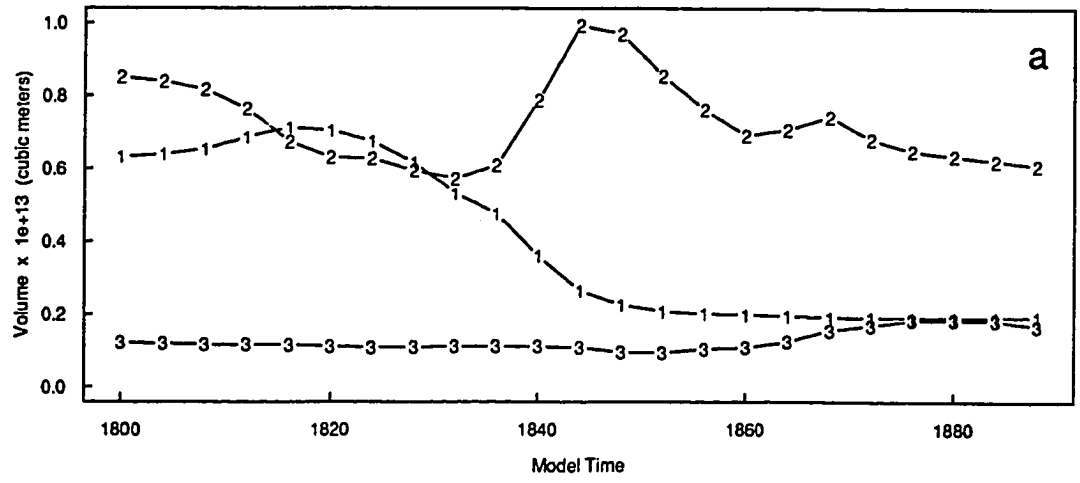

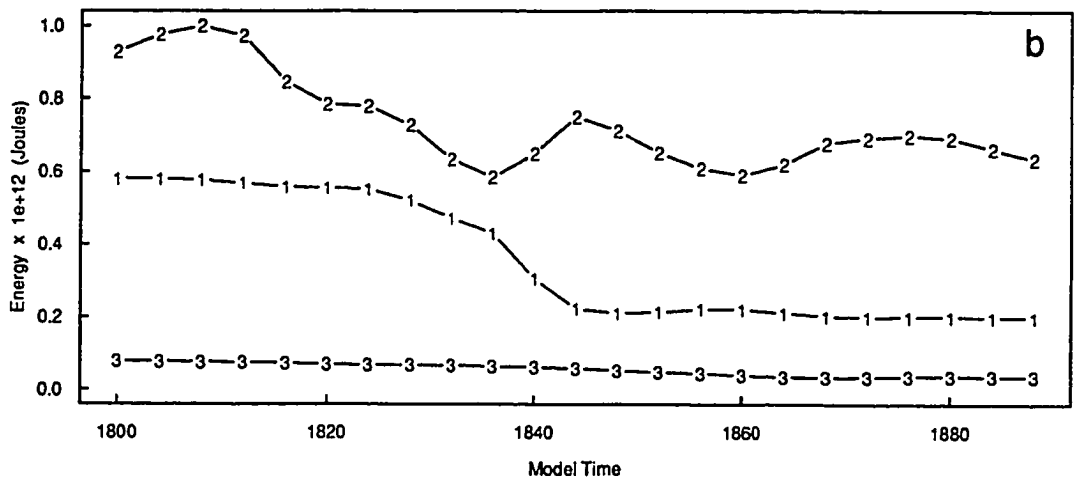

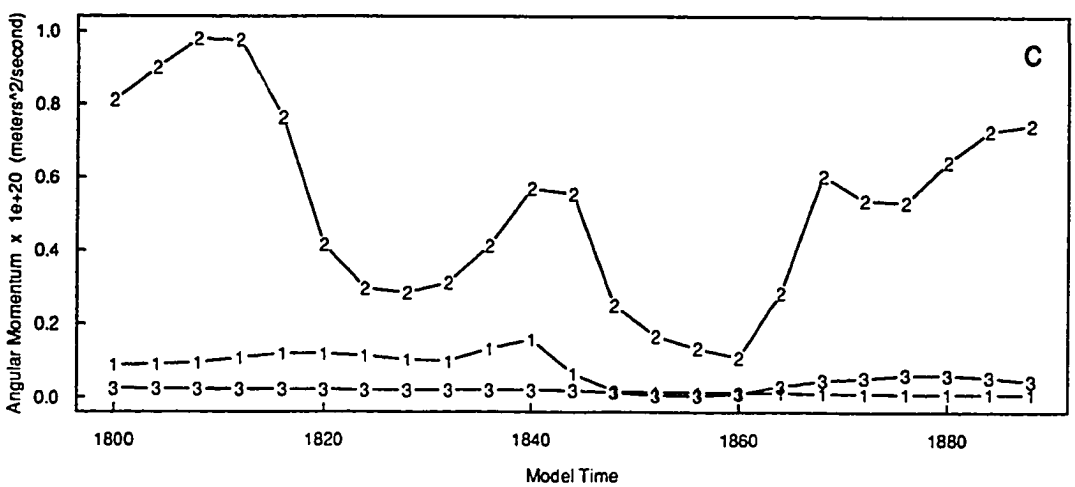

Figure 23. d) Potential vorticity as calculated from NOARL model results of days 1800–1890 for anticyclones M1, M2 and M3. The number in the time series corresponds to the number of the anticyclone: 1—M1, 2—M2, 3—M3. e) Enstrophy as calculated from the NOARL model results of days 1800–1890 for anticyclones M1, M2 and M3. f) Kinetic energy as calculated from the NOARL model results of days 1800–1890 for M1 and the lower layer cyclone, MC5.

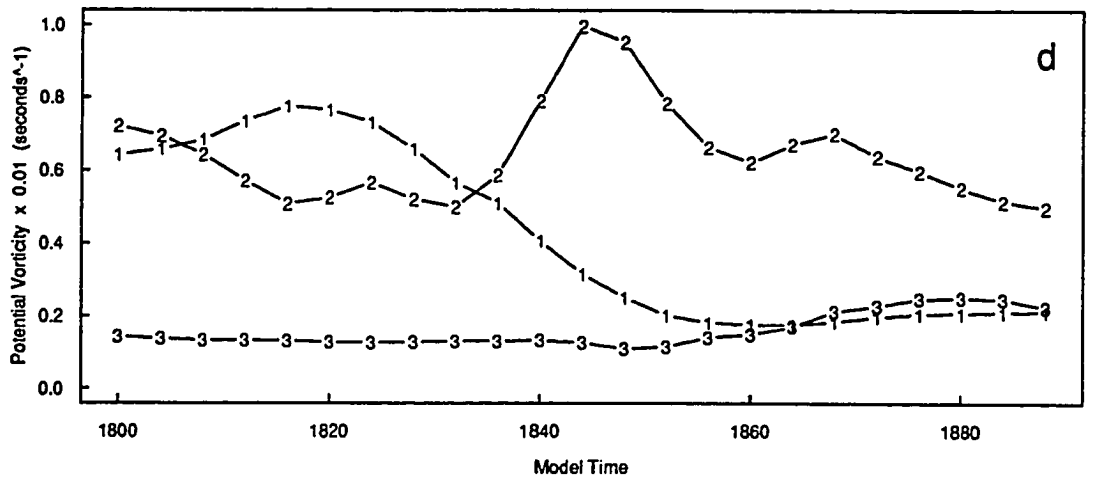

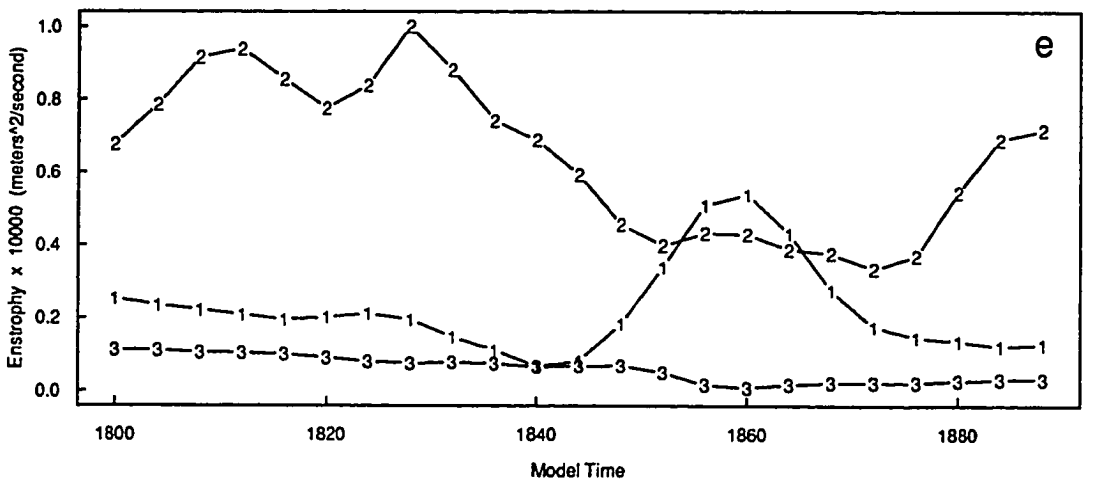

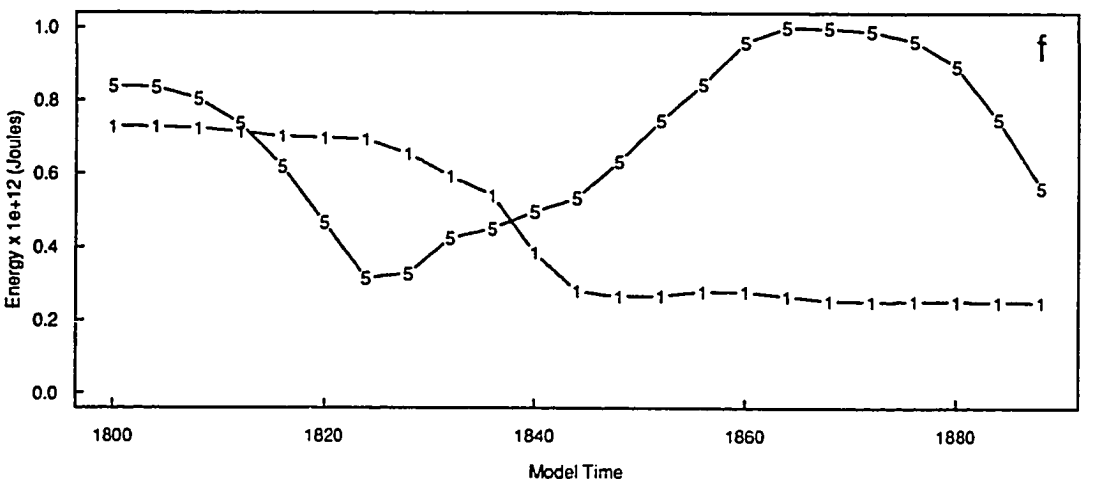

Figure 24. a) Volume calculated from NOARL model results of days 1800–1890 for cyclones, MC1, MC2, MC3 and MC4. The number in the time series corresponds to the number of the cyclone: 1—MC1, 2—MC2, 3—MC3, 4—MC4. b) Kinetic energy as calculated from NOARL model results of days 1800–1890 for cyclones, MC1, MC2, MC3 and MC4. c) Angular momentum as calculated from NOARL model results of days 1800–1890 for cyclones, MC1, MC2, MC3 and MC4.

Cyclonic Model Rings MC1, MC2, MC3 and MC4

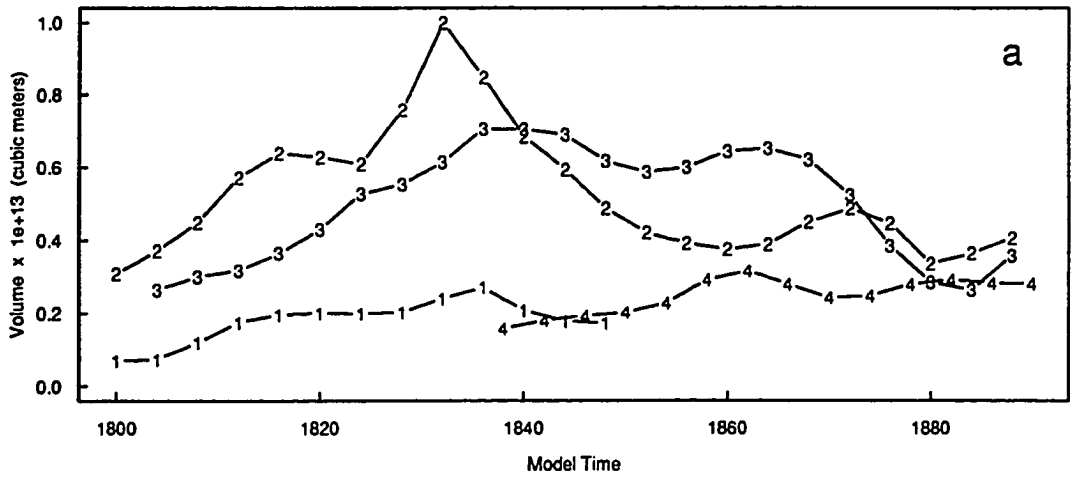

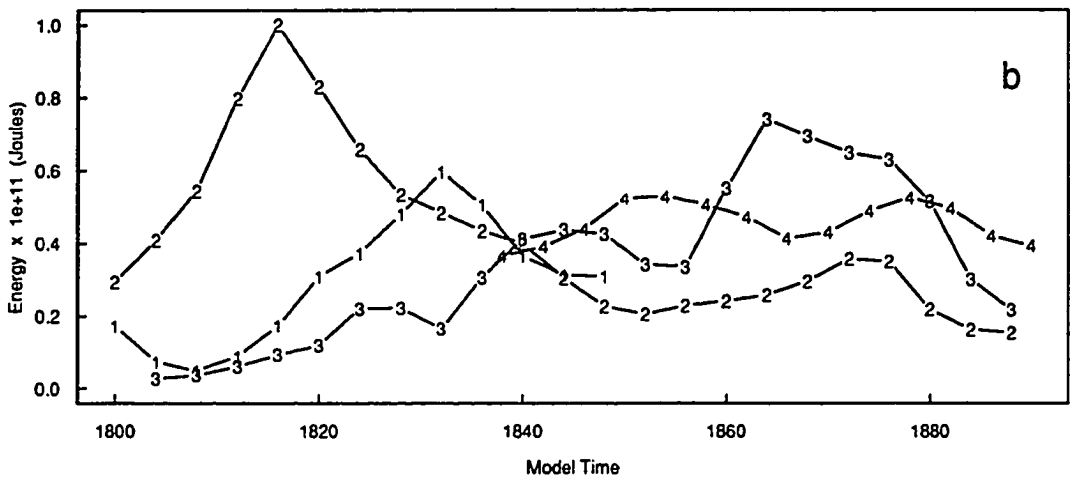

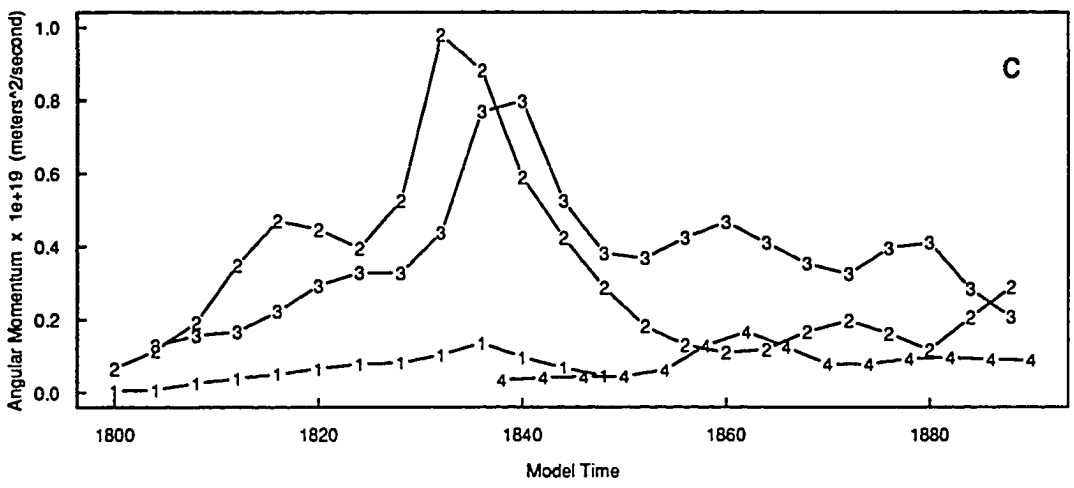

Figure 24. d) Potential vorticity as calculated from NOARL model results of days 1800–1890 for cyclones, MC1, MC2, MC3 and MC4. The number in the time series corresponds to the number of the cyclone: 1—MC1, 2—MC2, 3—MC3, 4—MC4. e) Enstrophy as calculated from the NOARL model results of days 1800–1890 for cyclones, MC1, MC2, MC3 and MC4.

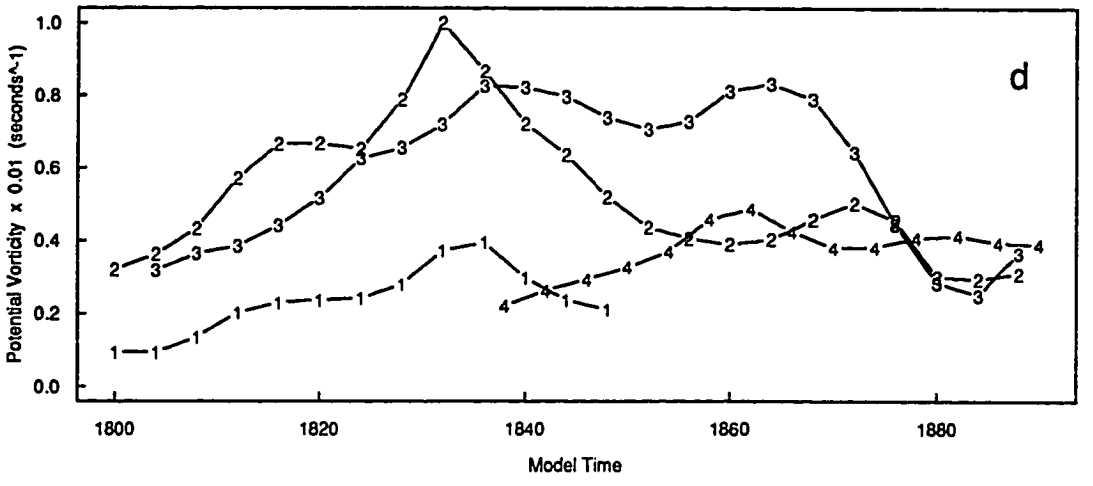

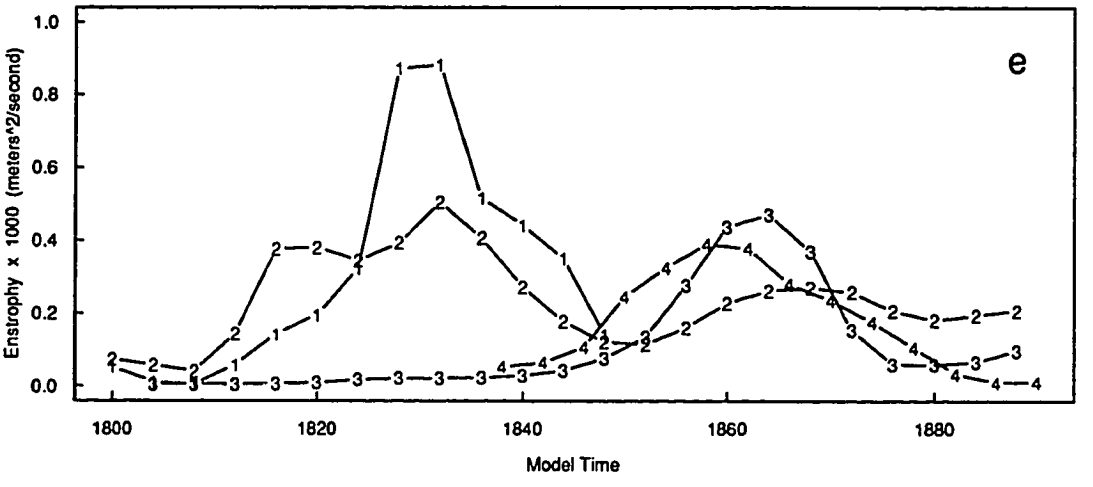

Figure 25. a) 15 °C isothermal contours (m) from R/V Gyre cruise 78-G-3 of April 1 - 12, 1978. The center of the cyclonic and anticyclonic circulations are L and H, respectively. Dashed lines denote extrapolated contours. From Merrell and Morrison (1981).

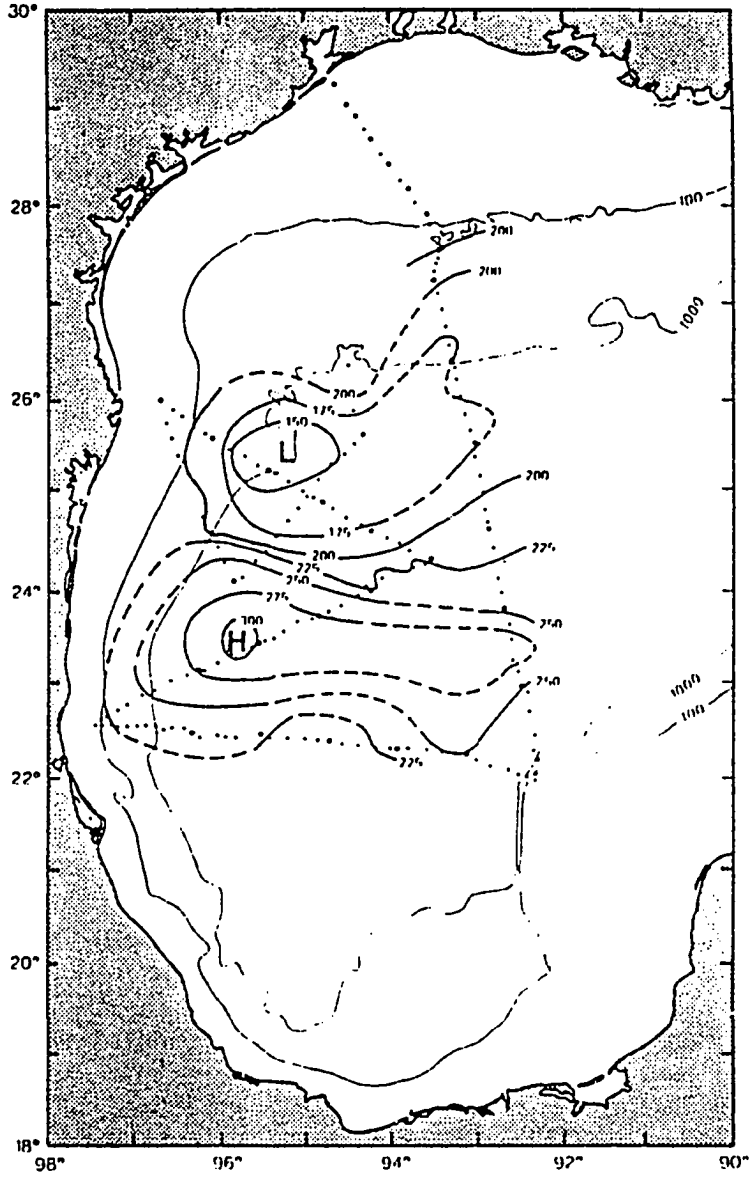

Figure 25. b) 15 °C isothermal contours (m) from the Gran Remolino cruise of April 12 – 26, 1978. (From Merrell and Morrison, 1981).

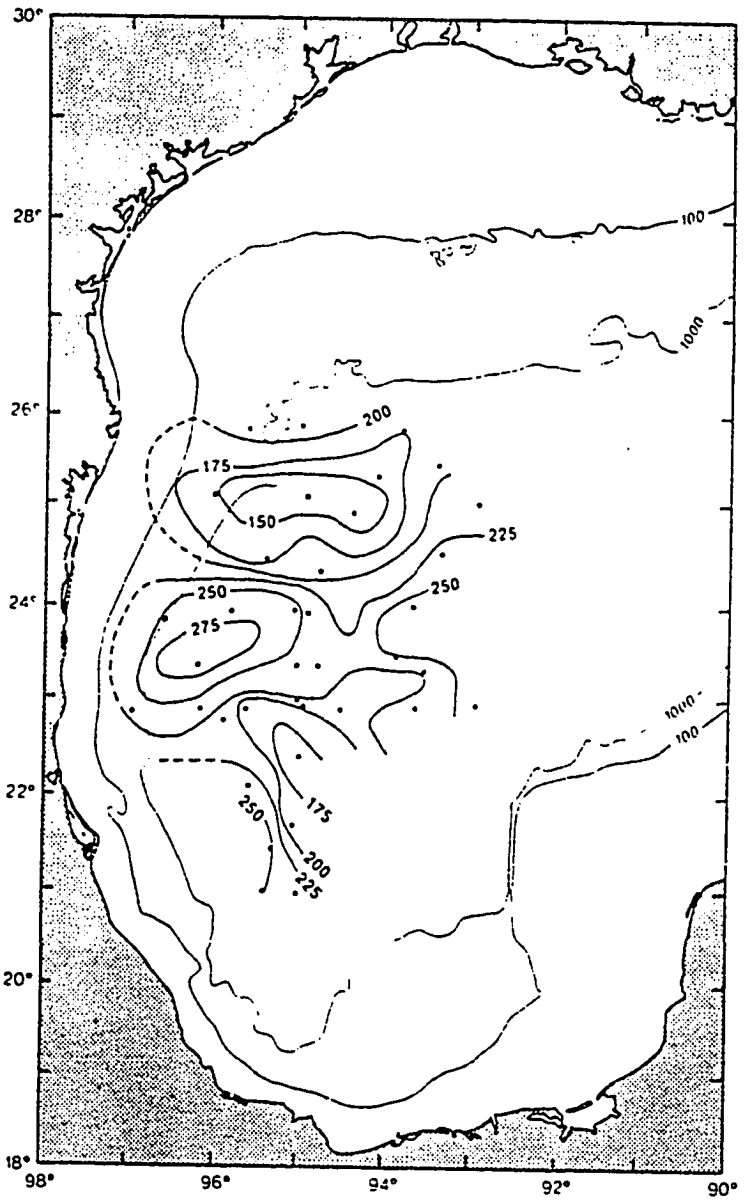

Figure 26. Path trajectory of drifter 3378 for the entire Gulf of Mexico. The solid line is path of the drifter low-pass filtered at 100 hours. Arrows denote 10 day intervals. The solid dot and X mark the start and end, respectively.

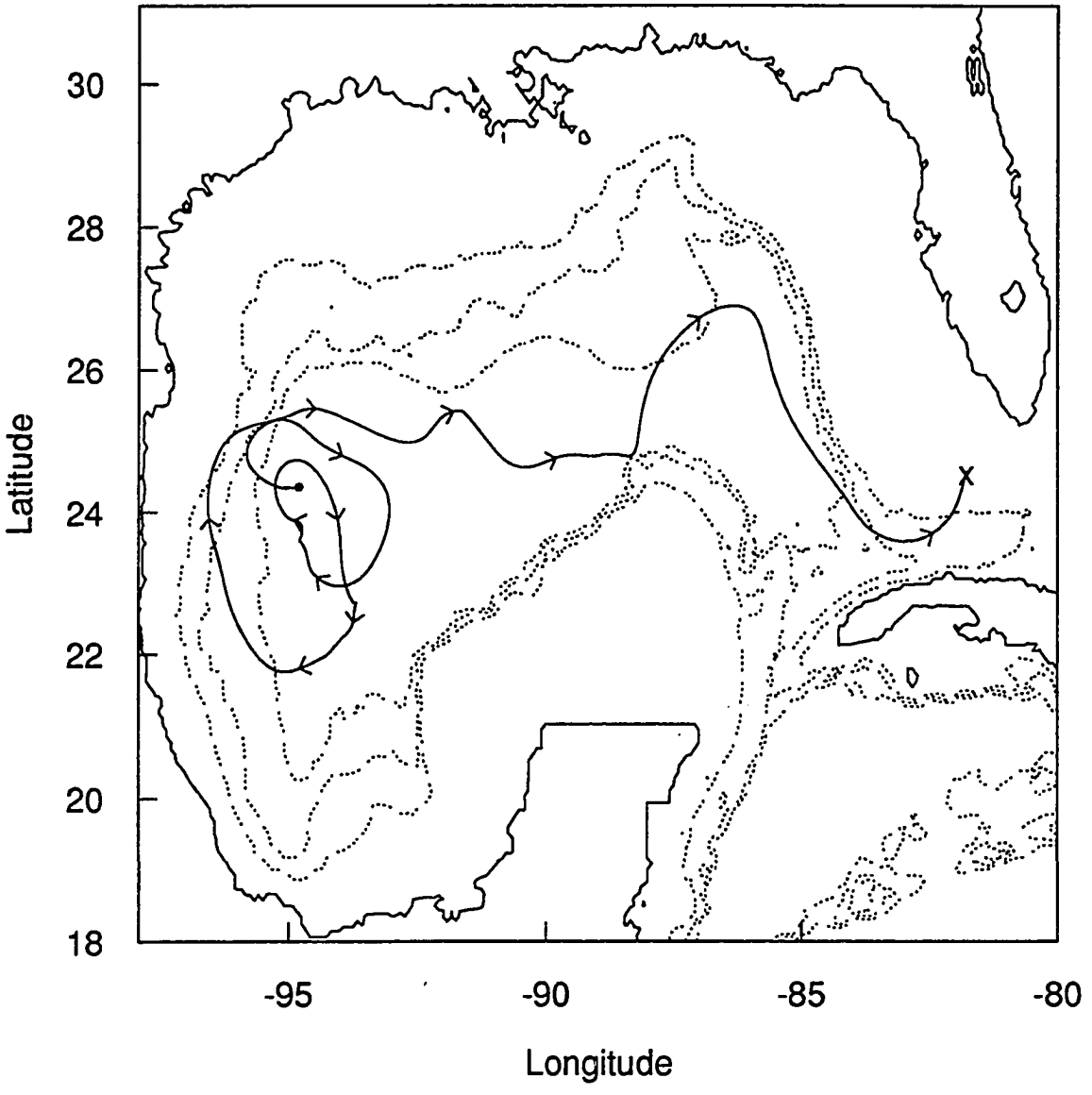

Figure 27. a) Isotherms (m) for 14 °C surface from R/V Gyre cruise 80-G-1 of March 30 - April 14, 1980. Dashed contours are extrapolated and hence subject to error. The broad solid line shows the position of the front and the hash marked line is the position of a warm filament associated with the front (From Brooks and Legeckis, 1982).

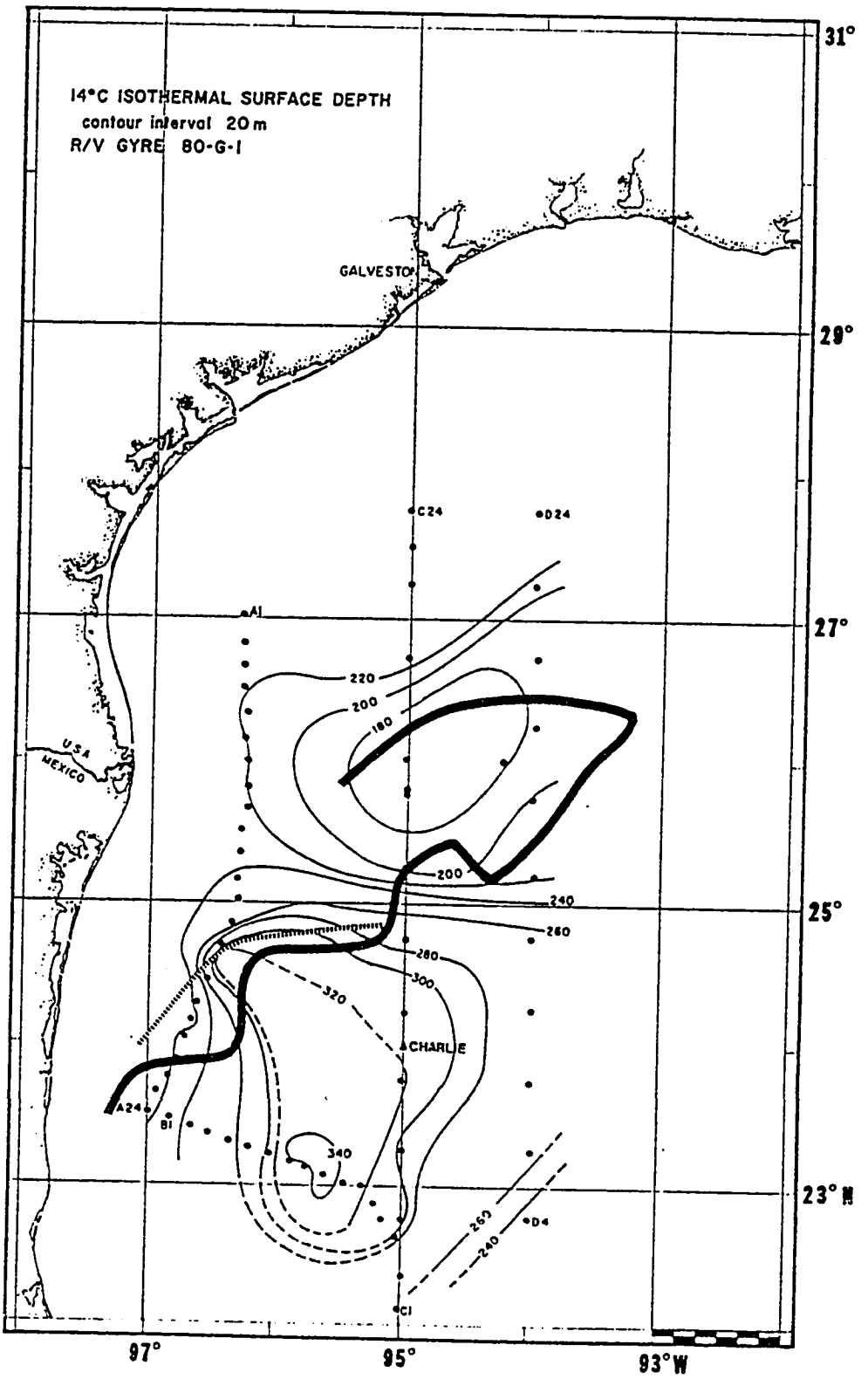

Figure 27. b) Thermal contours (°C) from ten stations along Transect C from R/V Gyre cruise 80-G-1 of April 4, 1980.(From Brooks and Legeckis, 1982). c) Salinity contours (‰) from ten stations along Transect C from R/V Gyre cruise 80-G-1 of April 4, 1980.(From Brooks and Legeckis, 1982).

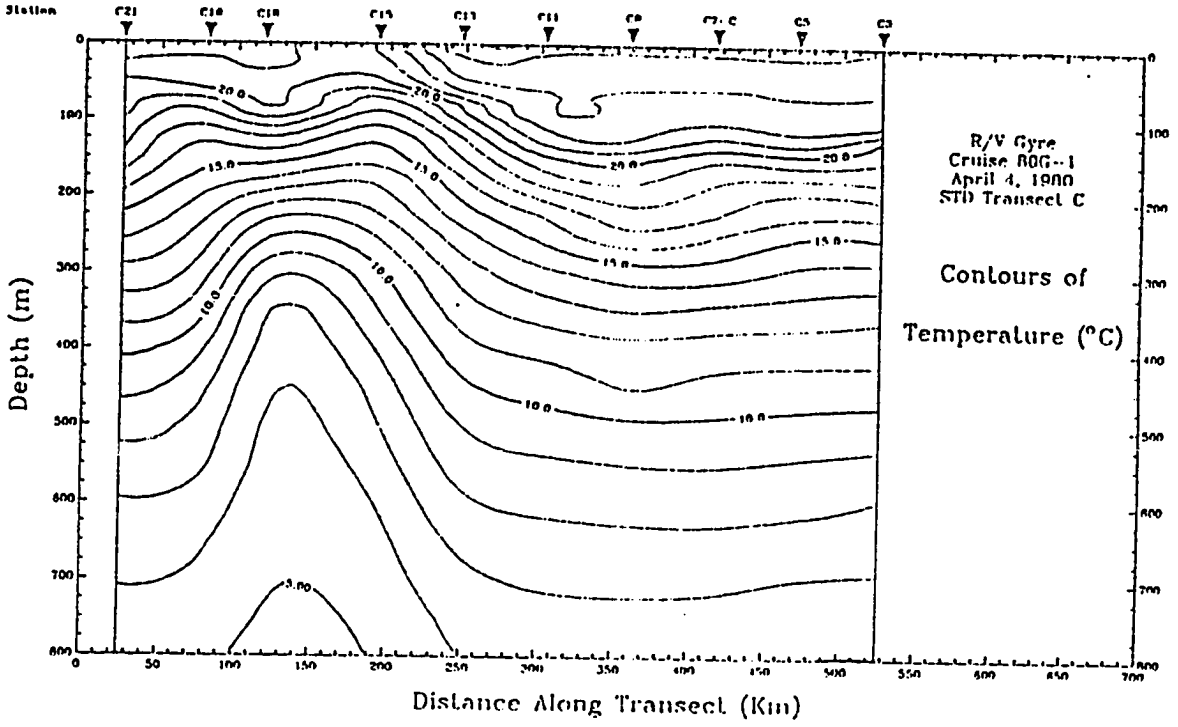

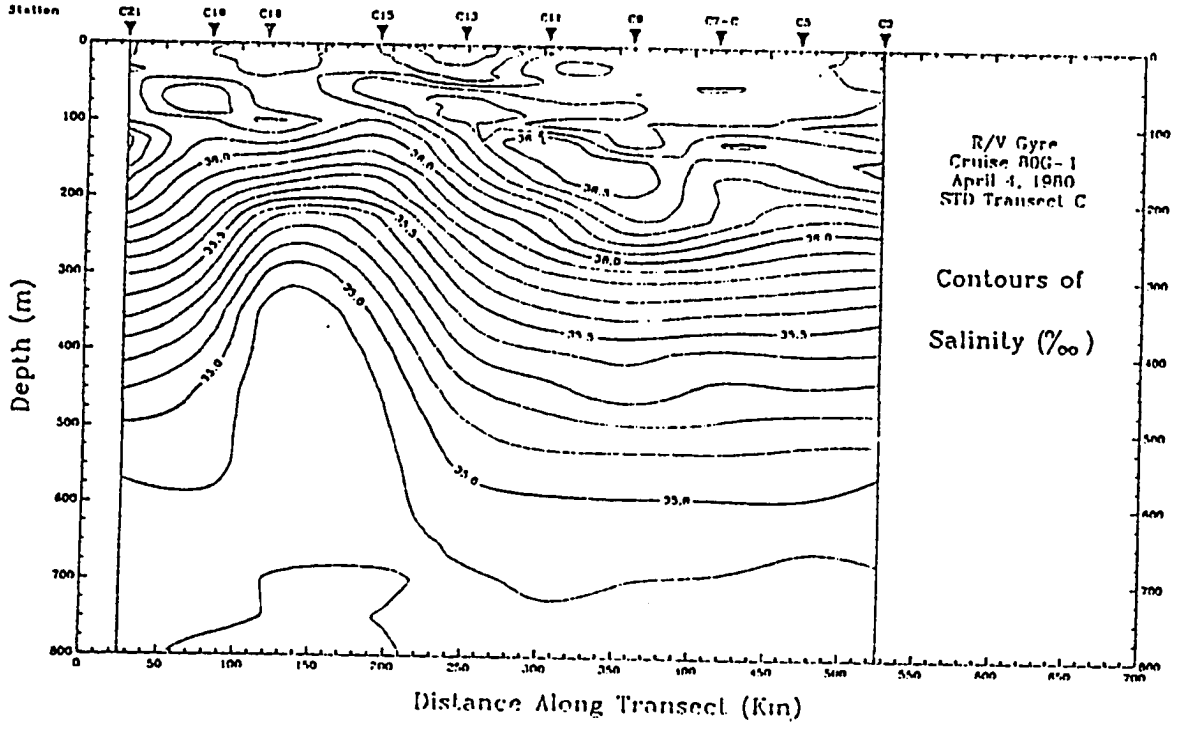

Figure 28. Isotherms (m) for 8 °C surface from XBT data of October 14 – November 24, 1987. (From SAIC, 1988).

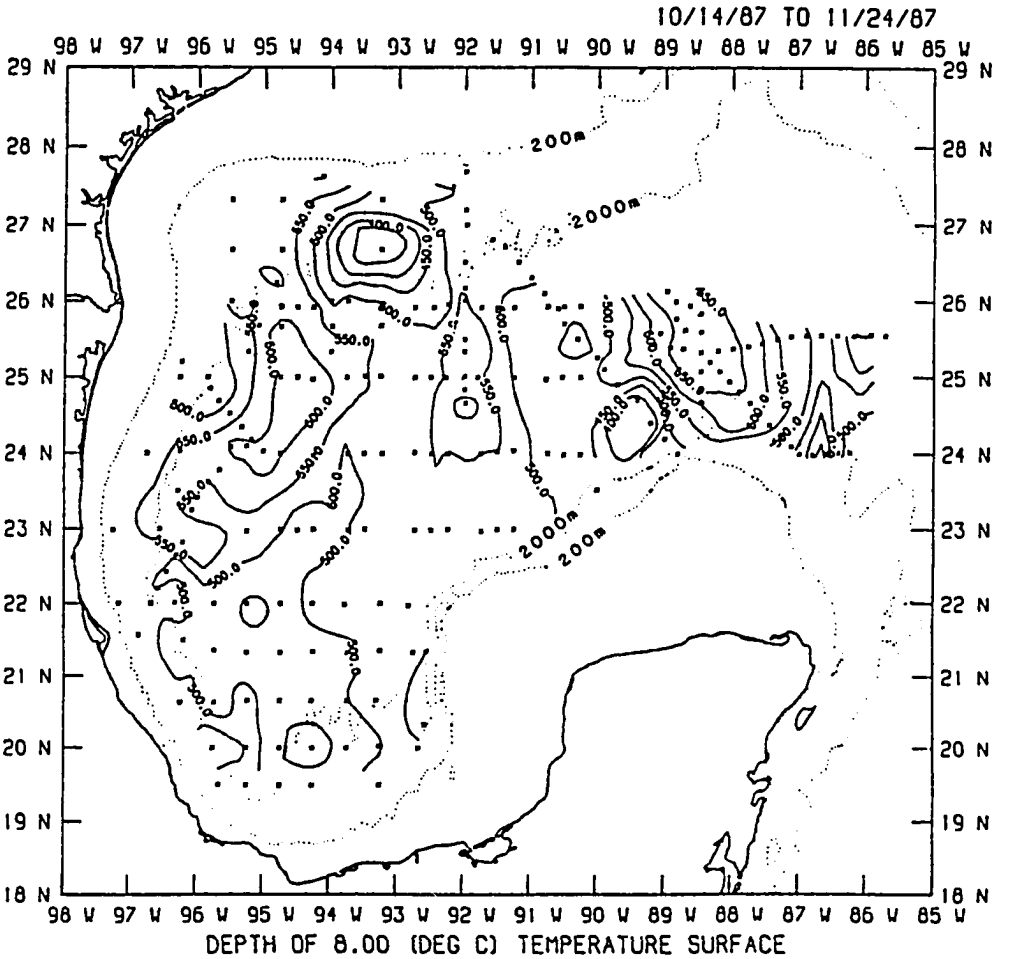

Figure 29. Path trajectory of drifter 5839. The solid line is the actual path of the drifter low-pass filtered at 100 hours. Arrows denote 10 day intervals. The solid dot and X mark the start and end, respectively.

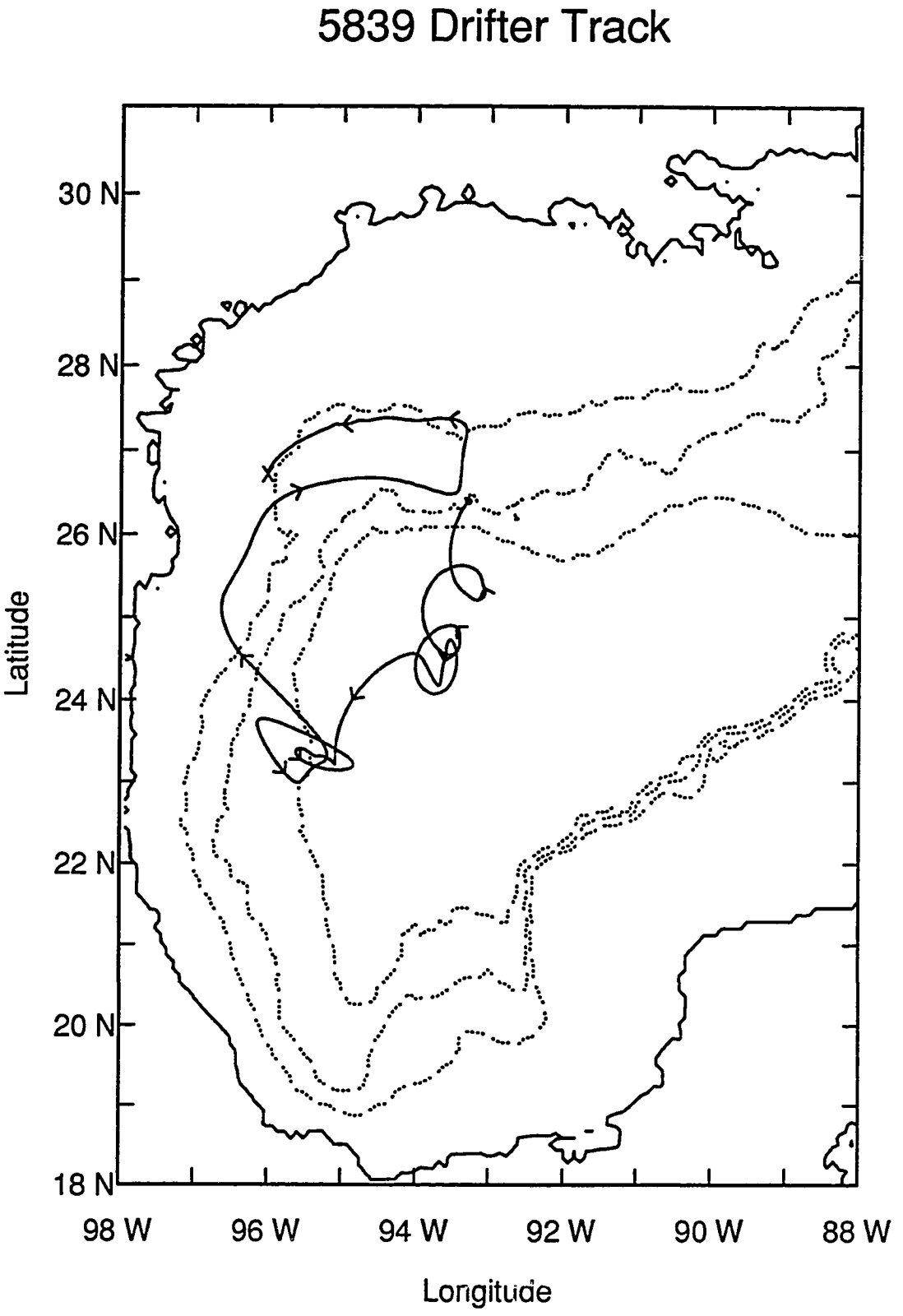

Figure 30. a) Mean velocity vectors from all of the direct current measurements below 1000 m. Mooring R5 data was from July – October, 1985 while all others were from July, 1985 – May, 1986. (From Hamilton, 1990).

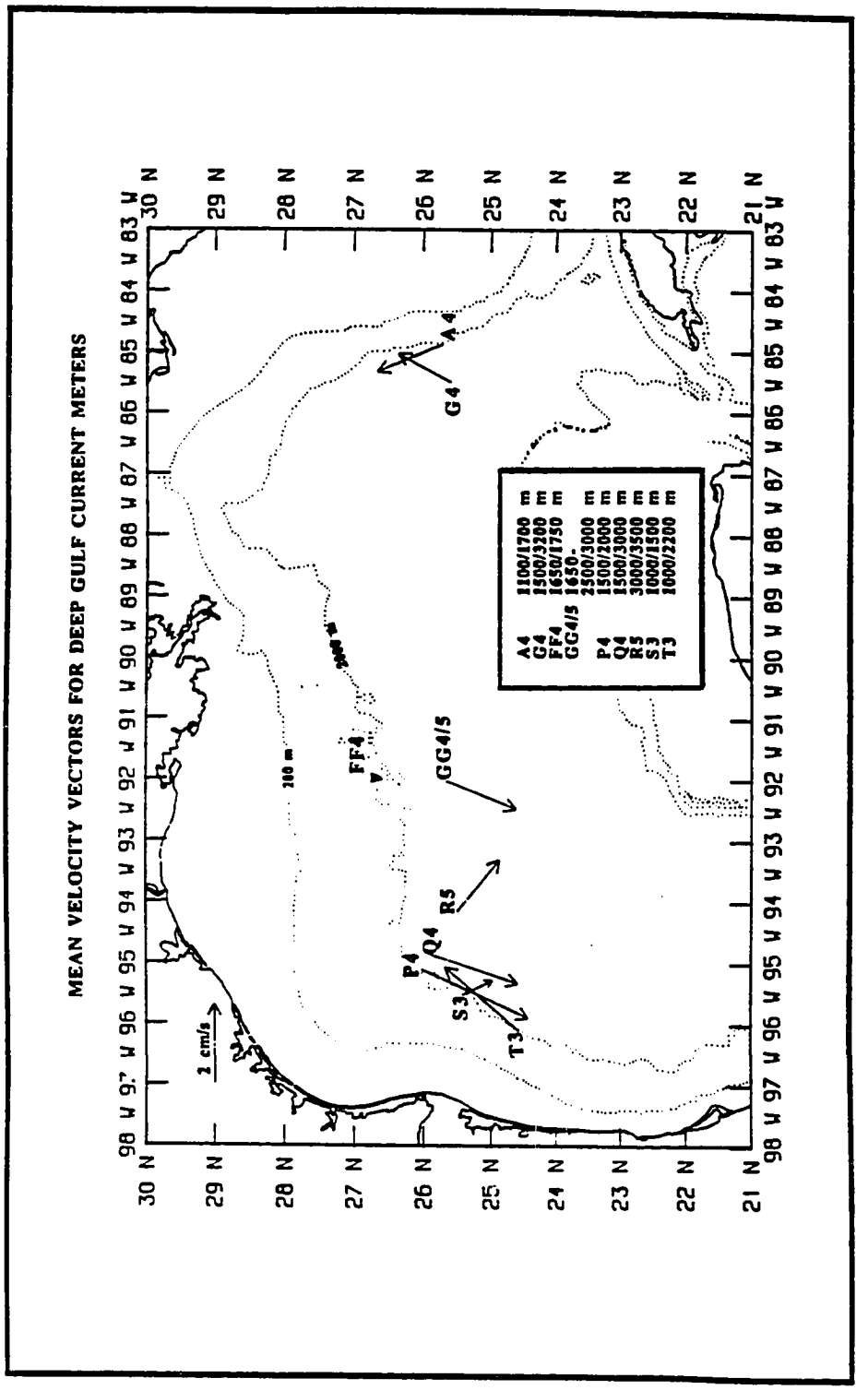

Figure 30. b) Stick vector time series of 40-hour low-passed currents for mooring R. (from SAIC, 1988, p. 91).

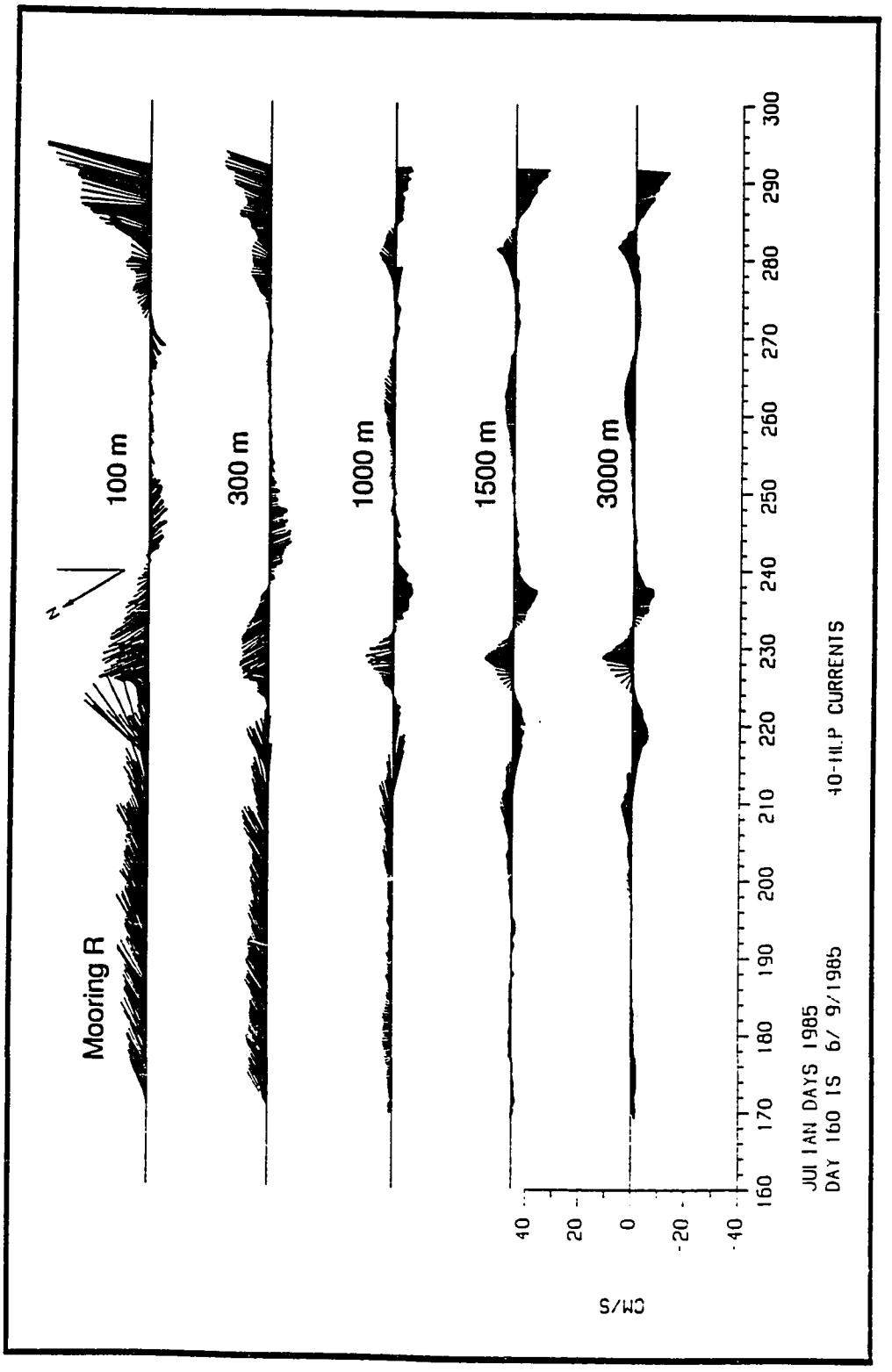

7. Biography

Adolphe William Indest was born in a house two blocks from Bayou Terrebonne in what is now known as Houma, Louisiana. He was raised in New Orleans and educated in the parochial school system where he learned nuns do not take kindly to the epithet, penguins. His undergraduate career spanned nearly seven years as, out of necessity, he was involved with a multitude of jobs and women. In December, 1979, he received, without fanfare, his Bachelor of Science degree with a General Studies major from a secretary in the Office of the Student Registrar, Louisiana State University. He must have learned nothing from the past seven years, for he then continued his educational career at the University of New Orleans where he earned a Master of Science degree in Biological Sciences in a record three years. He was then accepted in the physical oceanography program at the University of South Florida in lovely, sunny St. Petersburg. However, his major professor was awarded the Slover endowed chair in physical oceanography at Old Dominion University so he moved to Norfolk, Virginia with his major professor. Currently he is attempting to receive his terminal degree, a Ph.D. in physical oceanography, from Old Dominion University. He is married to Marci Indest, a lovely woman and wonderful tennis player, and has one child.